# Numerical Simulations of Internal and Inertial Solitary Waves

Thesis submitted for the degree of
Doctor of Philosophy

## Andreas Aigner

*Department of Mathematics and Statistics,*
*Monash University, Clayton VIC 3800, Australia*

*January 2001*

# Contents

# Summary

The objectives of this thesis are the numerical verification of the theory developed by Derzho and Grimshaw for large-amplitude solitary waves with recirculation regions in stratified fluids (1997) [16] and axisymmetric rotating flows through cylindrical channels [15]. This study is further complemented by the verification of the theory by Grimshaw and Yi (1991) [32] for the generation of solitary waves by stratified flow over topography and the theory by Derzho and Velarde (1995) [17] for multi-scaled internal solitary waves.

For this purpose two novel numerical methods are developed based on the pseudospectral scheme by Rottman *et al* (1996) [58]. The time-dependent fully nonlinear governing equations are integrated using spectral methods for the spatial integration and a low-storage Runge-Kutta method for the temporal integration. For the case of stratified flow the governing equations are considered with and without the Boussinesq approximation. In order to include the inertial effects discarded in the Boussinesq approximation the Runge-Kutta method is coupled with a Liouville-Neumann iteration. For both models a form of the generalized Poisson equation is solved using direct methods.

The governing equations are given in chapter 2 and the asymptotic theory for the four applications is described in chapter 3. The numerical methods are described in chapter 4 and chapter 5 presents the results for the four applications, followed by the conclusion in chapter 6.

# Statement

This thesis contains no material which has been accepted for the award of any other degree or diploma at any university or institution and, to the best of my knowledge and belief, contains no material previously published or written by any other person, except where due reference is made in the text.

A. Aigner

# Publications

A. Aigner, D. Broutman and R. Grimshaw, (1999), "Numerical simulations of large amplitude internal solitary waves with vortex cores", *Fluid Dyn. Res.* **25**:315-333

A. Aigner, R. Grimshaw (2001), "Numerical simulations of the flow of a continuously stratified fluid, incorporating inertial effects", *Fluid Dyn. Res.*, to appear

# Acknowledgements

The author of this thesis would like to express his appreciation for the inexhaustible support and immeasurable supervision received by Prof. Grimshaw and Dr. Broutman.

The author also wishes to acknowledge the valuable discussions with Dr. Derzho, assistance with the numerical codes by Dr. Rottman and is indebted to Dr. Blennerhassett and Dr. McKee for their ceaseless encouragement and motivation. In addition, the author expresses his gratitude to his fellow students at Monash University and the University of NSW.

Last but not least the author would like to thank Ines Rittgasser, Walter Schrabmair and his family for being there when it mattered the most.

To my father

# Chapter 1

# Introduction

In 1834 John Scott Russell [59] was the first to record the existence of a new kind of wave, which he observed on the surface of water flowing through the British canals. Originally termed 'the great wave of translation' the observed wave consisted of a single hump and became known as a solitary wave due to its localized horizontal extension and non-periodicity in space. The discovery of solitary waves was particularly exciting because their permanent nature seemed to contradict prevalent shallow water theory. A theoretical equation for the shape of these waves was discovered by Kortweg and de Vries (1895) [41] but the ubiquitous nature of solitary waves in many physical systems was noticed only in the 20th century.

In 1965 Zabusky and Kruskal [73] discovered the mathematical significance of solitary waves with respect to the Korteweg-de Vries equation. In their numerical investigations they observed several remarkable qualities. For instance that solitary waves emerge unchanged from interactions with other solitary waves and that several conservation laws can be derived. Solitary waves are nonlinear waves of permanent form which exist due to a balance between nonlinear wave-steepening effects and linear wave dispersion. These discoveries lead them to coin the name 'solitons' for solitary waves, signifying the attributed particle-like qualities. Since these fundamental discoveries nonlinear wave theory has become a fruitful field of study and nonlinear wave equations similar to the Kortweg-deVries equation were found in a wide variety of physical contexts such as plasma physics, lattice dynamics and optics. A derivation of the KdV equation and generalizations can be found in Gardner *et al* (1974) [23] with methods

1

for solving the KdV equation.

This study focuses on the structure of internal solitary waves in a stratified fluid and inertial solitary waves in an axially-symmetric rotating flow through a cylindrical channel. Of particular interest are large-amplitude solitary waves with vortex cores. In a stratified flow the structure, as well as the generation of large-amplitude solitary waves by localized bottom topography in a channel of finite depth are investigated. The study of internal solitary waves is further complemented by the study of multi-scale finite-amplitude solitary waves.

The study of solitary waves in stratified fluids is significant with regard to the ocean, where solitary waves of large-amplitude can threaten marine as well as submarine constructions. Moreover, the results are relevant for atmospheric systems, regarding "lee waves" as well as the "Morning Glory" phenomenon (also known as "roll clouds"), which pose dangers to aviation. In both cases the solitary waves are believed to be directly related to the evolution of bores. Inertial solitary waves with vortex cores propagating in a rotating flow through a cylindrical channel are important, since they can provide insight into the still unexplained phenomenon of vortex breakdown. Furthermore, they are applicable to the construction of turbines, jet propulsion in aviation and space technology as well as hydrodynamic technology.

In the following, the theoretical background and development of the applications considered in this study are discussed.

*Internal solitary waves*

The first indication of internal waves in the ocean can be found in Nansen (1902), who noticed naturally occurring internal waves – stumbling upon them on his famous *'Fram'* voyage – and was confronted with the "dead water" phenomenon, which incited Ekman (1904) to investigate this phenomenon. Initially interfacial internal waves were studied by Stokes (1847) as well as von Helmholtz (1868). Subsequently, internal waves in continuously stratified fluids were investigated by Lord Rayleigh (1883) and Love (1891).

The first elementary theoretical investigations of internal waves for a continuously stratified ocean are from Fjeldstad (1933) [20], where the first comprehensive overview of linear internal wave theory, for a rotating earth, along thermoclines and methods for detecting internal waves at sea are given. Defant (1952) [14] provided an overview of internal waves of tidal periods and discusses stability conditions of internal tidal waves, but it was not until Long (1953/54/55,1964) [47, 48, 49, 50] and Dubreil-Jacotin (1937) [19] that a complete theoretical and experimental foundation for the study of internal waves – comprising linear and nonlinear theory – was presented.

The governing equations for the system of six homogeneous partial differential equations describing the eigenoscillations in a frictionless two-stratified ocean without horizontal limitation are derived by Krauss (1957) [42] and measurements of large-amplitude waves in the ocean are presented, Krauss (1958) [43]. Magaard (1965) [52] derives exact wave equations for non-stationary two-dimensional internal waves of finite amplitude in incompressible continuously stratified media, where a first integral is found identical to Long's equation (1953) [47] for stationary lee-waves.

Linear wave theory of inertial and internal waves is thoroughly presented in the work by Krauss (1973) [44] and a comprehensive introduction to internal wave characteristics as well as examples are presented by Lighthill (1967) [46].

In general solitary waves in stratified fluids can be characterized by the depth of the fluid – ranging from shallow to deep - and the magnitude of nonlinearity, which is related to the amplitude of the disturbance. Small amplitude disturbances are treated in a weakly nonlinear long wave approximation, typically leading to a Korteweg-de Vries (KdV) type of equation for shallow fluids, or to the intermediate depth equation for deep fluids (see, for instance the recent review by Grimshaw (1997) [30]). Inclusion of higher-order terms in the asymptotic expansion enables the theory to be extended to larger amplitude disturbances. For instance Gear and Grimshaw (1983) [24] have extended the theory for shallow fluids to second order. However, this amplitude expansion approach is generally not suitable for large amplitude waves, and in particular fails to generate solutions with vortex cores, which are commonly observed in natural flows

and tank experiments. Further, the analysis of Pelinovsky and Grimshaw (1997) [57] indicates that solitary waves of large amplitudes may be unstable, and evolve into structures with vortex cores. The steady flow of a uniformly stratified, incompressible and inviscid fluid in a channel of finite depth was first studied extensively by Long (1953) [47]. Long independently derived a nonlinear equation commonly referred to as Long's equation, which was originally obtained by Dubreil-Jacotin (1937) [19]. Long's equation is applicable for the study of steady solitary waves in a stratified, incompressible and inviscid fluid, when the solution has no closed streamlines, and there is no upstream influence on the flow. McIntyre (1972) [54] discusses Long's hypothesis of no upstream influence in uniformly stratified or rotating flow.

Long's equation is linear for uniform stratification in the Boussinesq approximation yielding an equation similar to that for linear waves (Chan *et al* (1982) [39], Tung *et al* (1982) [66], Leonov and Miropol'skiy (1975) [45]). It follows that solitary waves are then precluded. While for incompressible fluids and uniform stratification the Boussinesq approximation removes the existence of solitary waves, Long and Morton (1966) [51] and Grimshaw (1980/81) [28] have shown that allowance of the slightest compressibility makes solitary waves possible. Grimshaw (1980) [28] derives evolution equations for long nonlinear internal waves in compressible fluids, with the aim of comparing these equations to their counterparts in incompressible fluids. Both the KdV and the intermediate depth equation are discussed for dry and moist atmospheres. It is shown that the effects of compressibility, or non-Boussinesq terms, are generally small, but measurable and are manifested mainly in the nonlinear term of the evolution equation. Grimshaw (1969) [27] derives integral constraints for steady recirculating flows of nearly incompressible fluids, arising from the action of a small amount of viscosity and heat conduction. He shows that waves with recirculation regions are isothermal, vorticity is constant and that there is an analogous result for an axially symmetric flow.

Although Long's equation is linear in the Boussinesq approximation for uniform stratification a small departure from the Boussinesq approximation, or a small departure from uniform stratification again make solitary waves possible (see, for instance, Benney

and Ko (1978) [5], Grimshaw and Yi (1991) [32]). For a fluid of finite depth with rigid top and bottom boundaries, the absence of recirculation regions limits Long's equation to the study of waves of amplitudes less than a critical amplitude, for which a stagnation point is situated at the upper boundary for a wave of depression (and at the lower boundary for a wave of elevation). Note that waves of depression are considered henceforth; waves of elevation are analogous. For amplitudes greater than the critical amplitude a vortex will be generated near the upper boundary. The appearance of closed streamlines terminates the strict validity of solutions to Long's equation, but Derzho and Grimshaw [DG] (1997) [16] have shown that the range of solitary wave solutions of Long's equation can be extended to solutions possessing vortex cores. The usual solitary wave solution valid in the outer region is matched to another solution in the inner region, thereby extending the study of solitary waves to amplitudes in excess of the critical amplitude. To achieve this, it is necessary to include a small vortex core region near the upper boundary, in which the flow is stagnant to leading order. The solutions so obtained exhibit amplitude-width relationships characteristic for observed large amplitude waves, which are known to possess closed streamlines and a pocket of recirculating flow; the width of the disturbance increases with amplitude.

In the Boussinesq approximation and for uniform stratification Long's equation is linear, without restriction to the wave amplitude. Solitary waves can then only be generated by a deviation from these conditions, as shown by Derzho and Grimshaw (1997) [16] , although waves resembling solitary waves may sometimes be generated by topography. Grimshaw and Yi (1991) [32] derive an unsteady fully nonlinear, weakly dispersive equation encompassing small departures from the case of the Boussinesq approximation with uniform stratification, which also includes the effects of localized topography. Rottman *et al* (1996) [58] report a detailed investigation, using numerical simulations of the fully nonlinear unsteady equations in the Boussinesq approximation for a uniform stratification, and compare their results to solutions of the finite-amplitude long-wave equation (FALW) derived by Grimshaw and Yi (1991) [32].

In this study the inertial terms neglected in the Boussinesq approximation (called

| | Source of Nonlinearity |
|---|---|
| Boussinesq Approximation* | deviation from uniform (linear) stratification $N^2 = N_0^2 + g\sigma^2 f(z)$, (N=Brunt-Väisälä frequency) and/or topography |
| non-Boussinesq | combination of deviation from uniform stratification and inertial effects and/or topography |

Table 1.1: *Table of the sources of nonlinearity for the stratified flow in a channel. (*) The Boussinesq approximation can be regarded as the zeroth order in a perturbation expansion of all primitive variables. Note: a deviation from uniform flow (ie. shear flow, $U \neq const$) introduces nonlinearity too.*

non-Boussinesq effects in the sequel) are included. For this purpose, a novel numerical model is developed to model the time-dependent fully nonlinear governing equations for incompressible, inviscid stratified flow in a channel of finite depth including the non-Boussinesq terms. This part of the study thus aims to verify, firstly, the FALW equation for flow over topography and secondly, the asymptotic theory of Derzho and Grimshaw (1997) [16] [DG] for large-amplitude internal solitary waves with vortex cores. Brown and Christie (1998) [11] present fully nonlinear internal solitary waves with vortex cores in a continuously stratified incompressible inviscid, shear free Boussinesq fluid, but do not include a different governing equation for the recirculation region. Numerical experiments suggest that such waves are not stable since the same equation was used in deriving the solution outside and inside the recirculation region.

Three sources of nonlinearity supporting the existence of solitary waves, or solitary-like waves can be identified. First, the nonlinearity induced by the deviation from uniform stratification in the Boussinesq approximation. Second, the nonlinearity induced by the non-Boussinesq terms and third, the role of the bottom topography (see Table 1.1).

Subsequently, the aforementioned numerical model will be employed to study multi-scaled internal solitary waves. Multi-scale solitary waves are solitary waves usually governed by a generalized Korteweg-de Vries type equation and resemble an isolated

hump situated on a bigger wider hump. Multi-scale internal solitary waves have been derived by Derzho and Velarde (1995) [17] for the case of a shallow stratified fluid with a free surface. Capillary dispersion and gravitational nonlinearity are considered to represent the prevalent nonlinear balance necessary. See Benjamin (1992) [4] for solitary waves in a two-fluid system and an interface subject to capillarity. In this study, the internal solitary waves are derived in a channel of finite depth with no flow boundary conditions. The derivation of multi-scale internal solitary waves is motivated by the experimental observation of bore-like waves with smaller scaled solitary waves located on top. The purpose of this part of the study is to show that solitary waves of such type exist and are of permanent shape.

*Inertial solitary waves*

Apart from internal solitary waves, this study also focuses on large-amplitude inertial solitary waves with vortex cores in an axisymmetric rotating fluid flowing through a cylindrical channel. The interest in a rotating fluid – commonly known as swirl flow – stems from the stabilizing effect of a rotating flow on high intensity combustion in engines, gas turbines, industrial furnaces and many more propulsion mechanisms. Of particular interest is the optimization of performance, stability, combustion intensity of flames and the reduction of pollution of aforementioned technological applications, see Gupta (1984) [33].

The existence of a recirculation zone can improve the efficiency of the burning process in the combustion chamber, when the propagation velocity of the flame front equals the propellant flow at the inflow opening of air where a sudden expansion in the cylindrical channel exists. The recirculation zone is utilized as a flame stabilization by providing an efficient burning region. The similarity of recirculation zones to vortex breakdown effects is noted here; see Benjamin (1978) [3] for more details on the vortex breakdown phenomenon.

Recirculating regions in fluids are generated by sudden expansions in pipes and are propagated downstream for great lengths, Vennard (1961) [67]. Oswatitsch (1956) [56]

discusses the gas dynamical context of the abrupt expansion of a channel. A closely related occurence is cavitation behind a disk. The accompanying discontinuity surface between the recirculation region and the main flow can create a low pressure surface with a pressure below the vapor pressure of the fluid causing it to vaporize. The resulting cavities greatly diminish the preformance of the system and can result in erosion of the structures, Streeter and Wylie (1975) [63].

This study examines the unsteady behaviour of the large-amplitude solitary wave solutions derived by Derzho and Grimshaw [15] [DG] by solving the fully nonlinear time-dependent equations for an axially-symmetric rotating inviscid, incompressible flow through a cylindrical cylinder. For this purpose a novel numerical model is developed. The steady-state solutions derived by DG utilize the Bragg-Hawthorne equation (1950) [9] for vorticity, for which circulation and head are invariants along streamlines. The Bragg-Hawthorne equation, for a rotating flow in a cylindrical axisymmetric geometry, uniquely defines all those streamlines originating upstream. The introduction of a re-circulation zone necessitates the subdivision of the domain and the use of a modified governing equation for the region of fluid where closed streamlines exist, similar to the case of stratified flow.

In the limit of exact uniform inflow conditions the Bragg-Hawthorne equation is linear, thus precluding the existence of solitary wave solutions. However, DG showed that small departures from uniformity in the inflow conditions can provide the nonlinearity needed to obtain solitary waves. Further DG showed that the solutions can be extended in amplitude to contain recirculation zones. The situation is closely related to large-amplitude solitary waves with vortex cores in a stratified fluid. In fact, the derivation is analogous. Instead of the Dubreil-Jacotin-Long equation, which is linear for uniform stratification in the Boussinesq approximation, the flow is governed by the Bragg-Hawthorne equation.

Hence the rotating flow can be compared to the stratified flow. The centripetal force has a similar role to the gravitational force for stratified flow. Likewise, the sources of nonlinearity for the generation of solitary waves can be deduced, as was done for the

stratified flow. Sources of nonlinearity are the deviation from uniform axial and rotating flow as well as topography. Grimshaw (1990) [29] considers the flow of a rotating fluid past an axisymmetric obstacle placed on the axis of a cylindrical channel. The amplitude function satisfies a forced KdV equation when the upstream flow contains radial shear and/or radially dependent angular velocity. Thus solitary like waves are generated. Grimshaw and Yi (1993) [31] show that for the case of a flow with uniform angular velocity an equation different to a forced KdV equation is needed, similar to the finite-amplitude long-wave equation (FALW) for stratified flow over topography [32].

*Outline*

This study develops novel numerical methods to integrate the time-dependent fully non-linear governing equations for the stratified flow in a channel including topography, as well as the fully nonlinear equations for the rotating flow through a cylindrical channel. The main purpose is to verify the existence and permanence of large-amplitude internal and inertial solitary waves with vortex cores in these settings. Numerical evidence for the existence and permanence of large-amplitude solitary waves is provided by considering the long-time behaviour of characteristic quantities such as shape, maximum amplitude, phase speed and maximum adverse velocity at the top of the recirculation region. The aim is to provide quantitative results substantiating the validity of the solutions derived by Derzho and Grimshaw (1997) [16, 15]. Moreover results for the generation of large-amplitude internal solitary waves by topography and multi-scaled internal solitary waves are presented for the fully nonlinear equations.

In order to model the fully nonlinear unsteady governing equations for stratified flow – including the non-Boussinesq terms – a novel numerical method is proposed to solve the discrete elliptic problem arising from the inviscid equations. It consists of a high-resolution pseudospectral method based on the scheme used by Rottman *et al* (1996) [58] for spatial integration and a low-storage Runge-Kutta method for temporal integration coupled with a Liouville-Neumann iteration for the solution to a fixed-point problem. The simulations allow comparison of the fully nonlinear equations

with the finite-amplitude long-wave model of Grimshaw and Yi (1991) [32], and the large-amplitude solitary waves with vortex cores of DG.

The numerical technique developed for the rotating flow consists of the solution of a generalized Poisson equation using direct methods and a pseudospectral scheme for the spatial integration coupled with a Runge-Kutta method for the temporal integration. Alternate methods for solving the generalized Poisson equation based on finite difference iterative methods will be described and their capabilities related to the direct method used.

This study is organized into seven chapters. The second chapter introduces the time-dependent governing equations for the stratified flow in a channel of finite depth in the Boussinesq approximation, as well as the fully-nonlinear non-Boussinesq case. The equations for the rotating flow through a cylindrical channel are also stated. In chapter three the theoretical asymptotic solutions are derived. The applications being the large-amplitude internal solitary waves with vortex cores in the stratified flow for the Boussinesq and non-Boussinesq case, the multi-scale internal solitary waves and the rotating flow. The finite-amplitude long-wave equation derived by Grimshaw and Yi (1991) [32] is described briefly. In the fourth chapter the novel numerical methods derived throughout the course of this study are presented, the model for the stratified flow in a channel and the model for the rotating flow through a cylindrical channel, followed by the numerical results for all four applications in chapter five. Chapter six provides the conclusion of this study followed by the Appendix.

# Chapter 2

# Governing Equations

In this chapter, the governing equations are discussed for the case of a density-stratified uniform flow through a channel of finite depth, encompassing the equations in the Boussinesq approximation and including the terms neglected in the Boussinesq approximation, which will be called non-Boussinesq subsequently. Followed by the governing equations for the rotating flow of a constant density fluid through a cylindrical channel.

## 2.1 Stratified flow in a channel of finite depth

Consider a two-dimensional inviscid incompressible fluid of undisturbed depth $D$, with rigid upper and lower boundaries. The governing equations in standard notation are,

$$\rho\{u_t + \vec{u} \cdot \nabla u\} + p_x = 0, \tag{2.1}$$

$$\rho\{w_t + \vec{u} \cdot \nabla w\} + p_z + \rho g = 0, \tag{2.2}$$

$$\rho_t + \vec{u} \cdot \nabla \rho = 0, \tag{2.3}$$

$$\nabla \cdot \vec{u} = 0. \tag{2.4}$$

The perturbation velocity $u$ in the $x-$direction, is relative to a uniform flow $U$, so that the $x-$component of $\vec{u}$ is $U + u$. The continuity equation (2.4) is satisfied by introducing a perturbation streamfunction $\psi$ such that $u = -\psi_z$, $w = \psi_x$. Next, eliminating the pressure $p$ it follows that,

$$D_t \Delta \psi + \frac{\rho_x}{\rho}(g + D_t \psi_x) + \frac{\rho_z}{\rho} D_t \psi_z = 0, \tag{2.5}$$

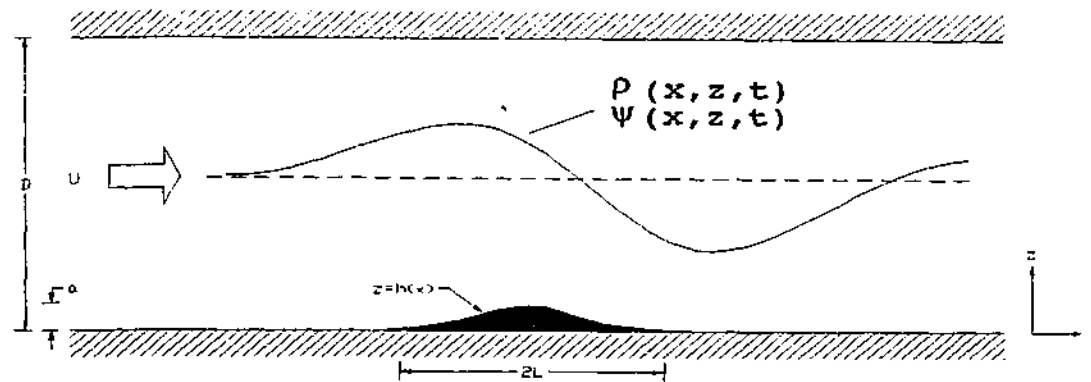$$D_t \rho' + w \bar{\rho}_z = 0, \tag{2.6}$$

Figure 2.1: Sketch of the geometry for the two-dimensional flow of undisturbed depth $D$. The uniform background flow is denoted by $U$. The functions $\rho(x, z, t)$, $\psi(x, z, t)$ represent surfaces of constant density and streamfunction respectively. The undisturbed level is indicated by the dashed horizontal line. The elevation of the topography is given by $z = h(x)$ and its maximum height by $a$. The characteristic length scale of the topography is $L$. Note that for the case of the solitary waves with vortex cores the uniform flow is reversed and the topography vanishes, i.e. $a = 0$.

where the total derivative is given by

$$D_t = \frac{\partial}{\partial t} + U \frac{\partial}{\partial x} + J(\psi, \cdot), \tag{2.7}$$

$J(\cdot, \cdot)$ is the Jacobian defined by $J(a, b) = a_x b_z - a_z b_x$, and the total density $\rho$ is defined by

$$\rho(x, z, t) = \bar{\rho}(z) + \rho'(x, z, t). \tag{2.8}$$

The vorticity $\omega$ is given by $\omega = w_x - u_z = \Delta \psi$.

Figure 2.1 shows a sketch of the geometry. Note that the topography is included in the diagram, but vanishes for the case of the large-amplitude solitary waves with vortex cores. The boundary conditions are

$$\psi = 0 \quad \text{on} \quad z = h(x), \tag{2.9}$$

$$\psi = U \quad \text{on} \quad z = D, \tag{2.10}$$

ensuring that there is no flow through the boundaries. When there is no topography present the function for the shape of the hill is set to zero, $h = 0$. To identify the Boussinesq approximation, it is appropriate to introduce the parameter $\kappa$, which is chosen such that the non-Boussinesq case is represented by $\kappa = 1$, and the equations
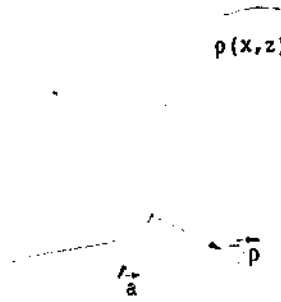
$\rho(x,z)$

Figure 2.2: The last term in equation (2.11) can be thought of as the vector product of the density gradient $\vec{\nabla}\rho = (\rho_x, 0, \rho_z)$ with the acceleration of fluid particles $\vec{a} = (a_1, 0, a_3)$, given by $\vec{\nabla}\rho \times \vec{a}$. Notice that since the flow is two dimensional the vorticity vector $\vec{\omega} = \omega\,\mathbf{j}$ has only one component in the y-direction.

in the Boussinesq approximation by $\kappa = 0$. Thus the vorticity equation (2.5) can be written as

$$\omega_t = -U\omega_x - J(\psi, \omega) - \frac{\rho_x}{\rho_0 + \kappa(\rho - \rho_0)}g - \frac{\kappa}{\rho_0 + \kappa(\rho - \rho_0)}\left\{\rho_x \frac{D\psi_x}{Dt} + \rho_z \frac{D\psi_z}{Dt}\right\}. \quad (2.11)$$

The last term in equation (2.11) represents the inertial contribution to the vorticity equation, see Figure 2.2. It contains the variation of the velocities with time and space, and is neglected in the Boussinesq approximation. Furthermore, in the Boussinesq approximation, the total density $\rho = \rho_0 + \kappa(\rho - \rho_0)$ is set to a reference density $\rho = \rho_0$, except where it acts as the gravitational term, which is the case for $\kappa = 0$ in equation (2.11).

This term is retained in the non-Boussinesq case, which means that vorticity is generated by a nonzero horizontal density gradient, as is the case in the Boussinesq approximation, and also by a variation in the horizontal and vertical velocity components, that is, inertial terms in the horizontal and vertical directions.

The variation in the perturbation density is given by equation (2.6), or in full,

$$\rho'_t = -U\rho'_x - J(\psi, \rho') - \psi_x \bar{\rho}_z. \quad (2.12)$$

Note that the bouyancy frequency $N(z)$ is defined by $N^2 = -g\bar{\rho}_z/\rho_0$ and is constant in the Boussinesq approximation for uniform stratification. For the case of the flow over topography the initial conditions are that $\psi = 0$ and $\rho' = 0$ at $t = 0$. Together with the

boundary conditions (2.9) and (2.10), these represent the case of an impulsively acceler-ated obstacle, and mimic the initial conditions in tow-tank experiments in a laboratory. The isopycnal surfaces are initially horizontal, and thus intersect the obstacle surface. This creates a small region of non-uniform distribution of density at the bottom bound-ary, which is swept rapidly downstream after the flow is initiated. The spectral filter that is used filters out these modes and leaves the main flow behaviour unaltered. This small abnormality is seen in all results, yet gives no further reasons for concern, since the long-time behaviour near the obstacle is not affected (for a detailed description see Rottman *et al* (1996) [58]).

The propagating solitary wave solutions considered here are viewed in a reference frame moving with the wave, this is achieved by setting the background flow $U$ to the phase speed of the wave $U = c$.

The governing equations for vorticity and density perturbation in the Boussinesq approximation in explicit form are given by

$$\omega_t = -U\omega_x - J(\psi, \omega) - \sigma_x^*, \tag{2.13}$$

$$\sigma_t^* = -U\sigma_x^* - J(\psi, \sigma^*) + w \cdot N^2, \tag{2.14}$$

where

$$\sigma^* = g\frac{\rho'}{\rho_0}. \tag{2.15}$$

## 2.2 Rotating flow in a cylindrical channel

Consider the axisymmetric flow of an inviscid, incompressible swirling fluid of constant density, confined to a channel of circular cross-section. In standard notation the equa-tions for the unsteady flow through the cylindrical channel are,

$$u_t + uu_x + vu_r + p_x = 0, \tag{2.16}$$

$$v_t + uv_x + vv_r - \frac{w^2}{r} + p_r = 0, \tag{2.17}$$

$$w_t + uw_x + vw_r + \frac{vw}{r} = 0, \tag{2.18}$$

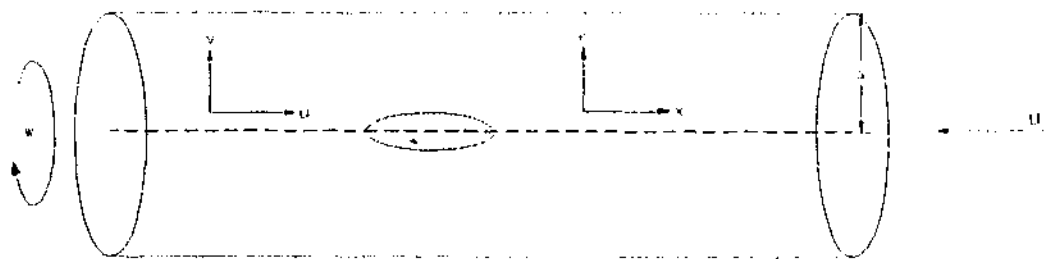$$u_x + \frac{1}{r}(rv)_r = 0. \tag{2.19}$$

Figure 2.3: This diagram shows the coordinate system for the rotating flow in a cylindrical channel of radius $a$. $U$ is the uniform flow, $w$ the rotational velocity and $u$, $v$ the axial and radial velocity respectively. The coordinate axes are $x$, $r$ and $\theta$ which is directed along the circumference of a cylinder of radius $r = const$.

The coordinates are $(x, r, \theta)$ with x being in the axial direction, r in the radial direction and $\theta$ in the azimuthal direction, see Figure 2.3, $(u, v, w)$ are the corresponding velocity components, and $p$ is the pressure. Eliminating the pressure, $p$, using $u = \psi_r/r$ and $v = -\psi_x/r$ yields a vorticity equation and an equation for the circulation $C = wr$

$$\Gamma_t = \frac{1}{r}J(\psi, \Gamma) - 2\frac{CC_x}{r^4}, \tag{2.20}$$

$$C_t = \frac{1}{r}J(\psi, C), \tag{2.21}$$

where

$$\Gamma = \frac{1}{r^2}\{\psi_{xx} + \psi_{rr}\} - \frac{\psi_r}{r^3}.$$

Note that the solitary wave solutions will be viewed in a reference frame moving with the phase speed of the wave.

# Chapter 3

# Applications

This section describes the four applications that are considered. For the case of stratified flow through a channel the large-amplitude internal solitary waves with vortex cores are derived, a short summary of the finite-amplitude long-wave equation for flow over topography derived by Grimshaw and Yi (1991) [32] is given, followed by the construction of multi-scaled internal solitary waves. In the fourth subsection the large-amplitude inertial solitary waves with vortex cores in a rotating constant-density fluid are derived.

## 3.1 Large-amplitude internal solitary waves with vortex cores

For a reference frame moving with the wave in the positive x-direction at the phase speed $U = c$ a modified streamfunction $\phi(x, z)$ for steady flow can be introduced,

$$\psi(x, z) = -U z + \phi(x, z). \tag{3.1}$$

Then, for steady flow, equation (2.3) for conservation of density implies that

$$\rho = \rho(\phi). \tag{3.2}$$

Elimination of the pressure between the momentum equations (2.1,2.2) and making use of the transformation (3.1) yields a single equation for the streamfunction $\phi$

$$(J(\phi_x, \phi) + g) \frac{\partial q}{\partial x} + J(\phi_z, \phi) \frac{\partial q}{\partial z} = -J(\Delta \phi, \phi) \qquad \text{with} \qquad q = \ln \rho.$$

Using equation (3.2) this can be written as

$$\left\{ g \frac{\partial \phi}{\partial x} + \frac{1}{2} J \left[ \left( \frac{\partial \phi}{\partial x} \right)^2 + \left( \frac{\partial \phi}{\partial z} \right)^2, \phi \right] \right\} \frac{1}{\rho} \frac{d\rho}{d\phi} + J(\Delta \phi, \phi) = 0$$

or

$$J \left[ \phi_{xx} + \phi_{zz} + \frac{1}{\rho} \frac{d\rho}{d\phi} \left( g\, z + \frac{1}{2} \left( \phi_x^2 + \phi_z^2 \right) \right), \phi \right] = 0,$$

where $J$, the Jacobian operator, is given by $J(A, B) = A_x B_z - A_z B_x$. It follows that for a vorticity function $\mathcal{G}(\phi)$, determined from upstream conditions, the streamfunction $\phi$ has to satisfy the following nonlinear equation, derived by Dubreil-Jacotin (1937) [19],

$$\phi_{xx} + \phi_{zz} + \frac{1}{\rho} \frac{d\rho}{d\phi} (\, g\, z + \frac{1}{2} \left( \phi_x^2 + \phi_z^2 \right)\,) = \mathcal{G}(\phi), \tag{3.3}$$

its equivalent to Long's equation for nonlinear leewaves for $c = 0$ [47]. The functions $\mathcal{G}$ and $\rho(\phi)$ can be obtained on those streamlines originating upstream, where we assume that $\psi \to 0$, so that

$$\phi \;\; \to \;\; c\, z, \tag{3.4}$$

$$\rho \;\; \to \;\; \bar{\rho}(z), \tag{3.5}$$

where $\bar{\rho}(z)$ is the basic density profile. It follows that

$$\rho(\phi) \;\; = \;\; \bar{\rho}(\phi/c), \tag{3.6}$$

$$\mathcal{G}(\phi) \;\; = \;\; \frac{1}{\rho} \frac{d\rho}{d\phi} \left( \frac{g\, \phi}{c} + \frac{1}{2} c^2 \right). \tag{3.7}$$

Dimensionless coordinates are introduced based on the height of undisturbed fluid $D$ and the phase speed $c$,

$$\phi' = \frac{\phi}{c\, D}, \qquad x' = \frac{x}{D}, \qquad z' = \frac{z}{D} \tag{3.8}$$

and consider a basic density field close to uniform stratification

$$\bar{\rho}(z') = \rho_0 (1 - \sigma\, z' - \sigma^2 f(z')), \tag{3.9}$$

where $\rho_0$ is the reference density, having a value typical for water. Omitting the prime superscripts subsequently the non-dimensionalisation (3.8) and the basic density field (3.9) transforms equation (3.3) into the following equation, which, after omitting the prime superscripts, is given by

$$\phi_{xx} + \phi_{zz} + \lambda\, (\phi - z)(1 + \sigma\, f_\phi(\phi) + \sigma\, \phi) - \frac{1}{2} \sigma\, (\phi_x^2 + \phi_z^2 - 1) + \mathcal{O}(\sigma^2) = 0, \tag{3.10}$$

where the eigenvalue $\lambda$ is given by

$$\lambda \doteq \frac{\sigma g D}{c^2}. \tag{3.11}$$

Here $\lambda$ is an inverse Froude number, and scales with unity with respect to the small parameter $\sigma$, which characterizes the weak stratification. The boundary conditions, corresponding to equations (2.9,2.10), are

$$\phi_x = 0 \qquad \text{on} \qquad z = 0,1 \tag{3.12}$$

$$\phi \sim z \qquad \text{as} \qquad x \to \pm\infty. \tag{3.13}$$

Equations (3.10,3.12,3.13) provide a complete formulation of the problem if all streamlines originate upstream, thus excluding the possible presence of a recirculation region.

### Derivation of the steady solitary wave solutions

The steady solitary wave solutions are derived by introducing the stretched variable $X = \epsilon x$ and scaling the stratification parameter $\sigma$ with $\epsilon^2$. Thus an asymptotic expansion of $\phi$ and $\lambda$ in terms of $\epsilon^2$ is substituted into the governing equation (3.10)

$$\phi(X,z) \sim \sum_{k=0}^{\infty} \epsilon^{2k} \phi^{(k)}(X,z), \tag{3.14}$$

$$\lambda \sim \sum_{k=0}^{\infty} \epsilon^{2k} \lambda^{(k)}, \tag{3.15}$$

which yields the zeroth order solution, $\phi^{(0)} = z + A(X)\sin n\pi z$ and $\lambda^{(0)} = \pi^2$. Here only the first mode $n = 1$ is considered. A secularity condition applied at the next order then gives the amplitude equation,

$$A_X^2 + \lambda^{(1)} A^2 + \kappa\frac{4}{3}\pi A^3 + 2\int_0^A M(A')dA' = 0. \tag{3.16}$$

The nonlinear function $M(A)$ is given by

$$M(A) = 2\pi^2 \int_0^1 A \sin^2(\pi z) f_\phi(z + A\sin(\pi z))dz. \tag{3.17}$$

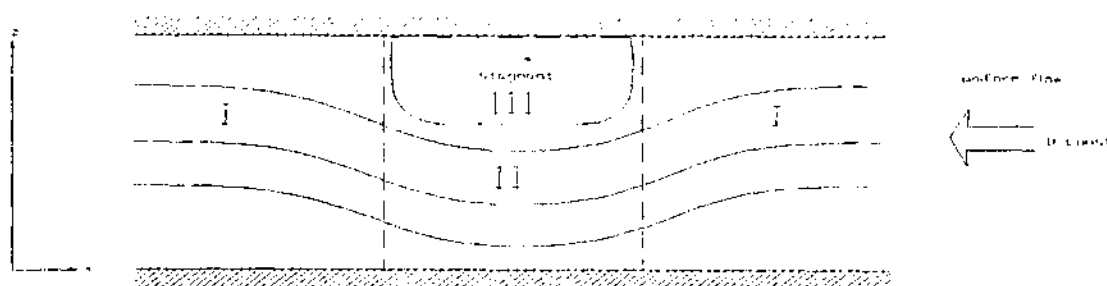Note that the parameter $\kappa$ is zero in the Boussinesq approximation and unity otherwise.

Figure 3.1: Schematic picture of the three zones: (I) outer zone, (II) inner zone and (III) recirculation zone. The recirculation region can be assumed to be stagnant to leading order.

### Solution to the Inner Region

Equation (3.16) holds in the whole $x$–domain when the amplitude $A$ is less than the maximum possible amplitude $A_* = \frac{1}{\pi}$, for which no recirculation region exists, i.e. $A < A_*$. However, if $A = A_*$ at some point $|X| = X_0$ (where the centre of the wave is situated at the origin of the x-axis for convenience) on the wave profile, then there is an incipient flow reversal, and in the region $|X| < X_0$, an asymptotic solution containing a vortex core needs to be constructed. Thus, three regions of the domain can be identified, each of which has a different asymptotic solution. First, the outer zone – denoted by (I) in Figure 3.1, secondly the inner zone – denoted by (II), and the recirculation region itself – denoted by (III).

The recirculation region can be assumed to be stagnant to leading order, as was shown by DG. The streamfunction is set to $\psi = const.$ inside the recirculation region, since the theoretical structure is not known. Yet the physical flow has of course no discontinuity in the horizontal velocity $u$ at the boundary between zone (II) and (III), see Figure 3.2. The resultant change in the solution for a smoothed matching between the solutions of zone (II) and (III) is small, and since it does not cause numerical instability, it is omitted.

The solution in zone (II) is found by introducing a perturbation to the maximum amplitude $A_*$,

$$A(\xi) = A_* + \mu\, B(\xi) \qquad \text{with} \qquad 0 \le B(\xi) \le 1, \tag{3.18}$$
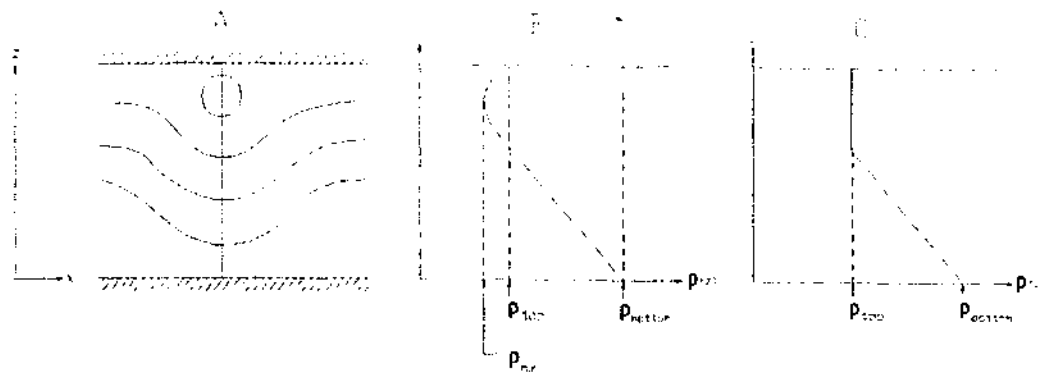
Figure 3.2: Schematic picture of A) the coordinate system for the stratified flow in a channel, B) cross-section of the density field at the center of the recirculation zone, with non-zero vorticity and static instability of the density field and C) the same as B) but with constant density. The fluid inside the recirculation region is stagnant to leading order, thus streamfunction and density are constant inside the recirculation region to leading order.

where $\xi = \varsigma x$ is the stretched variable for zone (II). Since $\epsilon \ll \varsigma$, it follows that $\mu\varsigma^2 = \epsilon^2$ and the total length scale of the recirculation region tends to zero as $\mu \to 0$. Further details of the balance of parameters are omitted here, since they can be found in DG. Substituting equation (3.18) into equation (3.14), together with the condition that the streamfunction $\phi$ and the pressure have to be continuous across the vortex core boundary, yields an approximative equation for $B(\xi)$, again using an appropriate secularity condition,

$$B_\xi^2 = R(A_*)\left[1 - B\right] - \frac{8\nu}{15}\left[1 - B^{\frac{5}{2}}\right], \tag{3.19}$$

where

$$R(A_*) = \kappa\frac{4}{3}\pi A_*^2 + 2M(A_*) - \frac{4}{A_*}\int_0^{A_*} M(A')dA' \tag{3.20}$$

and

$$\nu = \frac{(2\pi\mu)^{\frac{3}{2}}}{\epsilon^2}. \tag{3.21}$$

For a solution to exist the right-hand side of equation (3.19) must be positive. This yields a bound on $\nu$ and $\mu$, which in turn places an upper bound on the maximum possible amplitude, that is,

$$\nu < \nu_{max} = \frac{3}{4}R(A_*) \quad , \quad \mu < \mu_{max} = \frac{\epsilon^{\frac{4}{3}}}{2\pi}\nu_{max}^{\frac{2}{3}}, \tag{3.22}$$

$$A_{max} = A_* + \mu_{max}. \tag{3.23}$$

The eigenvalue $\lambda^{(1)}$ is given by

$$\lambda^{(1)} = -\frac{1}{A_*^2}\left[\kappa\frac{4}{3}\pi A_*^3 + 2\int_0^{A_*} M(A')dA' + \mu\left(R(A_*) - \frac{8\nu}{15}\right)\right]. \qquad (3.24)$$

Suppose that the function $f(z')$ is given by

$$f(z') = \alpha_1 z' + \alpha_2 z'^2 + \alpha_3 z'^3, \qquad (3.25)$$

so that equations (3.17,3.20,3.24) yield

$$M(A) = \frac{9\pi^2}{4}\alpha_3 A^3 + 8\pi\left(\alpha_3 + \frac{2}{3}\alpha_2\right) A^2, \qquad (3.26)$$

$$R(A_*) = \frac{9\pi^2}{4}\alpha_3 A_*^3 + \frac{4\pi}{3}\left(\kappa + 4\alpha_3 + \frac{8}{3}\alpha_2\right) A_*^2, \qquad (3.27)$$

and

$$\lambda^{(1)} = -\left(\kappa\frac{4}{3} + \frac{32}{9}\alpha_2 + \frac{155}{24}\alpha_3\right)\pi A_{max} - \frac{9\pi}{8}\alpha_3\,\mu + \frac{2}{15}\frac{(2\pi)^{\frac{7}{2}}}{\epsilon^2}\mu^{\frac{5}{2}}, \qquad (3.28)$$

where $\alpha_1$ is chosen conveniently to remove the linear term in $M(A)$,

$$\alpha_1 = -\alpha_2 - \left(1 - \frac{3}{2\pi^2}\right)\alpha_3. \qquad (3.29)$$

Introducing $\iota^2 = -\lambda^{(1)}$ equation (3.16) becomes

$$A_X^2 - \iota^2 A^2 + \tau_1 A^3 + \tau_2 A^4 = 0, \qquad (3.30)$$

where

$$\tau_1 = \frac{4\pi}{3}\left(\kappa + 4\alpha_3 + \frac{8}{3}\alpha_2\right) \qquad \text{and} \qquad \tau_2 = \frac{9\pi^2}{8}\alpha_3. \qquad (3.31)$$

Equation (3.30) can be readily solved. In the following the two cases of a Korteweg-de Vries (KdV) ($\tau_2 = 0$) and modified KdV outer solution ($\tau_1 = 0$) are considered, which is then matched to the inner solution obtained by solving for $B$ in equation (3.19).

1. Equation (3.30) simplifies to the KdV equation for $\tau_2 = 0$ ($\alpha_3 = 0$), which has the solution

$$A = \frac{\iota^2}{\tau_1} \operatorname{sech}^2\frac{\iota}{2}(|X| - X_*). \qquad (3.32)$$

2. For $\tau_1 = 0$ equation (3.30) reduces to the mKdV equation which has the solution

$$A = \frac{\iota}{\sqrt{\tau_2}} \operatorname{sech}\iota(|X| - X_*). \qquad (3.33)$$

The matching conditions $X_*$ for these two cases are given by

$$X_* = |X_0| - \frac{2}{\iota} \ln \left( \iota \sqrt{\frac{\pi}{\tau_1}} + \sqrt{\iota^2 \frac{\pi}{\tau_1} - 1} \right) \qquad \text{for} \qquad \tau_2 = 0, \qquad (3.34)$$

and

$$X_* = |X_0| - \frac{1}{\iota} \ln \left( \iota \frac{\pi}{\sqrt{\tau_2}} + \sqrt{\iota^2 \frac{\pi^2}{\tau_2^2} - 1} \right) \qquad \text{for} \qquad \tau_1 = 0. \qquad (3.35)$$

Here $X_0 = \epsilon x_0$, is the halfwidth of the recirculation region, which is found by solving equation (3.19).

The phase speed of the solitary waves is given by

$$c = \sqrt{\frac{\sigma g D}{\lambda}} \qquad (3.36)$$

and the linear phase speed is given by $c_0 = \sqrt{\sigma g D}/\pi$. To leading order the nonlinear phase speed can be approximated by

$$c = c_0 \left( 1 - \frac{\epsilon^2}{2\pi^2} \lambda^{(1)} + O(\epsilon^4) \right). \qquad (3.37)$$

For $\tau_2 = 0$, ie. $\alpha_3 = 0$, corresponding to the KdV outer solution, the eigenvalue $\lambda^{(1)}$ is

$$\lambda^{(1)} = -\tau_1 A_{max} + \frac{2}{15} \frac{(2\pi)^{\frac{7}{2}}}{\epsilon^2} \mu^{\frac{5}{2}}. \qquad (3.38)$$

If the recirculation region is absent equation (3.32) represents the solution over the entire domain. The eigenvalue $\lambda^{(1)}$ is then given by

$$A_{max} = \iota^2/\tau_1,$$

where since $\lambda^{(1)} = -\iota^2$,

$$\lambda^{(1)}_{KdV} = -\tau_1 A_{max}.$$

Dropping the $O(\epsilon^4)$ term in equation (3.37), the phase speed of the solution with the recirculating region can be expressed as

$$c_{GD}|_{\tau_2=0} = c_{KdV} - \frac{c_0}{\pi^2} \frac{(2\pi)^{\frac{7}{2}}}{15} \mu^{\frac{5}{2}}, \qquad (3.39)$$

where

$$c_{KdV} = c_0 \left( 1 + \frac{\epsilon^2}{2\pi^2} \tau_1 A_{max} \right), \qquad (3.40)$$

is the phase speed of the KdV solution without the recirculating region. Note that $c_{KdV}$ increases with amplitude $A_{max}$.

Considering the case $\tau_1 = 0$, one notices that the parameter $\kappa$ – which distinguishes the Boussinesq approximation from the non-Boussinesq case – is absent from equation (3.28). Thus the phase speed for the solution with the mKdV outer solution in the Boussinesq approximation ($\kappa = 0$) is the same as in the non-Boussinesq case ($\kappa = 1$). For $\tau_1 = 0$ the eigenvalue $\lambda^{(1)}$ becomes

$$\lambda^{(1)} = -\tau_2 \frac{1}{\pi}(A_{max} + \mu) + \frac{2}{15}\frac{(2\pi)^{\frac{7}{2}}}{\epsilon^2}\mu^{\frac{5}{2}}. \tag{3.41}$$

Similarly, if the recirculation region is absent, equation (3.33) is the amplitude equation for the entire domain and its eigenvalue $\lambda^{(1)}$ can be computed from

$$A_{max} = \iota/\sqrt{\tau_2}, \tag{3.42}$$

yielding

$$\lambda^{(1)}_{mKdV} = -\tau_2 A^2_{max} \tag{3.43}$$

for the eigenvalue and

$$c_{mKdV} = c_0 \left(1 + \frac{\epsilon^2}{2\pi^2}\tau_2 A^2_{max}\right) \tag{3.44}$$

for the phase speed. Note that the phase speed of the mKdV solution increases with $A^2_{max}$ in contrast to the KdV solution which increases with $A_{max}$ only. The phase speed of the solution with recirculating region is

$$c_{GD}|_{\tau_1=0} = c_0 \left(1 + \frac{\epsilon^2}{2\pi^2}\tau_2\frac{1}{\pi}(A_{max} + \mu) - \frac{c_0}{\pi^2}\frac{(2\pi)^{\frac{7}{2}}}{15}\mu^{\frac{5}{2}}\right) \tag{3.45}$$

The relative phase speed

$$(c_{GD} - c_0)/c_0$$

for the two outer solutions (KdV/mKdV) considered and the Boussinesq and non-Boussinesq case ($\kappa = 0/\kappa = 1$) is plotted in Figures 5.1 and 5.12 for the case of a KdV outer solution together with the phase speed of the conventional KdV solution. Figure 5.2 shows the phase speed for the mKdV outer solution together with the corresponding conventional mKdV phase speed for $\kappa = 0$. The GD solutions are of the order $O(10^{-3})$

and $O(10^{-2})$ slower than the phase speed of the KdV and mKdV solutions and faster than the speed of the linear long wave (see equation (3.40)). Also the width of the initial streamfunction field increases with amplitude, see Figure 5.3. Note that in the KdV case $\lambda^{(1)} = -\tau_1/\pi + O(\mu)$, and in the mKdV case $\lambda^{(1)} = -\tau_2/\pi^2 + O(\mu)$. Thus in both cases $X_* - |X_0|$ is $O(\mu^{1/2})$, which is required for consistency with the scaling for the inner region.

## 3.2   Stratified flow over topography

In the numerical simulations, a Gaussian curve was chosen as the obstacle shape,

$$h(x) = ae^{-\frac{(x-x_0)^2}{L^2}}. \tag{3.46}$$

The dimensionless quantities based on the amplitude of the hill $a$, the depth of the fluid $D$, the horizontal dimension of the hill $L$ and the flow speed $U$ are introduced,

$$\frac{a}{D}, \qquad \frac{L}{D}, \qquad K = \frac{ND}{\pi U} \quad \text{and} \quad \beta = \frac{N^2 D}{g}, \tag{3.47}$$

where $N$ is the Brunt-Väisälä frequency and $\beta$ the Boussinesq parameter which defines the strength of the stratification, $K$ is the inverse Froude number and $g$ the gravitational constant. The resonant points are where $K = n$, with $n = 1, 2, \cdots$. Small values of $a/D$ and moderate values of $L/D$, with the inverse Froude number in the range $0.95 \leq K \leq 1.2$, are considered. Equations (2.5,2.6) together with the boundary conditions (2.9,2.10) complete the formulation.

### FALW model equation

Grimshaw and ⋯ (1991) [32] derived the finite-amplitude long-wave equation (FALW) for the resonant interaction of flow with topography. Moreover an improved numerical solution to the FALW equation was presented by Rottman et al. (1996) [58]. The FALW equation is given by

$$\int_{-\infty}^{x} G(A, A')\frac{\partial A'}{\partial t}dx' + (U - c_n)A - \frac{c_n^2}{N^2}\beta m(A) - \frac{1}{2}\frac{c_n^3}{N^2}\frac{\partial^2 A}{\partial x^2} - \frac{c_n^2}{ND}(1 - \frac{N}{c_n}A)h = 0. \tag{3.48}$$

The kernel $G(A, A')$ is a complicated function of $A$ and $A'$ given in [32, 58], where $A(x, t)$ is the amplitude of the $n^{th}$ linear long wave mode, and $c_n = ND/n\pi$ is the linear long wave phase speed. Equation (3.48) holds for amplitudes less than a certain critical amplitude, that is, $|A| < A_* = D/n\pi$ in dimensional form. The non-Boussinesq term in the FALW equation is included in $m(A)$, and is asymptotically given by

$$m(A) = 3A^2, \tag{3.49}$$

as the Boussinesq limit is approached $(\beta \to 0)$, see [32].

## 3.3 Multi-scale internal solitary waves

Multi-scale solitary waves have been derived by Benjamin (1992) [4] in a two-fluid system relying on the balance of capillary and gravitational dispersion and nonlinearity. Subsequently Derzho and Velarde (1995) [17] derived multi-scaled internal shallow water solitary waves for a continuously stratified fluid with a free surface. The amplitude equation for these waves has nonlinearities that are of greater power than in the common Korteweg-de Vries equation, similar to the generalized KdV equation. The generalized Korteweg-de Vries (GKdV) includes the KdV and modified KdV equation and a term of higher order nonlinearity. Benjamin (1972) [2] has proven the stability of Korteweg-de Vries (KdV) type waves, which was extended by Bona (1975) [6]. The stability of KdV type waves have been considered using the generalized KdV equation, which can be written as

$$A_x^2 = A^2(aA^p + b) = R(A) \tag{3.50}$$

where $p \leq 4$. The KdV wave is given by $p = 1$ and the mKDV wave by $p = 2$. Weinstein (1986) [68] has shown the stability and integrability for $p < 4$. For $p \geq 4$ no stability proof is available. Bona *et al* (1987) [7] assume that an amplitude equation of the generalized KdV type (3.50) is marginally stable for $p = 4$ and unstable for $p > 4$.

Derzho and Velarde (1995) [17] derive multi-scaled internal solitary waves for a polynomial term $R(A)$ on the right hand side of (3.50) of quintic power $q$ and additional polynomial terms of degree $q < 5$. The derivation is based on introducing multiple scales

for the horizontal length scale of the solitary waves, where a balance of nonlinearity and dispersion is maintained as is typical for Korteweg-de Vries type equations, but where the dispersive effects are reduced by increased horizontal length scales.

The structure of these multi-scaled waves resembles those of oscillatory bores (see [55]), with a solitary wave situated on top of a larger broader solitary wave.

The main concern of this part of the study is to show that such multi-scaled internal solitary waves exist and are stable for polynomials given by $R(A)$ of degree $q = 5$, see equation (3.50).

### Derzho-Velarde asymptotic solution

It is possible to derive multi-scale solitary waves by introducing a quartic term in the second order function of the density field $f(z)$,

$$f(z) = a_2 z^2 + a_3 z^3 + a_4 z^4, \tag{3.51}$$

$$\rho(z) = \rho_0(1 - \sigma z - \sigma^2 f(z)). \tag{3.52}$$

The differential equation for the amplitude is then given by

$$A_{xx} + \lambda^{(1)}A + 2\pi A^2 + M(A) = 0, \tag{3.53}$$

where $M(A)$ is

$$M(A) = 2\pi^2 \int_0^1 A\sin(\pi z)^2 f_\phi(z + A\sin(\pi z))dz \tag{3.54}$$

and equates to a fourth-order polynomial in terms of the amplitude $A$

$$M(A) = c_4 A^4 + c_3 A^3 + c_2 A^2 + c_1 A, \tag{3.55}$$

with the coefficients of the polynomial being given by

$$c_1 = a_2 \pi^2 - \frac{3}{2}a_3 + a_3\pi^2 - 3a_4 + a_4\pi^2, \tag{3.56}$$

$$c_2 = \frac{16}{3}a_2\pi - \frac{640}{9\pi}a_4 + 8a_3\pi + 16a_4\pi, \tag{3.57}$$

$$c_3 = \frac{9}{4}a_3\pi^2 + \frac{9}{2}a_4\pi^2, \tag{3.58}$$

$$c_4 = \frac{128}{15}\pi a_4. \tag{3.59}$$
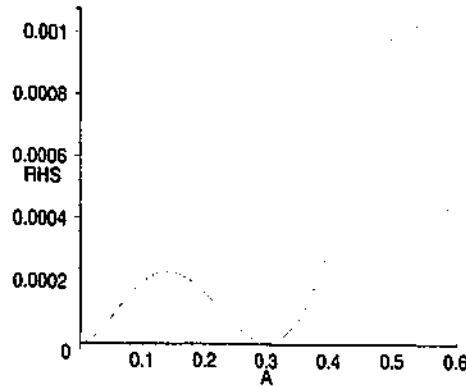
Figure 3.3: Plot of the right-hand-side of equation (3.62) for $\alpha_3 = 1.001$ and $A_0 = 0.6$.

Using the condition

$$A_x = 0 \qquad \text{for} \qquad A = A_0 \tag{3.60}$$

on equation (3.53) yields the eigenvalue $\lambda^{(1)}$

$$\lambda^{(1)} = -\frac{4}{3}\pi A_0 - \frac{2}{5}c_4 A_0^3 - \frac{1}{2}c_3 A_0^2 - \frac{2}{3}c_2 A_0 - c_1, \tag{3.61}$$

which is used to compute the phase speed of the wave.

After some algebra the ordinary differential equation for the amplitude is found to be

$$-\frac{A_x^2}{A^2} = (A - A_0)\left[\alpha_1 + \alpha_2(A + A_0) + \alpha_3(A^2 + A_0^2 + AA_0)\right], \tag{3.62}$$

where the coefficients $\alpha_1, \alpha_2, \alpha_3$ are given by

$$\alpha_1 = \frac{2}{3}c_2 + \frac{4}{3}\pi, \tag{3.63}$$

$$\alpha_2 = \frac{2}{4}c_3, \tag{3.64}$$

$$\alpha_3 = \frac{2}{5}c_4. \tag{3.65}$$

From this equation it is apparent that the solution is singular for $A = A_0$ and if the quadratic polynomial on the right hand side has a root. If that is the case, the amplitude equation reduces to the conventional KdV equation, which has no solution for $A > A_0$.

It is thus the aim to find parameters for which the quadratic polynomial has no root between $A = 0$ and $A = A_0$. Furthermore, in order to emphasize the multi-scale

| $\alpha_3$ | $a_2$ | $a_3$ | $a_4$ | $\lambda^{(1)}$ |
|---|---|---|---|---|
| 1.001 | -0.157722 | -0.240761 | 9.334810 | 2.923720 |
| 1.1 | -0.141238 | -0.261901 | 0.102580 | 2.874529 |

Table 3.1: Table of parameters for $A_0 = 0.3$

character of the solitary wave, it is necessary to choose the parameters in such a way that the local minimum is located very close to the horizontal axis. Picking the maximum amplitude $A_0$ there is one free parameter to choose the local minimum of the equation. This results in a linear system of three equations for the three variables $a_2$, $a_3$ and $a_4$, defining the density field. One example of the right-hand-side of equation (3.62) is shown in Figure 3.3.

For $\alpha_3$ taking the values 1.001, 1.1 and the maximum amplitude $A_0 = 0.3$ the corresponding parameters, together with the eigenvalues are given in Table 3.1. Equation (3.62) is then solved for the amplitude function using a Runge-Kutta method.

## 3.4 Large-amplitude inertial solitary waves with vortex cores in a cylindrical channel

The large-amplitude inertial solitary waves with vortex cores in a rotating flow are derived using the steady form of equations (2.16,2.17) and (2.18), introducing the streamfunction by

$$u - c = \frac{\psi_r}{r}, \qquad v = -\frac{\psi_x}{r}. \tag{3.66}$$

Equation (2.19) shows that the circulation is constant along a streamline, thus $C = C(\psi)$, where the functional form of $C(\psi)$ is to be determined from the upstream inflow condition for those streamlines which originate upstream. Inside the recirculation zone, which is located on the channel axis, DG show that the circulation is very weak, and in effect $C(\psi) \approx 0$ there. Finally, it can be shown that the vorticity equation (2.20) becomes

$$\psi_{xx} + \psi_{rr} - \frac{\psi_r}{r} + C(\psi)C'(\psi) = r^2 G(\psi), \tag{3.67}$$

where $G(\psi)$ is also to be determined from the inflow conditions for those streamlines which originate upstream. Inside the vortex core the flow is nearly stagnant, thus

$G(\psi) \approx 0$ there. Equation (3.67) is the Bragg-Hawthorne equation (1950) [9] used in numerous studies of rotating flows.

It is convenient to introduce dimensionless co-ordinates based on a typical axial velocity $U_0$ and the radius of the cylindrical channel $a$.

$$\psi' = \frac{2\psi}{U_0 a^2}, \qquad r' = \frac{r}{a}, \qquad x' = \frac{x}{a}. \tag{3.68}$$

Hereafter, the prime superscripts will be omitted. The inflow condition of axial velocity and rotation are close to uniform and given in dimensionless form by,

$$u \to u_\infty = 1 + \kappa U(\xi), \qquad \text{as} \qquad x \to -\infty, \tag{3.69}$$

$$\frac{w}{r} \to \frac{w_\infty}{r} = \Omega_0 \left( 1 + \sigma\Omega(\xi) \right), \qquad \text{as} \qquad x \to -\infty, \tag{3.70}$$

where $\xi = r^2$ and $U(\xi)$, $\Omega(\xi)$ are additional functions representing the departure from uniform axial flow and rotation which will be defined later. Here $\Omega_0$ is the swirl number, which is proportional to the ratio of the azimuthal velocity at the channel wall to the axial velocity and defines the strength of the rotation. Also, $\kappa$ and $\sigma$ are small parameters, characterizing the small departures from uniform axial flow and uniform rotation respectively. It follows that

$$\psi = \xi(1-c) + \kappa \int_0^\xi U(\hat{\xi})d\hat{\xi}, \qquad \text{as} \qquad x \to -\infty. \tag{3.71}$$

For those streamlines which originate upstream the functions $C(\psi)$ and $G(\psi)$ are

$$C(\psi) = \frac{\Omega_0}{1-c} \left\{ \psi + \sigma\psi\Omega(\frac{\psi}{1-c}) - \kappa \int^{\frac{\psi}{1-c}} U(\hat{\xi})d\hat{\xi} + \cdots \right\} \tag{3.72}$$

and

$$G(\psi) = \frac{2\Omega_0^2}{1-c} \left\{ 1 - \frac{\kappa}{1-c}U(\frac{\psi}{1-c}) + 2\sigma\Omega(\frac{\psi}{1-c}) + \frac{\sigma\psi}{1-c}\Omega'(\frac{\psi}{1-c}) \right\}$$
$$+ 2\kappa U'(\frac{\psi}{1-c}) + \cdots . \tag{3.73}$$

Here, the omitted terms are relatively of order of magnitude $O(\kappa, \sigma)$. Using the expressions (3.72, 3.73) equation (3.67) can be rewritten in explicit form in terms of the perturbed streamfunction $\phi$ where

$$\psi = \xi(1-c) + \kappa \int_0^\xi U(\hat{\xi})d\hat{\xi} + \phi. \tag{3.74}$$

Substituting equation (3.74) into equation (3.67) yields an equation for $\phi$

$$\phi_{xx} + 4\xi\phi_{\xi\xi} + \lambda^2\phi = F(\phi), \tag{3.75}$$

where

$$\lambda = \frac{2\Omega_0}{|1-c|} \tag{3.76}$$

and

$$
\begin{aligned}
F(\phi) = & \; \kappa\lambda^2 \left\{ \int_\xi^{\xi + \frac{\phi}{1-c}} U(\hat{\xi})d\hat{\xi} + \frac{\phi}{1-c}U\left(\xi + \frac{\phi}{1-c}\right) \right\} - \cdots \\
& \sigma\lambda^2 \left\{ 2\phi\Omega\left(\xi + \frac{\phi}{1-c}\right) + \phi\left(\xi + \frac{\phi}{1-c}\right)\Omega'\left(\xi + \frac{\phi}{1-c}\right) \right\} + \cdots \\
& 4\kappa\xi\left\{ U'\left(\xi + \frac{\phi}{1-c}\right) - U'(\xi) \right\} + \text{h.o.t.} \; .
\end{aligned} \tag{3.77}
$$

The boundary conditions on the channel axis and wall are

$$\phi = 0, \qquad \text{at} \qquad \xi = 0,1. \tag{3.78}$$

The boundary condition at $\xi = 0$ derives from the requirement that the flow be finite and regular there. Further, in the upstream and downstream directions it is required that

$$\phi \to 0, \qquad \text{as} \qquad x \to \pm\infty. \tag{3.79}$$

In the absence of any recirculating zone, equations (3.75, 3.78, 3.79) provide a complete formulation of the problem, since it is assumed that all streamlines originate upstream. The condition for no flow reversal is given by

$$1 + \frac{\phi_\xi}{1-c} > 0 \tag{3.80}$$

everywhere, then, to leading order with respect to the small parameter $\kappa$, $u - c > 0$ ($< 0$) according as $c < 1$ ($c > 1$) and there is no flow reversal at any point in the flow.

The critical condition, when condition (3.80) is violated on the channel axis is given by,

$$1 - c + \phi_\xi = 0, \qquad \text{at} \qquad \xi = 0, \tag{3.81}$$

which defines the critical wave amplitude $A_*$. For waves with amplitudes greater than the critical amplitude $A_*$, the wave exhibits a zone of recirculating fluid located on the

channel axis. Outside the recirculation zone, the flow is determined by equation (3.75) with the boundary conditions

$$\phi + \eta^2(1-c) + \kappa \int_0^{\eta^2} U(\hat{\xi})d\hat{\xi} = 0, \qquad \text{at} \qquad \xi = \eta^2, \tag{3.82}$$

where $\eta$ defines the boundary of the recirculation zone and

$$\phi = 0, \qquad \text{at} \qquad \xi = 1, \tag{3.83}$$

as well as the conditions (3.79) at infinity. Inside the recirculation zone the governing equation is (3.67), the circulation function $C(\psi)$ and the vorticity function $G(\psi)$ are yet to be determined. DG have shown that $G(\psi)$ is essentially zero.

### Derivation of the steady-solutions

In the derivation of the solitary wave solutions, it is assumed that the width of the waves is much greater than the radius of the cylindrical channel. Hence it is convenient to introduce the small parameter $\epsilon$ and let $X = \epsilon x$. An asymptotic expansion of $\phi$ and $c$ in terms of $\epsilon^2$ yields

$$\phi(X,\xi) \sim \sum_{k=0}^{\infty} \epsilon^{2k} \phi^{(k)}(X,\xi), \tag{3.84}$$

$$c \sim \sum_{k=0}^{\infty} \epsilon^{2k} c^{(k)}. \tag{3.85}$$

These expansions are substituted into (3.75) and the boundary conditions (3.78). At the lowest order,

$$\phi^{(0)} = A(X)W(\xi), \tag{3.86}$$

where

$$W(\xi) = rJ_1(\lambda^{(0)}r), \tag{3.87}$$

and

$$J_1(\lambda^{(0)}) = 0. \tag{3.88}$$

Here $J_1$ is the Bessel function of the first kind and

$$\lambda^{(0)} = \left| \frac{2\Omega_0}{1 - c^{(0)}} \right|. \tag{3.89}$$

Solving equation (3.88) for the first root yields $\lambda^{(0)} = 3.8317$ for the value of $\lambda^{(0)}$, which represents the lowest mode. The highest modes may be considered in analogy, but it is expected that higher modes do not exist in a purely steady form due to the generation of lower mode radiation.

The amplitude $A(X)$ is determined at the next order of the asymptotic expansion, which is

$$4\zeta \cdot \phi^{(1)}_{\xi\xi} + \lambda^{0^2}\phi^{(1)} = F^1, \tag{3.90}$$

where

$$F^1 = -A_{XX}W + \frac{F(\phi^{(0)})}{\epsilon^2} + \frac{2\lambda^{0^2}c^{(1)}}{c^{(0)}-1}AW. \tag{3.91}$$

This is to be solved with the boundary conditions

$$\phi^{(1)} = 0 \qquad \text{at} \qquad \xi = 0,1. \tag{3.92}$$

By exploiting the appropriate compatibility condition,

$$\int_0^1 F^1 W \frac{d\xi}{2\xi} = 0, \tag{3.93}$$

the following equation for A is obtained,

$$-A_{XX} + \Delta A + M(A) = 0. \tag{3.94}$$

Where

$$\Delta = \frac{2\lambda^{(0)^2}c^{(1)}}{c^{(0)}-1}, \tag{3.95}$$

$$M(A) = \hat{\kappa}M_\kappa(A) + \hat{\sigma}M_\sigma(A), \tag{3.96}$$

$$IM_\kappa = \lambda^{(0)^2}\int_0^1 \frac{Wd\xi}{2\xi}\left\{\int_\xi^{\xi+\frac{\phi^{(0)}}{1-c^{(0)}}} U(\hat{\xi})d\hat{\xi} + \frac{\phi^{(0)}}{1-c^{(0)}}U\left(\xi+\frac{\phi^{(0)}}{1-c^{(0)}}\right)\right\}$$
$$+ \int_0^1 2Wd\xi\left\{U'\left(\xi+\frac{\phi^{(0)}}{1-c^{(0)}}\right) - U'(\xi)\right\}, \tag{3.97}$$

$$IM_\sigma = -\lambda^{(0)^2}\int_0^1 \frac{Wd\xi}{2\xi}\left\{2\phi^{(0)}\Omega\left(\xi+\frac{\phi^{(0)}}{1-c^{(0)}}\right) + \phi^{(0)}\left(\xi+\frac{\phi^{(0)}}{1-c^{(0)}}\right)\Omega'\left(\xi+\frac{\phi^{(0)}}{1-c^{(0)}}\right)\right\},$$
$$\tag{3.98}$$

and

$$I = \int_0^1 \frac{W^2 d\xi}{2\xi} = \int_0^1 r J_0^2 (\lambda^{(0)})^2. \tag{3.99}$$

Equation (3.94) can be integrated once to yield an amplitude equation for $A$,

$$-A_X^2 + \Delta A^2 + 2\int_0^A M(A')dA' = 0. \tag{3.100}$$

## Solution to the Inner Region

The flow field is divided into three regions, an outer region where equations (3.94) and (3.67) hold combined with the amplitude equation (3.100), an inner region and a recirculation core, which are discussed next. Assuming the width of the inner solution large compared to the depth and the amplitude close to $A_*$, the solution in the inner region can be found by introducing a perturbed maximum amplitude

$$A(z) = A_* + \mu \operatorname{sign} A_* B(z) \qquad \text{with} \qquad 0 \leq B(z) \leq 1, \tag{3.101}$$

where the maximum possible amplitude is given by

$$A_* = \pm\frac{4|\Omega_0|}{\lambda(0)^2} = \pm 0.272, \tag{3.102}$$

differentiating between the two cases when $c^{(0)} > 1$ ($c^{(0)} < 1$), corresponding to $A_* > 0$ ($A_* < 0$), and $z = \beta x$ is another stretched variable, with $\beta = \frac{\epsilon}{\sqrt{\mu}}$ and $\mu$ a small parameter. Thus the width of the inner zone is smaller than the total length scale of the wave and tends to zero as $\mu \to 0$. In order to derive an approximative governing equation for the inner solution the depth of the vortex core $\eta$ is assumed small, $\eta = \delta f(z)$, where $\delta$ is another small parameter and $F(z)$ is a function describing the shape of the vortex boundary (i.e. the vortex core is given by $z = 1 - \eta$ for $|z| < z_0$, where $z_0$ is to be determined). It is shown by DG that an optimal balance of parameters occurs when $\delta = \epsilon^{1/2}$, $\mu = \epsilon$ and $\beta = \epsilon^{1/2}$. The amplitude equation describing the shape of the solution in the inner region is found by substituting equation (3.101) into the first-order equation (3.75), satisfying the kinematic and dynamic boundary conditions. Using a compatibility condition similar to (3.93) yields an approximative governing equation in terms of $B(z)$,

$$B_z^2 = R(A_*)(1 - B) - \frac{2\nu}{3}(1 - B^3) \tag{3.103}$$

where

$$R(A) = \text{sign} A_* \left\{ \frac{4}{A} \int_0^A M(A') dA' - 2M(A) \right\} \quad \text{and} \quad \nu = \frac{1}{I|A_*|} \frac{\mu^2}{\epsilon^2}. \quad (3.104)$$

Inside the recirculation zone the key assumption is that the flow is stagnant to leading order. For a nontrivial solution to exist the right-hand side of equation (3.103) must be positive, yielding a bound on $\nu$ and $\mu$, which in turn places an upper bound on the maximum possible amplitude,

$$\nu < \nu_{max} = \frac{1}{2} R(A_*), \qquad \mu < \mu_{max} = \epsilon \sqrt{I|A_*|\nu} \quad (3.105)$$

$$A_{max} = A_* + \mu_{max} . \quad (3.106)$$

Assume a basic velocity and swirl field as a quadratic in terms of the radial variable $\xi = r^2$ given by

$$U(\xi) = a_1(1 - \xi) + a_2(1 - \xi^2) \quad (3.107)$$

$$\Omega(\xi) = b_1(1 - \xi) + b_2(1 - \xi^2), \quad (3.108)$$

then M(A), equation (3.96), is given by

$$\frac{I}{\lambda^{(0)2}} M(A) = \alpha_1 A + \alpha_2 A^2 + \alpha_3 A^3. \quad (3.109)$$

The equations for $\alpha_1$, $\alpha_2$ and $\alpha_3$ in terms of $a_1$, $a_2$, $b_1$ and $b_2$ are given in the Appendix. From equations (3.72,3.74), for the above flow functions, $\psi$ and $C(\psi)$ can be computed. Equation (3.104) for $R(A)$ evaluates to

$$R(A) = \text{sign} A_* \left( -\frac{2}{3} \alpha_2 A^2 - \alpha_3 A^3 \right). \quad (3.110)$$

Subsuming the factor before $M(A)$ in equation (3.109) in the $\alpha$'s, equation (3.100) becomes

$$-A_X^2 + \tau^2 A^2 + \hat{\alpha_2} A^3 + \hat{\alpha_3} A^4 = 0, \quad (3.111)$$

where $\tau^2 = \Delta + \hat{\alpha_1}$, $\alpha_1 = \frac{\lambda^{(0)2}}{I} \alpha_1$, $\hat{\alpha_2} = \frac{2\lambda^{(0)2}}{3I} \alpha_2$ and $\hat{\alpha_3} = \frac{2\lambda^{(0)2}}{4I} \alpha_3$. Two different outer solutions are considered in the following. The first is an outer solution governed by a Korteweg-de Vries (KdV) equation. The second is governed by a modified KdV equation.

1. For $\hat{\alpha}_3 = 0$ equation (3.111) simplifies to the well known KdV equation, which has the familiar solution

$$A(X) = -\frac{\tau^2}{\alpha_2}\text{sech}^2(-\frac{\tau}{2}(|X| - X_*)).$$  (3.112)

2. The second case $\hat{\alpha}_3 \neq 0$ yields the modified KdV solution given by

$$A(X) = \frac{A_0}{1 + B_0\cosh(\tau(|X| - X_*))},$$  (3.113)

where

$$A_0 = -\frac{2\tau^2}{\hat{\alpha}_2} \quad \text{and} \quad B_0^2 = 1 - 4\frac{\hat{\alpha}_3}{\hat{\alpha}_2}\tau^2.$$  (3.114)

The maximum $\mu$ is given by

$$\mu_{max} = -\frac{\epsilon^2}{2}I\left(-\frac{\alpha_2}{3}|A_*|^2 A_* - \frac{\alpha_3}{2}|A_*|^3 A_*\right).$$  (3.115)

To find the solution of the inner region an asymptotic solution for $B \to 1$ of equation (3.103) is found first and an adaptive step size Runge-Kutta method is then used to solve for $B(z)$. The approximation for $B \to 1$ is given by

$$B(z) = 1 - \hat{c}z^2,$$  (3.116)

where

$$\hat{c} = \frac{1}{2}\left(\frac{1}{2}R(A_*) - \nu\right).$$

# Chapter 4

# Numerical Method

There are a number of methods to solve elliptic partial differential equations such as the ones which appear in the study of fluids. Depending on the choice of primitive variables one uses to describe a fluid in motion, there are generally three separate types of tasks that can be treated independently of one another and that represent the whole numerical scheme for solving the partial differential equations.

When solving the time-dependent equations the first task is to integrate the equations in time. Commonly known methods are explicit methods like the Runge-Kutta method and related schemes as well as implicit methods such as the Crank-Nicholson scheme. Generally implicit schemes are more stable than explicit schemes in the absolute sense, but are computationally more expensive, since the associated matrix inversion is complicated and not always straightforward. The stability condition for explicit schemes restricts the size of the time-steps, but the computational effort involved is very small and is the main advantage of explicit schemes.

Of the explicit schemes the Runge-Kutta schemes are the most robust. The Runge-Kutta method approximates the differential by a Taylor series of a certain order, which defines the order of accuracy of the method. The time-integration method used here belongs to the family of low-storage Runge-Kutta methods and reduces the computational load while retaining a measurable order of accuracy. At various places in the literature low-storage schemes have been introduced, see Williamson (1980) [72], Canuto *et al* (1988) [12] and Stetter (1973) [61], which combine a reasonable level of accuracy with a computationally efficient scheme and advantageous stability domains. The low-storage

Runge-Kutta method used in this study is proposed by Williamson (1980) [72] and originally stated in Stetter (1973) [61]. It is third order and possesses a stability region identical to a fourth-order Runge-Kutta method.

The second task for solving the partial differential equations is the spatial integration. Two methods are predominantly used: Finite difference methods and finite element methods. Finite difference methods approximate spatial differentials by a Taylor series of finite order and are easily implemented, when problems are very complex and need a fast solution, trading off accuracy.

Finite element methods approximate the solution to the differential equation by a linear series of basis functions appropriate to the boundary conditions, approximating the functions locally as is the case in the general finite element method or globally which is the case in the spectral methods used in this study, see Hirsch (1988) [35].

The general finite element method is very accurate but requires an integral formulation of the physical problem which is not always at hand. Related to finite element methods are the finite-volume methods that also require an integral representation making use of Gauss's flux theorems on a finite volume and applying the finite element methods to solve the differential equation. As mentioned the integral representation may be too difficult to acquire and generally not always possible.

The so-called pseudospectral method approximates the solution globally, not locally, as is the case in the finite element/volume methods, and its error decreases exponentially with the number of functions used. The exponential error decrease is the most important advantage of spectral methods, and distinguishes them from conventional methods in terms of accuracy. In practice, the exceptional accuracy of spectral methods is used to the advantage of computational efficiency, making a coarser grid spacing possible.

Spectral methods approximate the solution using a finite sum of very smooth basis functions, either for example trigonometric functions or Chebyshev polynomials - which are just trigonometric functions in disguise, see Boyd (1989) [8]. Chebyshev and Fourier functions are widely used in situations where a reasonably simple geometry is given that suggests the use of a function space related to that geometry - usually a rectangle or

circle - and the function to be solved for is smooth and lies in the corresponding function space. The limited applicability of spectral methods with respect to geometry and boundary conditions shall not be overlooked here, but albeit these restrictions advances have been made incorporating shock fronts and splitting areas, incorporating two sets of function spaces, see Fornberg (1996) [21]. It is therefore fair to say that if spectral methods can be used, they usually excel with all respects over conventional methods.

In some cases it is possible to use spectral methods in non-trivial geometries too. If, as is the case in this study, the rectangular domain is modified by a change of depth over a segment of the horizontal extension it is possible to transform the spatial derivatives to cartesian derivatives. This is done for the stratified flow over topography.

If the domain cannot be transformed into an appropriate geometric domain by using a transformation to cartesian coordinates or other relevant coordinate system transformations such as cylindrical and spherical domains, then multigrid methods can be used. Multigrid methods belong to the family of finite difference methods but increase the computational effort drastically, necessitating a trade off in accuracy, which then makes standard finite difference schemes more affordable.

Spectral methods have special advantages when modelling waves in particular, since dissipative and dispersive errors are very small, Fornberg (1996) [21]. This is fundamentally important when studying nonlinear waves, where even a slight increase in dispersion – induced by the scheme – can change the whole balance between nonlinearity and dispersion necessary for solitary wave existence.

In the cases studied here, pseudospectral Fourier collocation is used to represent the function in the horizontal with a periodic domain. In the vertical Chebyshev collocation is used, because Chebyshev functions can account for the non-periodic boundary conditions in the vertical.

A 2/3 filter on the highest modes is used to remove aliasing errors and a sponge is situated across the periodic boundary condition in the horizontal to prevent energy propagated downstream from re-entering the domain.

Since solitary waves conserve momentum and energy, it is of vital importance for the

numerical scheme to be non-dissipative, more precisely that the nonlinear convective term in the governing equation is represented in conservative form, see Zang (1990) [74], Fox and Orszag (1973) [22] and Gottlieb and Orszag (1989) [26]. The nonlinear convective term becomes, after taking the curl of the momentum equations,

$$\nabla \times (\vec{u} \times \vec{\omega}),$$

where the vorticity vector $\vec{\omega}$ is given by $\vec{\omega} = \nabla \times \vec{u}$, which has only one component in the y-direction $\vec{\omega} = \omega \vec{j}$. The computation of the nonlinear convective term in energy conserving form is given by $\nabla \cdot (\vec{u}\,\vec{\omega})$. The energy conserving form of the convective term has been successfully employed by Rottman et al (1996) [58] to study the unsteady flow of an incompressible, inviscid Boussinesq flow over topography.

The third problem usually encountered involves solving a discrete second-order elliptic linear partial differential equation, for example the Poisson equation or a form of the generalized Poisson equation. One can use iterative finite difference methods or direct methods, as will be explained in more detail in the following. For a numerical analysis of spectral methods see Gottlieb and Orszag (1989) [26] and Gottlieb et al (1984) [25]. For another detailed study of pseudospectral methods see He (1997) [34], the fundamental works of Boyd (1989) [8] for Chebyshev-Fourier methods in particular, Canuto et al (1988) [12] for spectral methods in general and the recent publication by Fornberg (1996) [21].

## 4.1 Solving equations of the type $L\psi = f$

For the governing equations occurring in this study two types of implicit matrix equations have to be solved. The stratified flow with and without topography poses a discrete elliptic problem, which is solved using the solution to a Poisson equation and a Liouville-Neumann iteration to a fix-point problem. In addition to solving a Poisson equation for the stratified flow with a Laplace operator, it is similarly necessary to solve a generalized Poisson equation, which occurs in the axisymmetric rotating flow through a cylindrical channel. The generalized Poisson equation is solved using minimum residual methods

combined with direct methods as outlined by Canuto *et al* [12]. The following discusses the two methods in more detail.

## Solving the equation $\nabla \cdot \rho \nabla \psi = f$

For the stratified flow using a Runge-Kutta method in time amounts to solving the discrete elliptic problem in space at each iteration,

$$\nabla \cdot \left[ \rho(x,z) \quad \nabla \psi(x,z) \right] = f(x,z). \tag{4.1}$$

In the Boussinesq approximation the density $\rho(x,z)$ on the left-hand-side of equation (4.1) is replaced by $\rho_0$. Equation (4.1) then reduces to the Poisson equation.

In this special case the Laplace operator on the left-hand side of equation (4.1) is positive-definite and relaxation schemes succeed. The relaxation method was successfully employed in the pseudospectral code of Rottman *et al* (1996) [58] and Aigner *et al* (1999) [1]. In the case where $\rho(x,z)$ is variable the operator on the left-hand side becomes

$$\rho(x,z)\nabla^2 + \nabla \rho(x,z) \cdot \nabla. \tag{4.2}$$

For an equidistant discretisation, analogous problems have successfully been solved using multigrid methods and appropriate preconditioners for the case of periodicity in two and three spatial dimensions, see [10, 64, 36].

The present pseudospectral model features an unequally spaced discretisation in conjunction with a transformation of the original differential operator to a topography-following differential operator. Furthermore, the model has mixed periodic-nonperiodic boundary conditions. A multigrid technique due to Wesseling (1982) [70, 71] and McCarthy (1983) [53] was applied initially, but failed due to the operator not being sufficiently diagonally dominant. As mentioned above in addition the multigrid technique requires a lot more computational effort to solve the elliptic problem (4.1). Considering the aim of examining the long-time behaviour of solitary waves this is extremely undesirable. For these reasons the multigrid technique was discarded in favor of a different iterative scheme, which splits up the elliptic problem (4.1) into the easily solvable discrete elliptic problem of the Poisson equation and a fixed-point problem.

Here, a method is proposed that employs a relaxation scheme for the spatial integration and a Runge-Kutta scheme combined with a Liouville-Neumann iteration to integrate forwards in time. For this purpose consider that equation (2.5) can be regarded as a fixed-point problem

$$\Delta \Phi = -J(\psi, \Delta \psi) - \frac{\rho_x}{\rho} \left\{ g + \Phi_x + J(\psi, \psi_x) \right\} - \frac{\rho_z}{\rho} \left\{ \Phi_z + J(\psi, \psi_z) \right\}, \qquad (4.3)$$

where $\Phi$ is the local temporal derivative of the streamfunction

$$\Phi = \frac{\partial \psi}{\partial t}. \qquad (4.4)$$

The left-hand side of equation (4.3) is inverted at each time step, applying the same relaxation scheme used by Rottman *et al* (1996) [58] and a low-storage Runge-Kutta scheme to solve

$$\Delta \frac{\partial \psi}{\partial t}(x, z, t) = F(x, z, t, t^*) \qquad (4.5)$$

for $\psi(x, z, t)$, where $t^*$ is an intermediate time used in the iterative approximation of the local time derivatives, $\Phi_x$ and $\Phi_z$ on the right-hand side of equation (4.3). The time-differences on the right-hand side of (4.3) are approximated by a first-order two-point stencil

$$\Phi^N = \frac{\psi^N - \psi^0}{\Delta t}, \qquad (4.6)$$

where $\psi^N$ is the approximated streamfunction and $\psi^0$ is the starting value for the iterated streamfunction $\psi$. The problem (4.3) can then be solved by iterating

$$L\Phi^{N+1} = F\Phi^N, \qquad (4.7)$$

where $L$ is the Laplace operator and $F$ is the differential operator on the right hand side of equation (4.3). If $\psi^N$ lies in the solution space $S$ which is complete, and the operator $F$ on the right-hand side is Lipschitz-bounded in $S$, then a converging Cauchy-series exists for all $N$ (see Collatz (1960) [13] and [40, 69] and references cited therein).

The low-storage Runge-Kutta method used is the memory efficient third-order scheme based on the method by Williamson (1980) [72] and Stetter (1973) [61]. The temporal approximation in the Liouville-Neumann iteration is first order. The accuracy of the

temporal approximation could be improved by using higher order finite difference approximations for $\Phi_x$ and $\Phi_z$, which would obviously increase the computational effort, since more than two approximated streamfunction fields $\psi^N$ have to be stored. Because the computational expense is already high, employing the Liouville-Neumann iteration, the use of higher-order approximations for $\Phi_x$ and $\Phi_z$ is omitted here.

## Solving the equation $\psi_{xx} + \psi_{rr} - \frac{1}{r}\psi_r = f$

For the rotating flow through a cylindrical channel the main difficulty lies in solving the discrete second-order elliptic partial differential equation

$$L\psi = f, \tag{4.8}$$

where the operator $L$ is given by

$$L = \partial_{xx} + \partial_{rr} - \frac{1}{r}\partial_r. \tag{4.9}$$

In the previous problem, the operator $L$ was the conventional Laplace operator, whereas here a different operator $L$ is given similar to the operator of a generalized Poisson equation.

For solving equation (4.9) various methods were adopted in the course of this study. At first a multigrid method from Wesseling (1982) [70] and McCarthy (1983) [53] was employed, but this method is computationally extremely expensive and too slow. An alternative method is to solve equation (4.9) in spectral space using the minimum residual method (MRM) due to Richardson. The MRM uses a preconditioner $H$ as an approximation to $L$, which is easily invertible. For a time-independent operator $L$, the preconditioner $H$ can be computed before starting the actual computation, thus greatly reducing the cost. Note that $L$ is the operator in spectral space and $H$ is the operator in an approximated space, which is typically second order accurate. The accuracy of this approximation depends on the discretization used and can vary greatly. Typically, a second order finite difference preconditioner is used, alternately it is much more accurate to use direct methods if available, see Canuto *et al* (1988) [12].

The minimum residual method used here is as follows

$$LP^n = f - L\psi^n = R^n,$$

where

$$P^n = \psi^{n+1} - \psi^n$$

or

$$P^n = L^{-1}R^n$$

or in this case

$$P^n = H^{-1}R^n.$$

The accelerator is given by optimizing according to the Rayleigh norm

$$\varsigma = \frac{(R^n, LP^n)}{(LP^n, LP^n)}$$

and

$$\psi^{n+1} = \psi^n + \varsigma P^n,$$

$$R^{n+1} = R^n - \varsigma LP^n.$$

Thus the only difficulty remaining is finding the preconditioning matrix $H^{-1}$, desirably close (or identical) to the spectrally accurate operator $L^{-1}$. Assuming that $H^{-1}$ was exactly $L^{-1}$, the solution would be obtained immediately in one step of the iteration, the operator being the exact inverse of $L$. But as is the case here, the computational effort of inverting $L$ is high, thus an approximate inverse $H^{-1}$ is used.

Theoretically, the eigenvalues of $H^{-1}$ lie very close to $L^{-1}$, thus the preconditioned minimum residual method has very desirable properties and fast convergence (positive-definiteness and so forth). Another way to think of it is that the second order approximation to $L^{-1}$ is made spectrally accurate by the minimum residual method.

## 4.2 Finite difference preconditioner

In the following two kinds of preconditioners commonly used are briefly described. Although finally direct methods are used for preconditioning, both of them will be

discussed, since the finite difference preconditioning provides illuminating insight into the robustness of the direct method.

The preconditioner $H$ is the finite difference representation of the two-dimensional elliptic partial differential equation given by (4.9) for the rotating flow problem. The preconditioner for the stratified flow problem is the Laplace operator and the derivation of the preconditioner is closely analogous to the operator in cylindrical coordinates and is therefore omitted here.

The finite difference preconditioning technique consists of the strongly implicit procedure to calculate the solution to the system of simultaneous algebraic equations of the five-point molecule form on the two-dimensional rectangular mesh, see Stone (1968) [62] and Jacobs (1972) [37]. The finite difference operator (4.9) can be written as

$$\partial_{xx} + r \left(\frac{1}{r}\partial_r\right)_r.$$

The partial x- and y-derivatives are discretized using second order accurate formulae

$$\psi_{xx} = \frac{\psi_{i+1,j} - 2\psi_{i,j} + \psi_{i-1,j}}{\Delta x^2} + O(\Delta x^2)$$

and

$$\frac{\partial}{\partial r}\left(c(r)\frac{\partial}{\partial r}\right)\psi = \frac{c_{i,j+\frac{1}{2}}c_{i,j+\frac{1}{2}}(\psi_{i,j+1} - \psi_{i,j})}{\Delta r^2} - \frac{c_{i,j-\frac{1}{2}}(\psi_{i,j} - \psi_{i,j-1})}{\Delta r^2} + O(\Delta r^2),$$

where

$$c_{i,j+\frac{1}{2}} = \frac{1}{2}(c_{i,j+1} + c_{i,j})$$

and

$$c_{i,j-\frac{1}{2}} = \frac{1}{2}(c_{i,j} + c_{i,j-1})$$

are the averages between $j, j+1$ and $j-1, j$, see Hirsch (1988) [35]. The complete operator is thus discretized by the 5—point stencil (see Figure 4.1) given by

$$\psi_{i+1,j} - 2\psi_{i,j} + \psi_{i-1,j} + \frac{1}{c_{i,j}}m(c_{i,j+1} + c_{i,j})(\psi_{i,j+1} - \psi_{i,j}) - \frac{1}{c_{i,j}}m(c_{i,j} + c_{i,j-1})(\psi_{i,j} - \psi_{i,j-1})$$

$$(4.10)$$

where

$$c_{i,j} = \frac{1}{r_j} \qquad \text{and} \qquad m = \frac{\Delta x^2}{2\Delta r^2}.$$
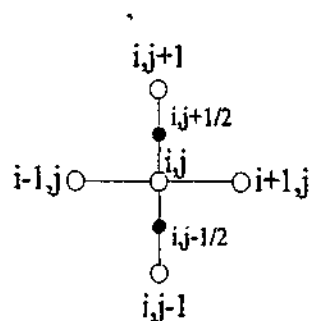
Figure 4.1: Stencil of the FD approximation. The empty dots represent the five-points of the stencil for the approximation of the second-order differential operator, the filled dots represent the averaged values of the function $c = \frac{1}{r}$ used in the second-order approximation.

Establishing the finite difference matrix for (4.10) yields a diagonally dominant matrix which is easily inverted. The maximum eigenvalue of this finite difference approximation to the operator (4.9) is very close to the eigenvalue of the Laplace operator in cartesian coordinates, the same is true for the spectral radius. Thus the operator (4.9) has the same qualitative properties as the Laplace operator in cartesian coordinates, which is vital for the following direct methods, ensuring positive-definiteness of the operator and convergence.

## 4.3  Direct methods

The most important advantage of direct methods is that they are more accurate than finite difference preconditioners. They make use of the properties of the approximating functions, in this case the globally approximating Fourier and Chebyshev functions, and provide a solution to a single implicit discrete differential matrix equation. In addition, direct methods are very attractive solution methods, because the operation count involved is competitively low and comparable to the usual spectral differentiation [12].

In the following the direct method used to solve equation (4.8) for $\psi$ is described briefly, for further details confer Canuto *et al* [12]. Consider

$$\frac{d^2\psi}{dx^2} + \frac{d^2\psi}{dr^2} - \frac{1}{r}\frac{d\psi}{dr} = f. \tag{4.11}$$

The Chebyshev collocation derivative can be represented in matrix form as

$$(\mathcal{D}_N \psi)(x_l) = \sum_{j=0}^{N} (D_N)_{lj} \psi(x_j), \tag{4.12}$$

where $(D_N)_{lj}$ is the operator matrix for $l, j = 0, ..., N$. The differential operator for equation (4.11) can be expressed as for the case of the Laplace operator, if in the Chebyshev collocation derivative, equation (4.12), for $D_N$ the following is substituted:

$$D_N = \mathcal{D}_N^\Delta - \frac{1}{r_l} \mathcal{D}_N,$$

where $\mathcal{D}_N^\Delta = \mathcal{D}_N^2$ is the second Chebyshev collocation derivative in cartesian coordinates. The matrix resulting from the above system can be transformed to Chebyshev space and by computing the eigenvalues of the differential operator in the r-direction, equation (4.11) reduces to

$$\frac{d^2 \hat{\psi}}{dx^2} + \lambda \hat{\psi} = \hat{f},$$

where $\lambda$ denotes the diagonal matrix with all the eigenvalues in Chebyshev space. Transformation in Fourier space gives

$$-k^2 \tilde{\hat{\psi}}_k + \lambda \tilde{\hat{\psi}}_k = \tilde{\hat{f}}_k, \tag{4.13}$$

with the conventional wave number $k$. The solution to the implicit equation (4.13) is trivially

$$\tilde{\hat{\psi}}_k = -\frac{\tilde{\hat{f}}_k}{(\lambda - k^2)}. \tag{4.14}$$

The direct method is the fastest of all preconditioning methods considered and greatly improves the speed of the minimum residual method used for solving the partial differential equation (4.11).

Equation (4.11) has an algebraic singularity at the axis, which is removed since $\psi = 0$ at the axis, but causes numerical conflicts. In order to remove this numerical singularity, the boundary is moved from the axis at $r = 0$ to a small quantity $\epsilon$ at $r = \epsilon$, with the boundary condition $\psi = 0$ there. The closed domain $[0, 1]$ is substituted by a semi-closed interval $(0, 1]$. The numerical results show that the solution is not sensitive to $\epsilon$ for small $\epsilon$. The parameter $\epsilon$ was initially chosen to be 0.1 and was varied down

to 0.01. As a consequence of the removable singularity, the time-step has to be rather small ($dt = 0.001$) for the numerical scheme to be stable. This limits the length of the total integration in time, a reasonable length being $t = 30$ secs in physical time ($t_r \approx 6$).

## 4.4    Testing the validity of the code

To establish the consistency and validity of the numerical model the results for exact solutions were studied. The following is a collection of methods for verifying the numerical model. All these tests show that the solutions are presented to within the error of the numerical code and that the scheme is not dissipative.

*A solution to the linearized equations*

The fully nonlinear governing equations for stratified flow given by Grimshaw and Yi (1991) [32] are the vorticity equation

$$\frac{d}{dt}(\nabla^2\psi) - N^2(z-\zeta)\left\{\zeta_x - \beta\left[\zeta_x\frac{d}{dt}(\psi_x) - (1-\zeta_z)\frac{d}{dt}(\psi_z)\right]\right\} = 0 \qquad (4.15)$$

and the equation for the deflection of the density surfaces

$$\frac{d\zeta}{dt} + \psi_x = 0, \qquad (4.16)$$

where

$$\frac{df}{dt} = \frac{\partial f}{\partial t} + J(f, \psi)$$

and $J(f, \psi) = f_x\psi_z - f_z\psi_x$. Density is given by $\rho(x, z, t) = \rho_0(z - \zeta)$ and the Boussinesq parameter $\beta$ by $\beta = \frac{N_0^2 D}{g}$.

This formulation has the advantage that only $N^2(z)$ is specified and obtained from the basic density profile

$$\rho = \rho_0(z), \qquad N^2 = -\frac{\rho_{0z}}{\beta\rho_0} \qquad (4.17)$$

and also that the '$\beta$' terms are not singular in this formulation. Now suppose $N^2 = const$ then

$$\rho_0(z) = \rho_{00}\, e^{-\beta N^2 z}. \qquad (4.18)$$

Linearization of equation (4.15) yields

$$(\nabla^2 \psi)_t - N^2 \zeta_x - N^2 \beta (\psi_z)_t = 0, \tag{4.19}$$

$$\zeta_t + \psi_x = 0. \tag{4.20}$$

A solution is given by

$$\zeta = e^{+\frac{1}{2}\beta N^2 z} e^{i(kx+mz-\hat{\omega}t)} + c.c., \tag{4.21}$$

$$\psi = \frac{\hat{\omega}}{k}\zeta, \tag{4.22}$$

with

$$\hat{\omega}^2 = \frac{k^2 N^2}{k^2 + m^2 + \frac{1}{4}\beta N^4}. \tag{4.23}$$

From equation (4.21) it follows that a small amplitude sinusoidal disturbance initialized at $z=0$ should increase as $e^{+\frac{1}{2}\beta N^2 z}$ as $z$ increases. A typical initial condition is

$$\zeta = e^{+\frac{1}{2}\beta N^2 z} \cos(kx + mz) e^{-30\,(z-\frac{1}{2})^2}, \tag{4.24}$$

where the solution (4.21) has been multiplied by a Gaussian to satisfy the no-flow boundary condition through the bottom boundary. The parameters $m$ and $k$ are suitably chosen, $m = \frac{2\pi}{w}$, $k = \frac{\pi}{2}$ and for $m \neq 0$ the wave is propagating at an angle

$$\arctan \frac{k}{m}$$

to the horizontal so that the change in amplitude is proportional to

$$\frac{\psi(x,z,t+dt)}{\psi(x,z,t)} \propto \frac{1}{\sqrt{\frac{\rho_0 - r}{\rho_0}}}. \tag{4.25}$$

The numerical model has been initialized with the solution given by equation (4.24) and found to satisfy the predicted growth rate to within the error of the computation.

*Conservation laws*

A more powerful method to verify the numerical model is to test the preservation of the conservation laws characteristic for solitary waves and the KdV solution in particular. The first two conservation laws are given by

$$\int_{-\infty}^{\infty} A \, dx = const$$

and

$$\int_{-\infty}^{\infty} A^2 \, dx = const,$$

where $A$ is a solution of the KdV equation, or in this case the amplitude of the disturbance. For further details confer Johnson (1997) [38] and Drazin (1983) [18].

The nonlinear non-Boussinesq terms neglected in the Boussinesq approximation for stratified flow can be tested using a traditional KdV solution with a linear density profile. In the Boussinesq approximation a solitary wave solution cannot exist, thus it is maintained solely by the non-Boussinesq terms. If the solitary wave is permanent of shape and stationary in the frame of reference, the nonlinear terms introduced work correctly up to the order of accuracy.

*Kinetic and potential energy*

Another method for verifying the numerical model is to calculate the change in kinetic energy

$$\Delta K = \int \int \frac{1}{2} \rho (u^2 + w^2) \, dx dz \qquad (4.26)$$

and the change in potential energy

$$\Delta P = \int \int g \rho z \, dx dz - \int \int g \rho z \, dx dz \Big|_{t=0}. \qquad (4.27)$$

The scheme is conserving energy if the change in total energy

$$\Delta E = \Delta K + \Delta P = const \qquad (4.28)$$

is constant to within the error of the computation. Gaussian quadrature is used to compute the two dimensional integrals and found to be conserved to within the error of the numerical model.

# Chapter 5

# Numerical Results

This section presents the results for the four applications considered. Firstly the results for the large-amplitude internal solitary waves with vortex cores in the Boussinesq approximation followed by the non-Boussinesq case. Then the results for the stratified flow over topography and multi-scaled internal solitary waves. In the fourth subsection, the results for the large-amplitude inertial solitary waves with vortex cores in a rotating flow are presented.

## 5.1 Large-amplitude internal solitary waves with vortex cores

Time is normalized with twice the halfwidth $\hat{L} = 2\,(x_0 + \bar{x})$ and the phase speed $U = c$, $t_n = t\,U/\hat{L}$. A measure of the width of the outer region being $\bar{x} = 2/\epsilon\kappa$ for case (1) and $\bar{x} = 1/\epsilon\kappa$ for case (2), these being the KdV and mKdV cases in the outer region respectively, while $x_0$ represents the halfwidth of the inner region where equation (3.19) is valid. The stratification parameter $\sigma$ is set to $\sigma = 0.01$ in the following to satisfy the Boussinesq approximation.

For the initialization of the streamfunction field in the inner region the first term of an expansion in powers of $\xi^2$ is used to approximate the bounded solution to equation (3.19) near $B = 1$,

$$B = 1 - \hat{k}\,\xi^2, \qquad \text{where} \qquad \hat{k} = \frac{1}{4}R(A_*) - \frac{1}{3}\nu. \tag{5.1}$$

Notice that the bound on $\nu$ (3.22) appears as the coefficient of the first term in this

expansion. A standard fourth-order Runge-Kutta solver continues the solution to $B = 0$, determining the width of the inner region. Initially the streamfunction is set to a constant, $\phi = \phi(z = D)$, inside the recirculation region. The initial density field is calculated taking advantage of equations (3.2,3.4) together with equation (3.9).

## Results for the equations in the Boussinesq approximation

The numerical results for both the KdV and mKdV outer solutions show that the approximate initial conditions shed transients (Figures 5.4, 5.5 and 5.8, 5.9), which propagate downstream only. Permanent steady solitary waves evolve after the flow has traversed the width of the waves for more than a hundred times, indicating the steady state of the solutions. In the close-up contours of the recirculation regions the streamfunction fields remain homogeneous (Figures 5.6 and 5.10), whereas the density field shows density inversions of higher order (i.e. variability of $O(10^{-6})$), but remains homogeneous to first order as predicted by DG. As a measure of the strength of the closed streamline region the maximum horizontal velocity opposing the downstream flow is measured at the top of the recirculation region. This adverse velocity opposing the flow at the upper boundary is of second order (Figures 5.7 and 5.11). The adverse velocity of the solution with the KdV outer solution decays to a level which cannot be resolved numerically. In contrast, the adverse velocity of the solution with the mKdV outer solution approaches a positive value. The results show that the recirculation region is stagnant to first order, as predicted by the asymptotic analysis of Derzho and Grimshaw (1997) [16] .

The amplitude of the steady state solution is measured for a number of different phase speeds from $0.65\mu_{max}$ to $0.95\mu_{max}$, denoted by diamonds in Figures 5.1 and 5.2. The results agree with the theoretical results for the amplitude-phase speed relations to within the error of the computation.

## Results for the non-Boussinesq case

Next, the results for the fully nonlinear governing equations in the non-Boussinesq case are presented. The maximum non-dimensional time the solutions were computed for is

$t_n \approx 11$, which corresponds to a dimensional time of more than $8.3\bar{3}$ hours. It is argued that the waves can be considered to be of permanent form if their shape is preserved for more than 6 hours of physical time. This is the case for non-dimensional times exceeding $t_n \approx 8$.

Figure 5.13 shows the evolution of the streamfunction at 2/3 of the depth $D$ for $\mu = 0.99\mu_{max}$ for the case of a KdV outer solution, at the normalized time $t_n = t\,U/\hat{L}$, where $\hat{L}$ is the length scale of the solitary wave as described above. Figure 5.14 is a sequence of five contour plots of the streamfunction and density at the respective times. Figures 5.16 and 5.17 display the results for the case of an mKdV outer solution for the same parameters as in the previous case. Noticeable from the contour plots are the transients propagating downstream and the essentially stagnant vortex core remaining intact. Figures 5.15 and 5.18 show the evolution of the maximum adverse velocity at the top boundary. Both show a non-vanishing velocity component in the upstream direction, but indicate that the length of computation may be insufficient.

A series of results from seven measurements, for $0.7 < \frac{\mu}{\mu_{max}} < 0.99$, shows a correction to the phase speed with an order of magnitude $O(10^{-4})$, see Figure 5.19. The relative error maximum $\frac{\Delta c}{c}$ is $0.1-0.4\%$. Note that the theoretical phase speed is known only to the order of magnitude $O(10^{-4})$, i.e. $O(\sigma^2)$ where here $\sigma = 0.01$ (compare with Figure 5.12). Hence the results suggest that the correction is to within the error of the theoretical solution and numerical scheme.

Comparing the results to the phase speed corrections in the case of the Boussinesq approximation, it is noticeable that the error of this numerical model is much larger than the Boussinesq spectral model, but still small enough to prove a satisfactory consistency with the above model.
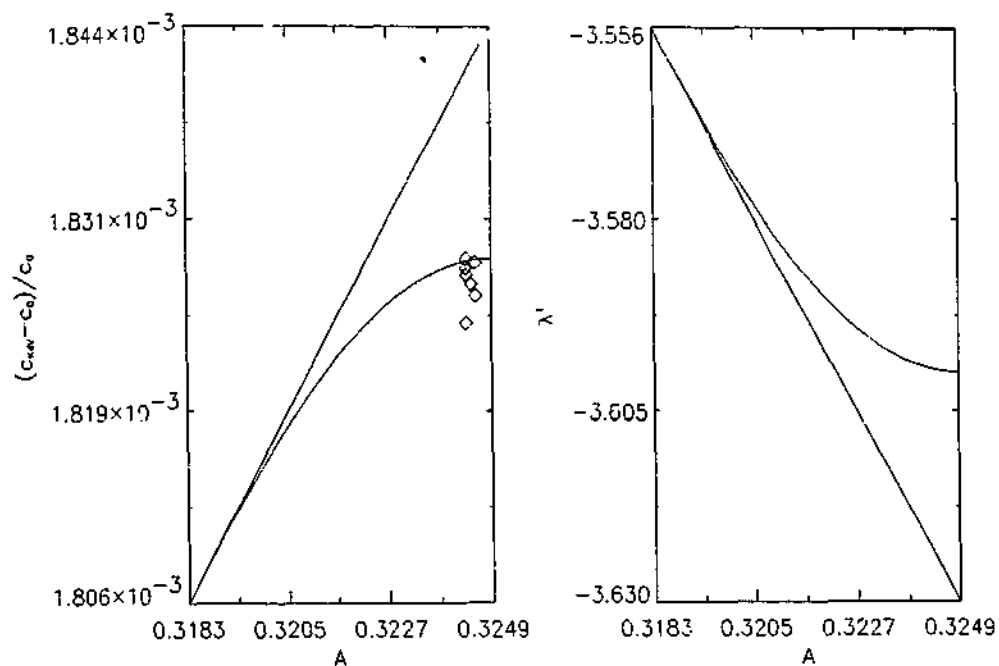
Figure 5.1: Relative phase speed $\frac{c-c_0}{c_0}$ and eigenvalue $\lambda^{(1)}$ for the KdV outer solution (bold) and KdV (dashed) solution for $\frac{1}{\pi} \leq A_{max} < \frac{1}{\pi} + \mu_{max}$; diamonds denote the numerical results.
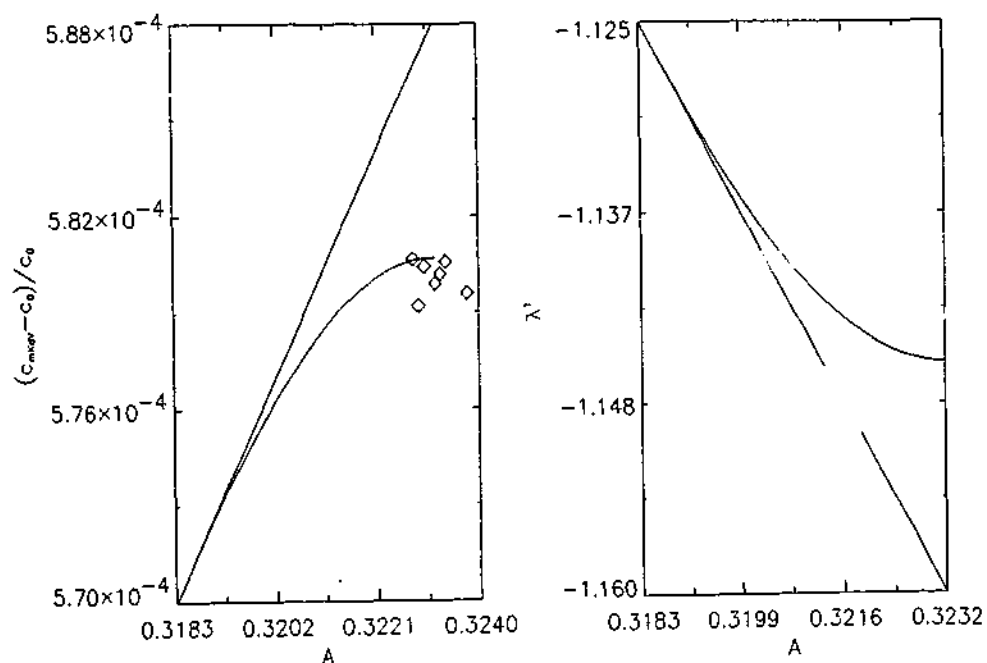


Figure 5.2: Relative phase speed $\frac{c-c_0}{c_0}$ and eigenvalue $\lambda^{(1)}$ for the mKdV outer solution (bold) and mKdV (dashed) solution for $\frac{1}{\pi} \leq A_{max} < \frac{1}{\pi} + \mu_{max}$; diamonds denote the numerical results.
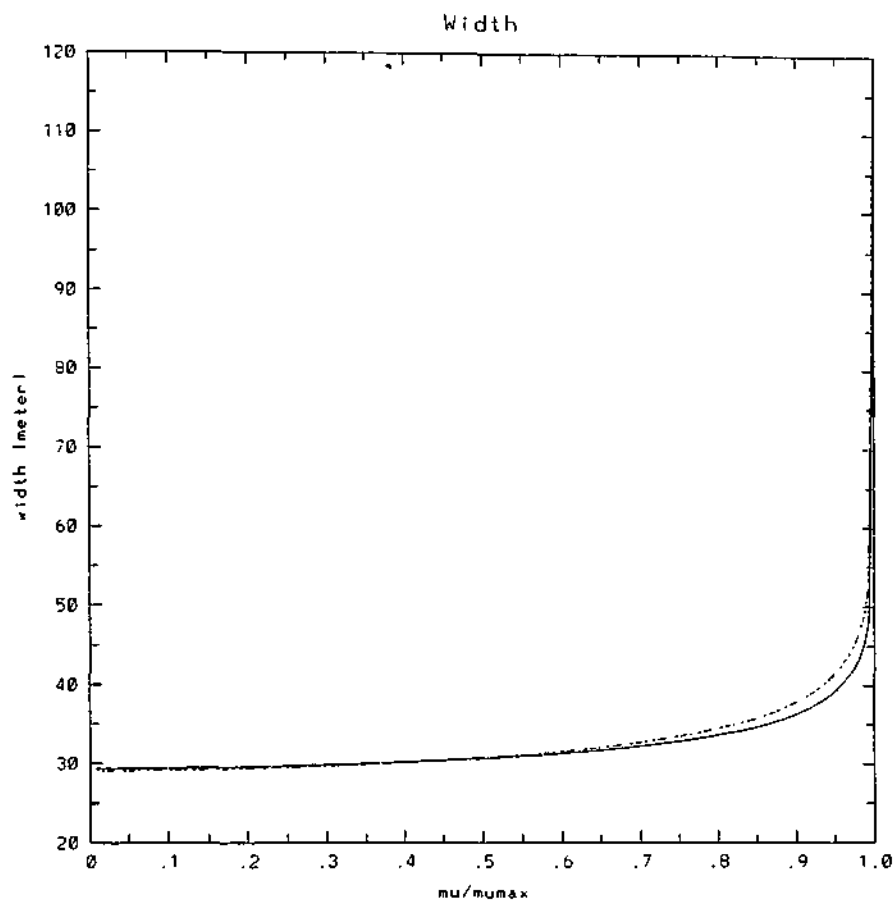
Figure 5.3: Plot of the width for $0 < \mu < \mu_{max}$ for the KdV (bold) and mKdV (dashed) outer solution ($\alpha_2 = 1$ and $\alpha_3 = 1$ resp.) for $\kappa = 0$.
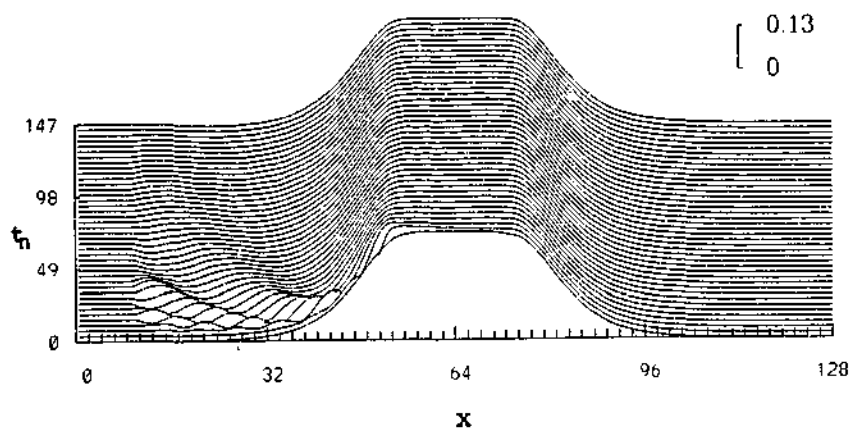


Figure 5.4: Time evolution of density at depth $\frac{2}{3}h$ for $\mu = 0.95\,\mu_{max}, \sigma = 0.01$, $\alpha_2 = 1$ and $\alpha_3 = 0$ (KdV outer solution).
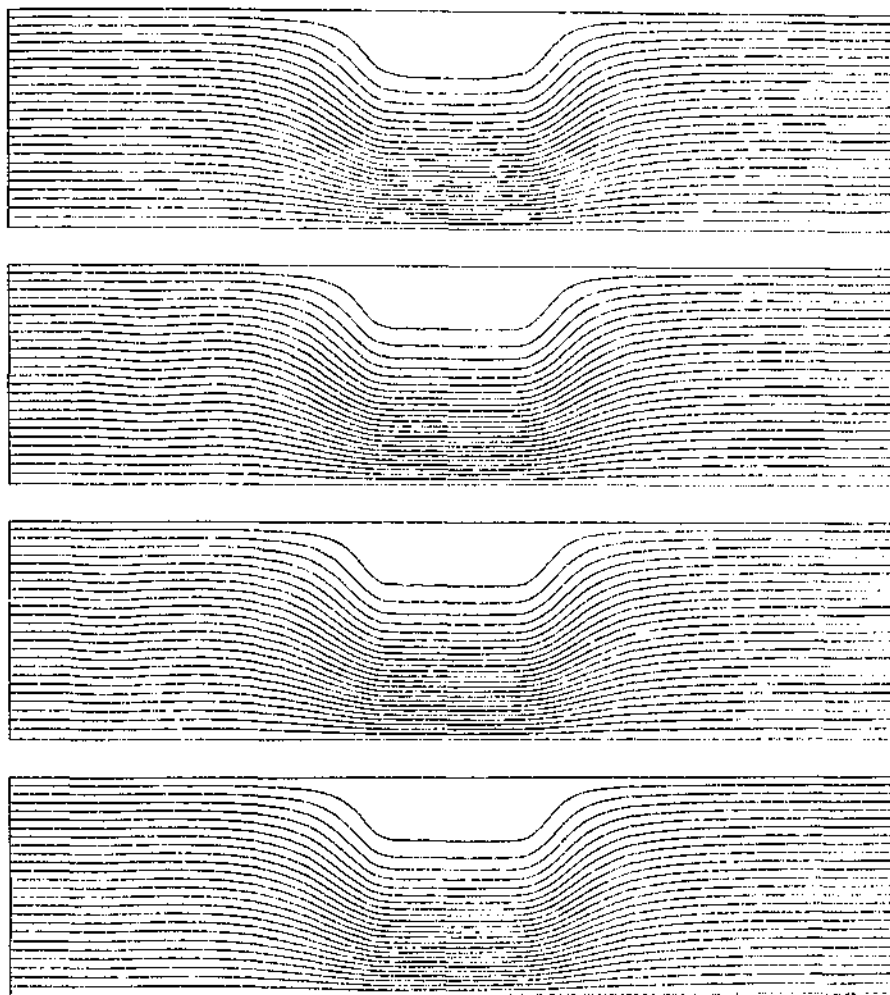
Figure 5.5: Density plots for normalized times $t_n = 0,69.89,106.67$ and $147.13$ and the parameters given in Figure 5.4. The x-axis is along the horizontal and the depth along the vertical.
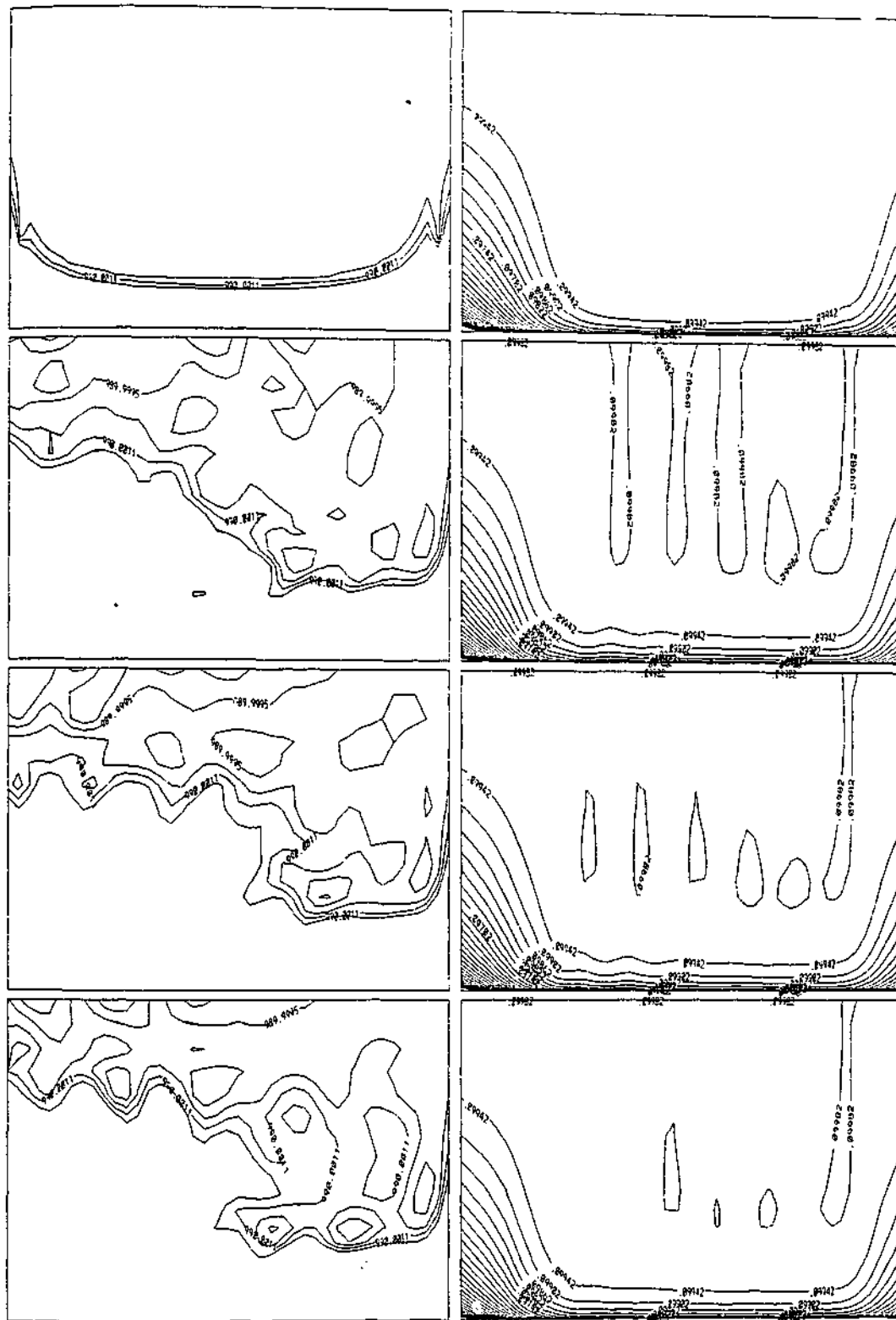
Figure 5.6: Plot of density (left) and streamfunction (right) for normalized times $t_n$ = 0,69.89,106.67 and 147.13 for the parameters given in Figure 5.4 inside of the recirculation region, $41 \times 23$ grid points resolution for $\rho$ and $61 \times 23$ grid points for $\psi$. Width along the horizontal and depth along the vertical.
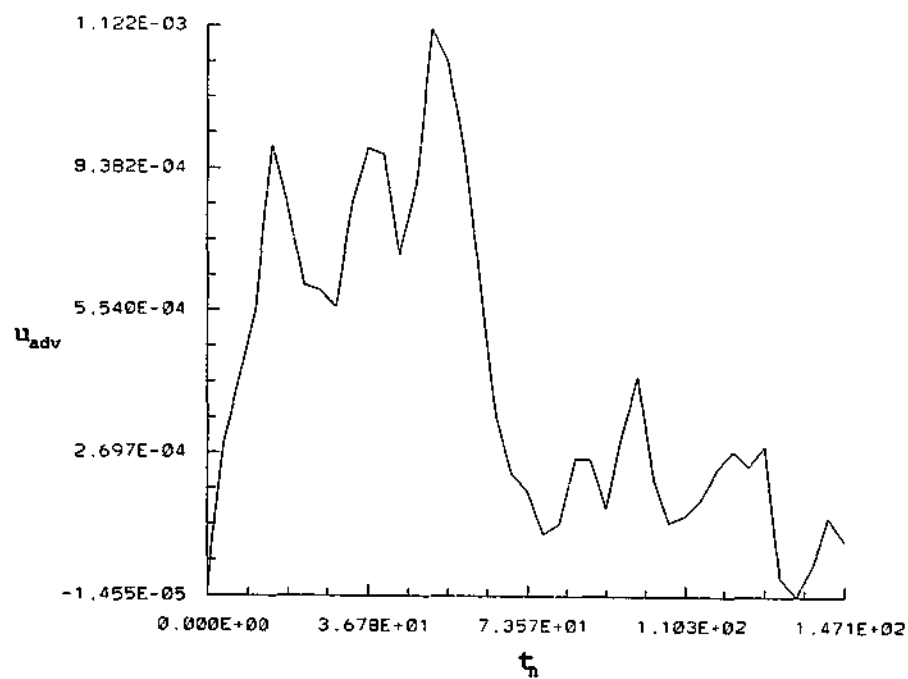
Figure 5.7: Maximum adverse velocity $u_{adv}$ at the upper boundary versus normalized time for the solution given in Figure 5.4.
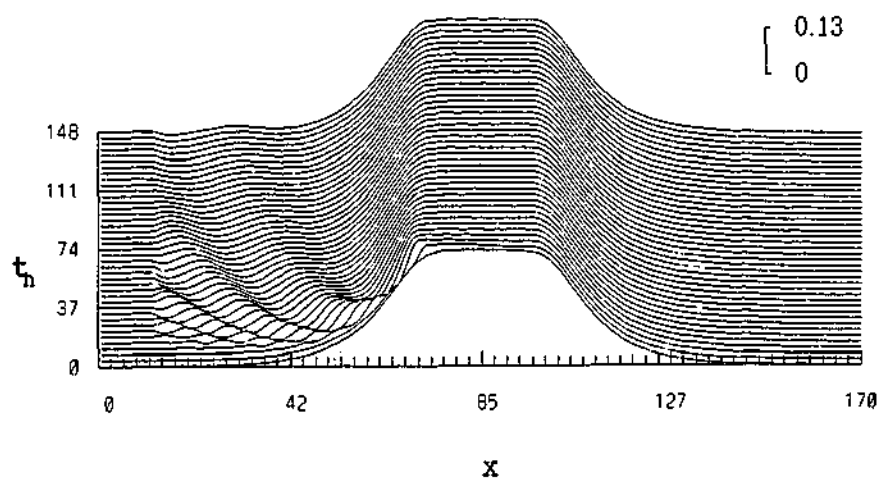


Figure 5.8: Time evolution of density at depth $\frac{2}{3}h$ for $\mu = 0.95\,\mu_{max}$, $\sigma = 0.01$, $\alpha_2 = -1.5$ and $\alpha_3 = 1$ (mKdV outer solution).
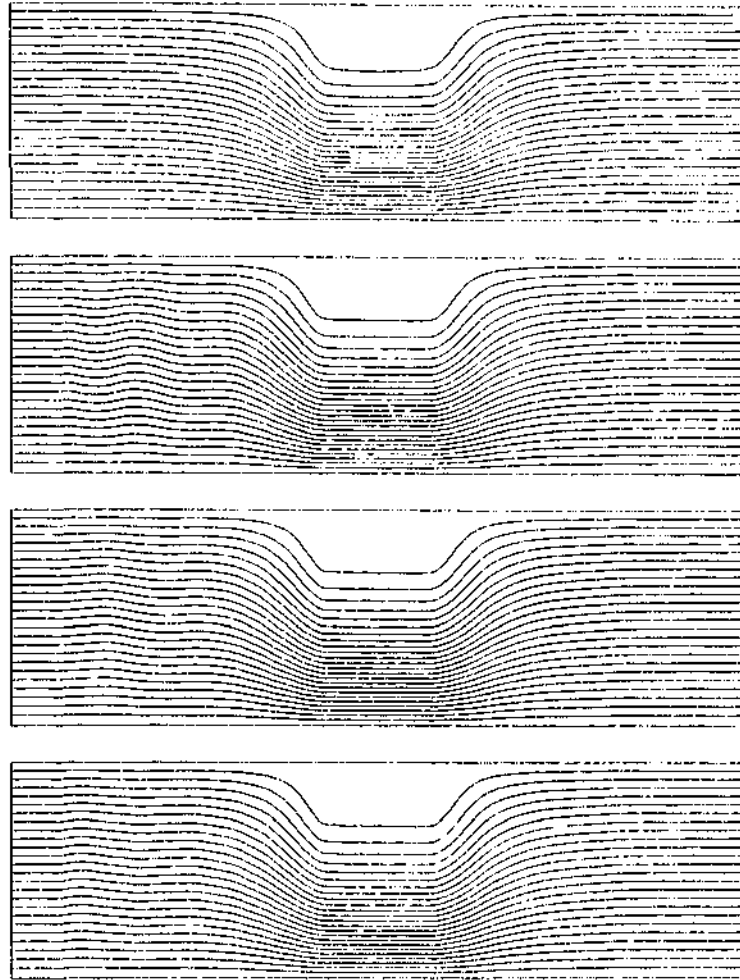
Figure 5.9: Density plots for normalized times $t_n = 0, 70.24, 107.21$ and $147.88$ and the parameters given in Figure 5.8. The x-axis is along the horizontal and the depth along the vertical.
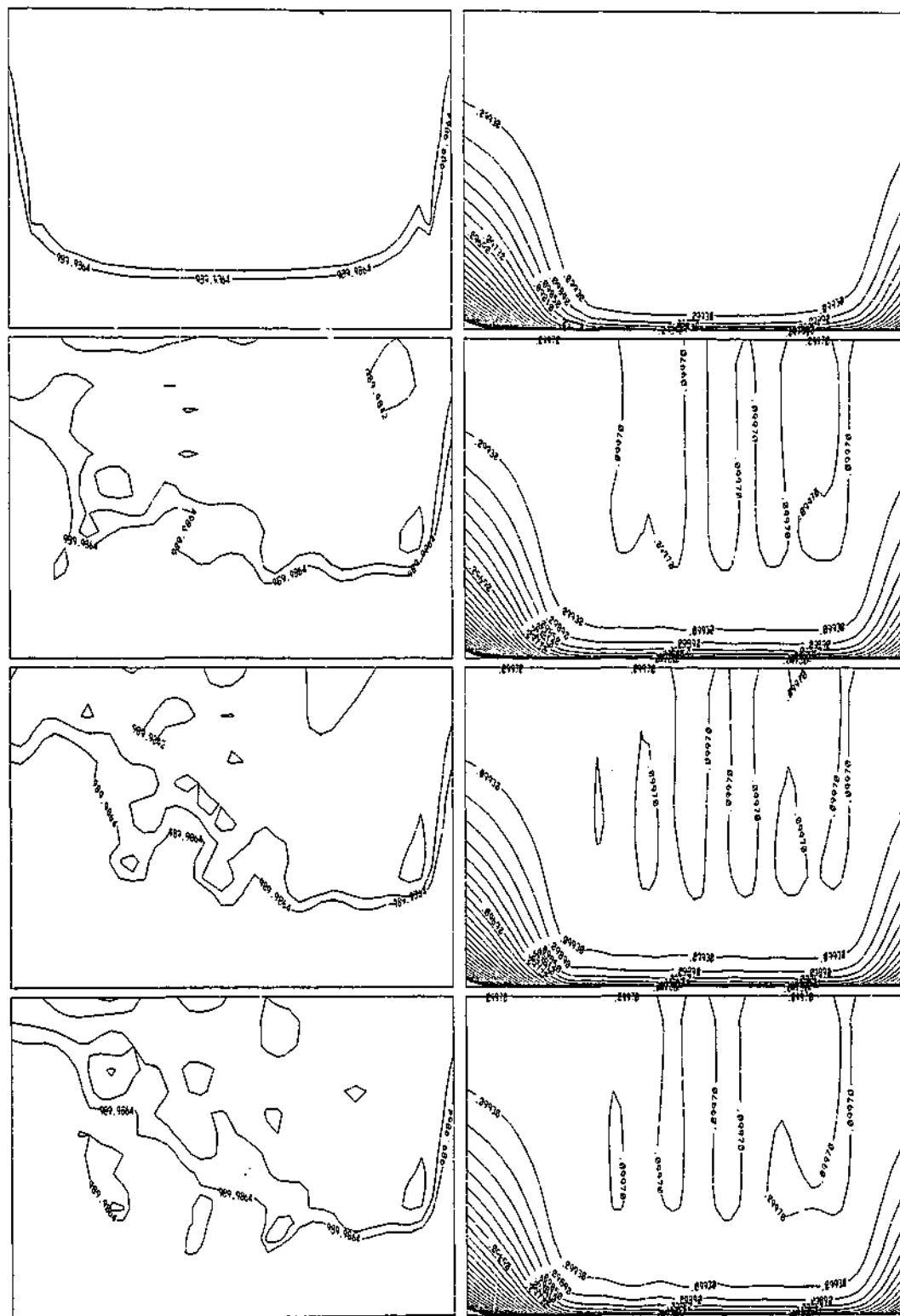
Figure 5.10: Plot of density (left) and streamfunction (right) for normalized times $t_n =$ 0,70.24,107.21 and 147.88 and the parameters given in Figure 5.8 inside of the recirculation region, $41 \times 23$ grid points resolution for $\rho$ and $61 \times 23$ grid points for $\psi$. The x-axis is along the horizontal and the depth along the vertical.
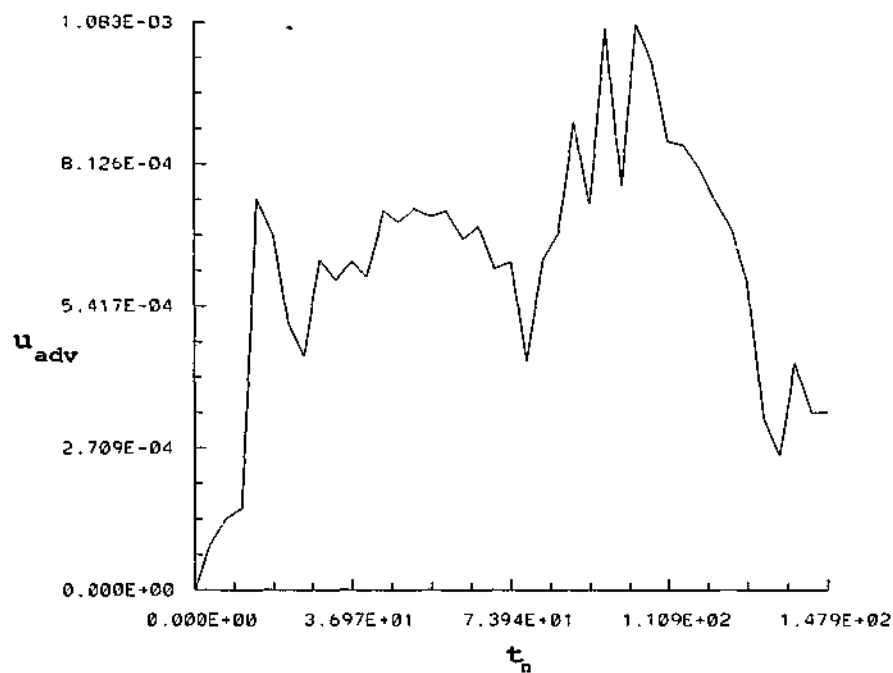
Figure 5.11: Maximum adverse velocity $u_{adv}$ at the upper boundary versus normalized time $t_n$ corresponding to the solution given in Figure 5.8.
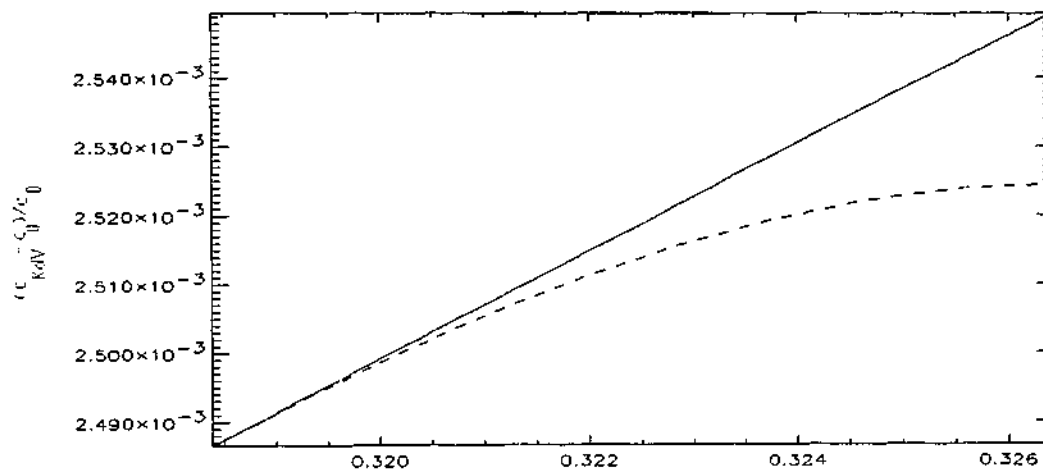


Figure 5.12: Plot of the phase speed versus the amplitude $A_* < A < A_* + \mu$ for the solitary wave with a vortex core and a KdV outer solution (dashed), and the phase speed of the traditional KdV solitary wave (solid) for the non-Boussinesq case ($c_0$ is the linear phase speed).
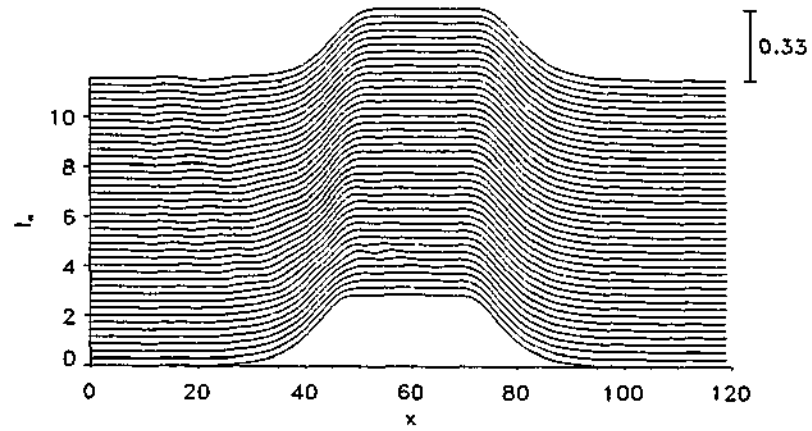
Figure 5.13: Plot of the streamfunction for a KdV outer solution at the depth $z = 2/3D$ for $\mu = 0.99\mu_{max}$, $\sigma = 0.01$ and $\tau_2 = 0$.
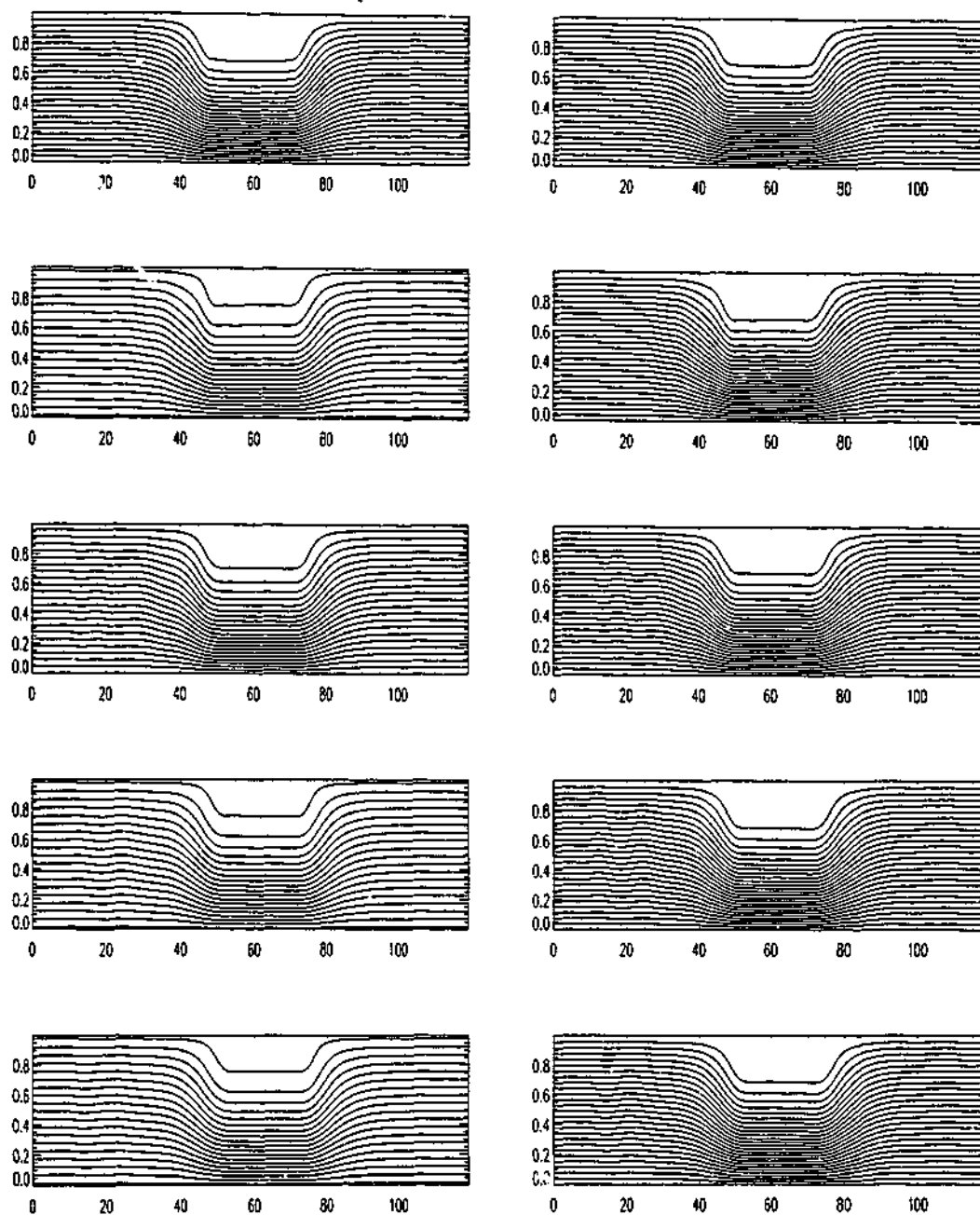
Figure 5.14: Density (left) and streamfunction (right) contour plots of the KdV outer solution with $\mu = 0.99\mu_{max}$, corresponding to Figure 5.13, for the non-dimensional times $t_n = 0, 2.8, 5.7, 8.6$ and $11.5$. Note that width is denoted along the horizontal and depth along the vertical.
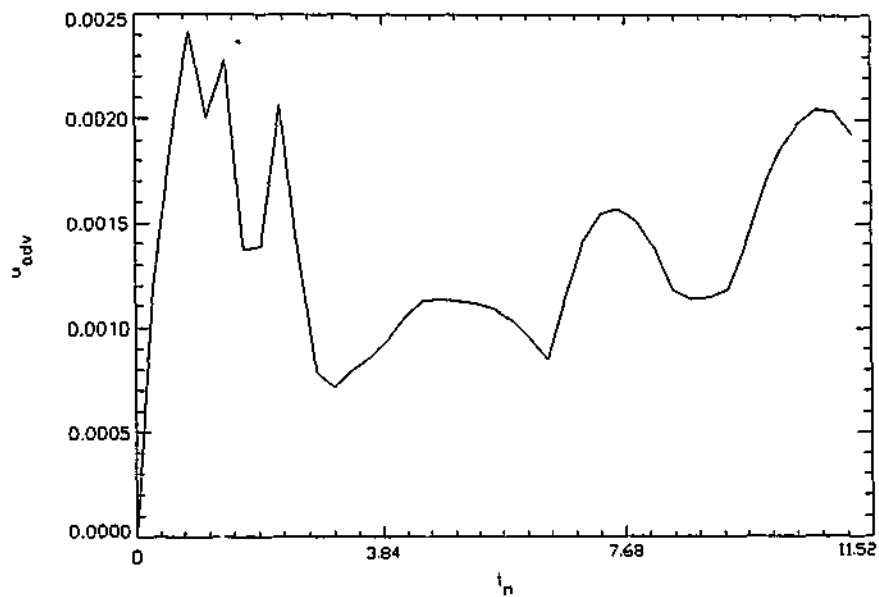
Figure 5.15: Plot of the maximum adverse velocity $u_{adv}$ versus non-dimensional time $t_n$ for the KdV outer solution given in Figure 5.14.
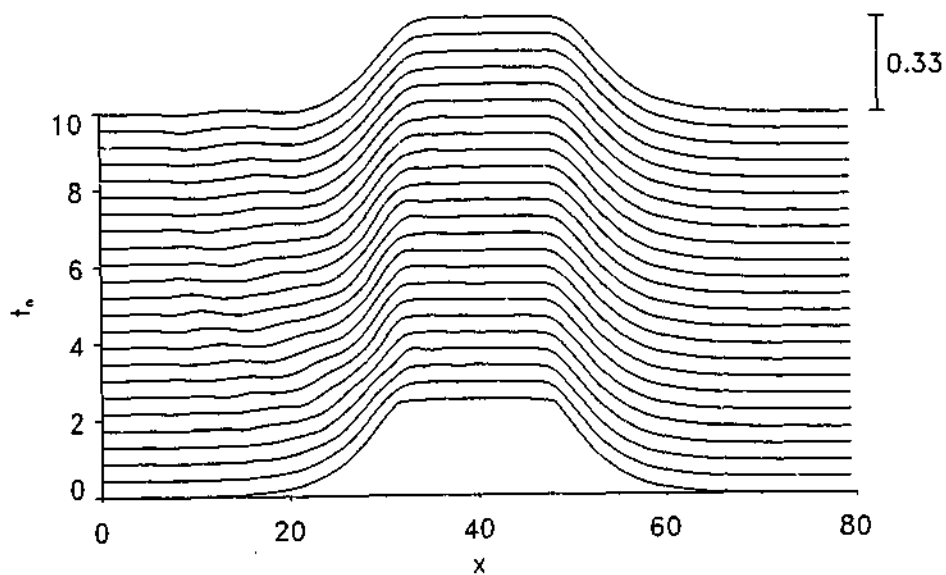


Figure 5.16: Plot of the streamfunction for a mKdV outer solution at the depth $z = 2/3D$ for $\mu = 0.99\mu_{max}$, $\sigma = 0.01$ and $\tau_1 = 0$.
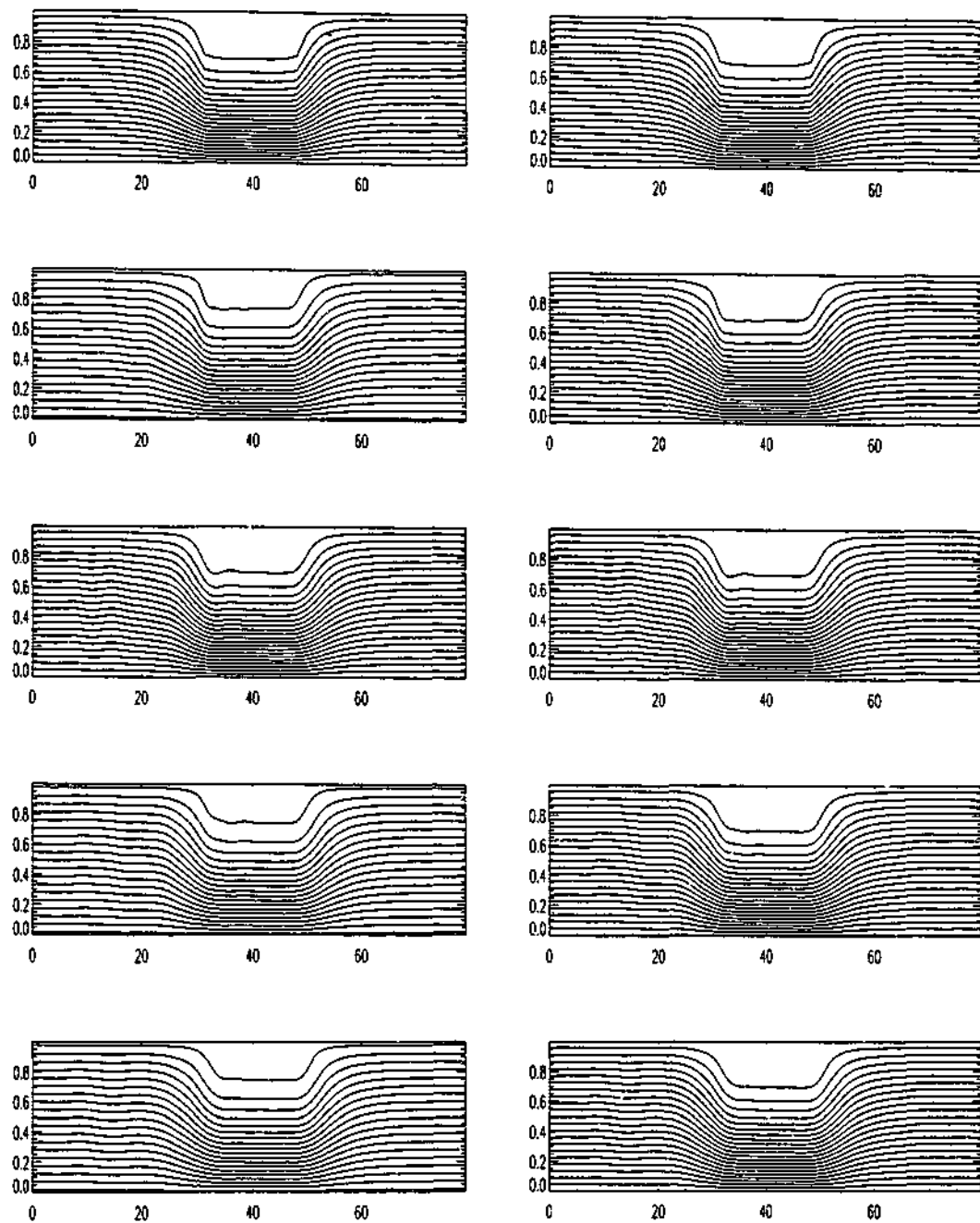
Figure 5.17:  Density (left) and streamfunction (right) contour plots of the mKdV outer solution with $\mu = 0.99\mu_{max}$, corresponding to Figure 5.16, for the non-dimensional times $t_n = 0, 2.5, 5.0, 7.5$ and $10.1$. Note that width is denoted along the horizontal and depth along the vertical.
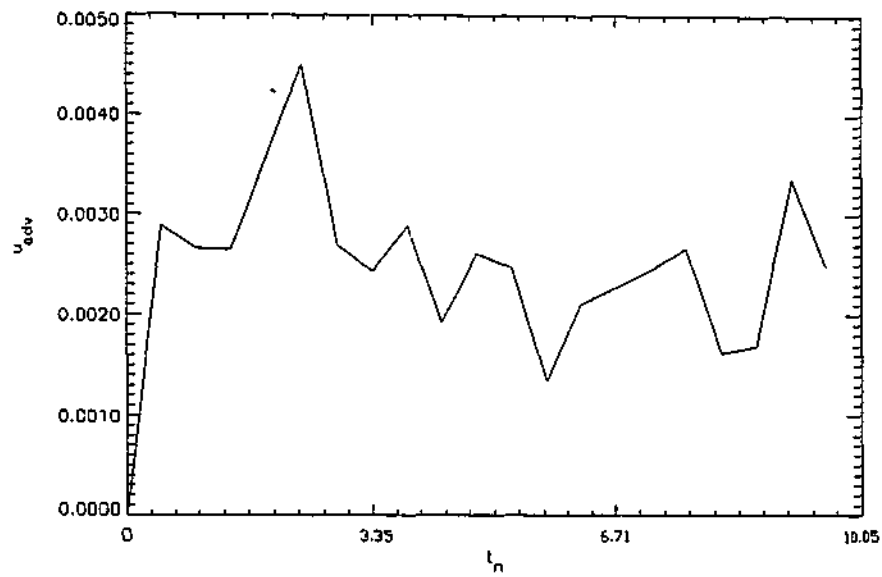
Figure 5.18: Plot of the maximum adverse velocity $u_{adv}$ versus non-dimensional time $t_n$ for the mKdV outer solution given in Figure 5.17.
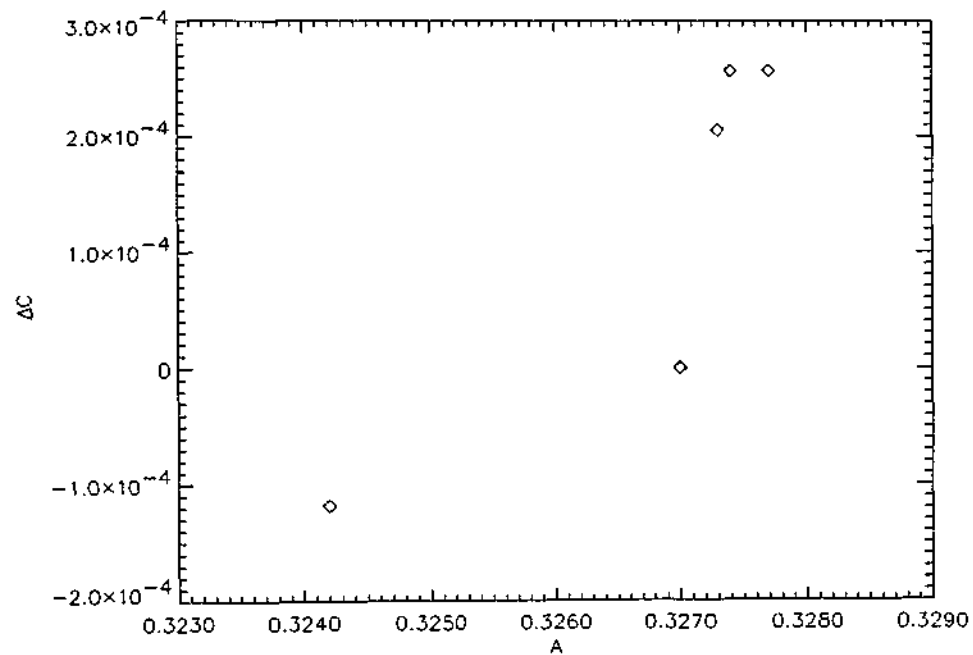


Figure 5.19: Plot of the absolute error in phase speed $\Delta c = c_{exp} - c$ of the phase speed in the numerical model $c_{exp}$ to the theoretical phase speed $c$, versus the amplitude $A_* < A < A_* + \mu$ of the solitary wave with a KdV outer solution. Notice that the error is constant over the time of integration, see, for example the streamfunction plot in Figure 5.13, where the upstream propagation of the wave is noticeable.

## 5.2  Stratified flow over topography

This section presents the numerical results of the non-Boussinesq model for resonant flow over topography. The basic density field is chosen to be

$$\bar{\rho}(z) = \rho_0 e^{\ln(1-\sigma)z/D}, \tag{5.2}$$

where $\sigma$ is a measure of the strength of the stratification, typically chosen to be $\sigma = 0.01$. Thus the Brunt-Väisälä frequency is given by

$$N^2 = -\frac{g}{D}\ln(1-\sigma) \tag{5.3}$$

and from equation (3.47) it follows that the Boussinesq parameter $\beta$ is 0.01. The flow speed is given by

$$U = \frac{ND}{\pi K}. \tag{5.4}$$

The region of stability for nonlinear hydrostatic flow in the Boussinesq limit $\beta \to 0$ is given by values for $K$ and $H = a/D$, which satisfy the following equation (see Rottman *et al* (1996) [58])

$$\pi H^* - |\sin(\pi(K^* - H^*))| \leq 0, \tag{5.5}$$

where $K^*$ and $H^*$ are given by

$$H^* = KH, \qquad K^* = K - n + 1; \tag{5.6}$$

$K$ is the inverse Froude number and $n$ the mode number. The region of instability and the cases examined in detail in the following are plotted in Figure 5.20.

The numerical model is valid until the disturbance starts to overturn anywhere in the fluid. This is called wave-breaking in the following and is relevant to the flow over topography. The nondimensional time that wave breaking occurs is called $t_{br} = Ut/D$ and is reached when the condition given by

$$\frac{\partial \rho}{\partial z} = 0$$

is satisfied anywhere in the flow. Wave breaking generates small-scale disturbances that are not resolved by the model and leads to aliasing errors and eventual numerical blow-up. Thus the time of wave-breaking is the final time of the numerical computation.

| $K^*$ | $t_{br} = Ut/D$ (nB) | $Ut/D$ (FALW) |
|---|---|---|
| 0.95 | * | * |
| 1.0 | 88.23 | 77.9 |
| 1.1 | 28.83 | 25.9 |
| 1.2 | 23.74 | 21.1 |

*Table 5.2* Table of nondimensional breaking times $t_b r$ for the non-Boussinesq model (nB) and the finite-amplitude long-wave model (FALW).

In Figure 5.21 at the non-dimensional time $Ut/D \approx 24$ the disturbance has reached wave-breaking ($\rho_z \approx 0$) and the numerical model fails shortly after.

Four cases are of specific interest: when the inverse Froude number $K$ is $1.2, 1.1, 1.0$ and $0.95$. The nondimensional hill height is chosen to be $H^* = 0.1$, that is, the nondimensional parameter $Ka/D$ equals 0.1 for all four cases considered. The length to depth ratio is $L/D = 2.0$. Figure 5.21 shows a plot of the streamfunction computed by the spectral numerical model for $K = 1.2$, when it is essentially parallel to the density contours. Note the development of the deep trough downstream of the obstacle near the maximum slope of the hill and at the upper boundary at around $Ut/D \approx 30$.

The evolution in time of the amplitude function $A(x,t)$ for the resonant mode as computed by the spectral model, is plotted in Figure 5.22 and by the FALW model in Figure 5.23, for the cases $K = 1.2, 1.1$ and $K = 1.0$ up to the breaking time $t_{br}$ (refer to Table 5.2 for the exact breaking times of these cases). The amplitude function for the case $K = 0.95$ is plotted in Figure 5.24. The flow approaches a steady state without breaking.

In Figure 5.25, the maximum absolute amplitude $|A|_{max}$ normalized by the maximum possible amplitude $|A_*|$ for the cases considered is plotted up to the breaking time $t_{br}$. The solid lines show the results for the spectral model; dashed lines the results from the FALW model. In all these cases the amplitude increases nearly linearly with time as predicted by linear resonant theory for times up to $Ut/D \approx 10$. For $K = 0.95$, the growth ceases altogether, which is also consistent with linear theory. For $K' = 1.0$, which is exactly on the margin of instability (confer with Figure 5.20), the growth is

very slow, but eventually reaches the breaking amplitude. For $K > 1$ the growth rate increases with $K$. For $K = 1.2$ the growth is close to linear. Note that the growth as predicted by the FALW model is always bigger than the amplitude of the resonant mode calculated by the spectral model for $K \geq 1$.

For $K = 1.0$ and $1.1$, the downstream trough grows to a breaking amplitude and the vertical position of breaking is located at the upper boundary. In Figure 5.26, the vertical position of breaking is plotted for several cases of the inverse Froude number in the range $1.0 \leq K \leq 1.2$. Note that the vertical position is always off centre and changes from close to the upper boundary to close to the lower boundary, and simultaneously from downstream to upstream. For $K = 1.2$ the development is similar, albeit more rapid. Nonetheless, the crest that develops over the obstacle does not start to propagate upstream as given in the results of Grimshaw and Yi (1991) [32] (see in particular Figure 3). Overall, the FALW model and the spectral model compare quite well in their time-dependent behaviour.

The drag $F_D$ on the obstacle is plotted in Figure 5.27, where the drag force is given by

$$F_D = \int_{-\infty}^{\infty} p\frac{dh}{dx}dx$$

and $p$ is the pressure evaluated on the lower boundary. The plot of the drag shows the agreement as well. Again, solid lines represent the spectral model and dashed lines the FALW model. The FALW model slightly underpredicts the drag for $K < 1.2$.

For $K = 0.95$, which does not lead to breaking waves (see Figure 5.20) the drag approaches zero, indicating that the flow eventually becomes symmetric about the obstacle. For $K \geq 1.0$ the drag is non-zero, when breaking occurs, and the model indicates that even after breaking it remains non-zero. This implies that the flow becomes asymmetric about the obstacle with a high pressure on the upstream side and low pressure on the downstream side.

The results presented here for the fully nonlinear case are consistent with the results obtained by Rottman *et al* (1996) [58]. The spectral model slightly underpredicts the FALW model, whereas it is just the opposite case in the Boussinesq spectral model.

The drag computation of the spectral model slightly exceeds the FALW model, as is the case in the Boussinesq spectral model.

The non-dimensional amplitude of the obstacle used by Rottman *et al* (1996) [58] and in this study are different from the scaled obstacle height used by Grimshaw and Yi (1991) [32] , since equations *(4.2-4)* therein state that $a = \frac{c_n D}{2N_0} f_0$. In addition to the improved computation of the kernel of the FALW equation by Rottman *et al* (1996) [58] , the weak correlation between the results of Rottman *et al* (1996) [58] , the results presented here, as compared to the results by Grimshaw and Yi (1991) [32] are attributed to the above mentioned fact.
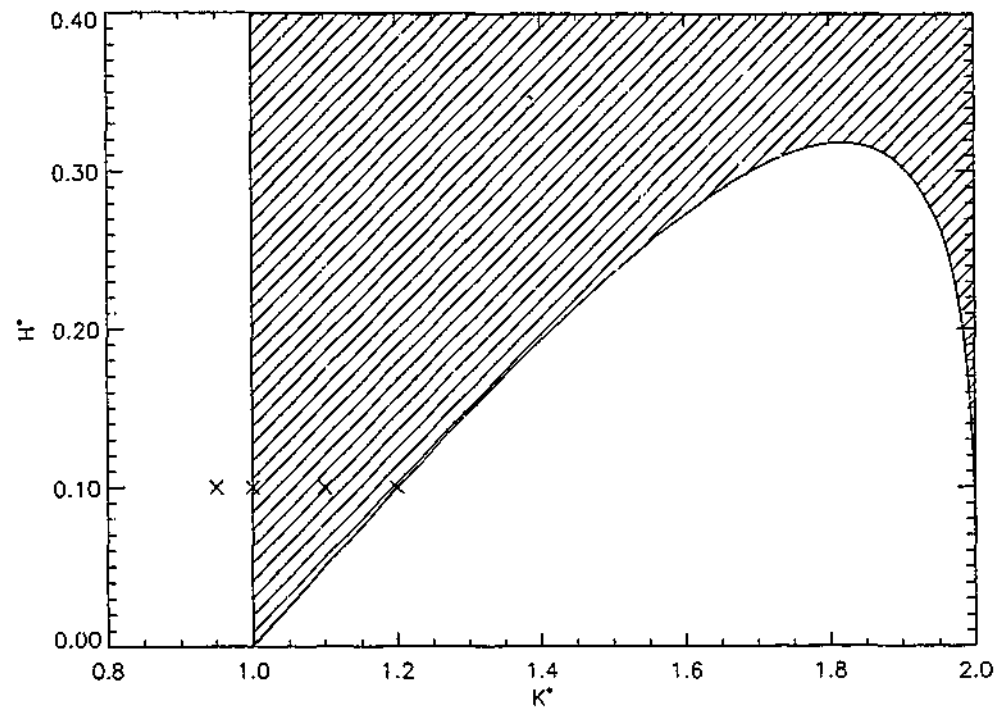
Figure 5.20: The $K^* - H^*$ parameter space diagram based on the hydrostatic Long's model solution for flow over two-dimensional obstacles. Crosses denote the cases $K^* = 0.95, 1.0, 1.1, 1.2$, plotted in Figures 5.22 to 5.24. The hatched region denotes the region of instability for values of $K^*$ and $H^*$ which do not satisfy equation (5.5).
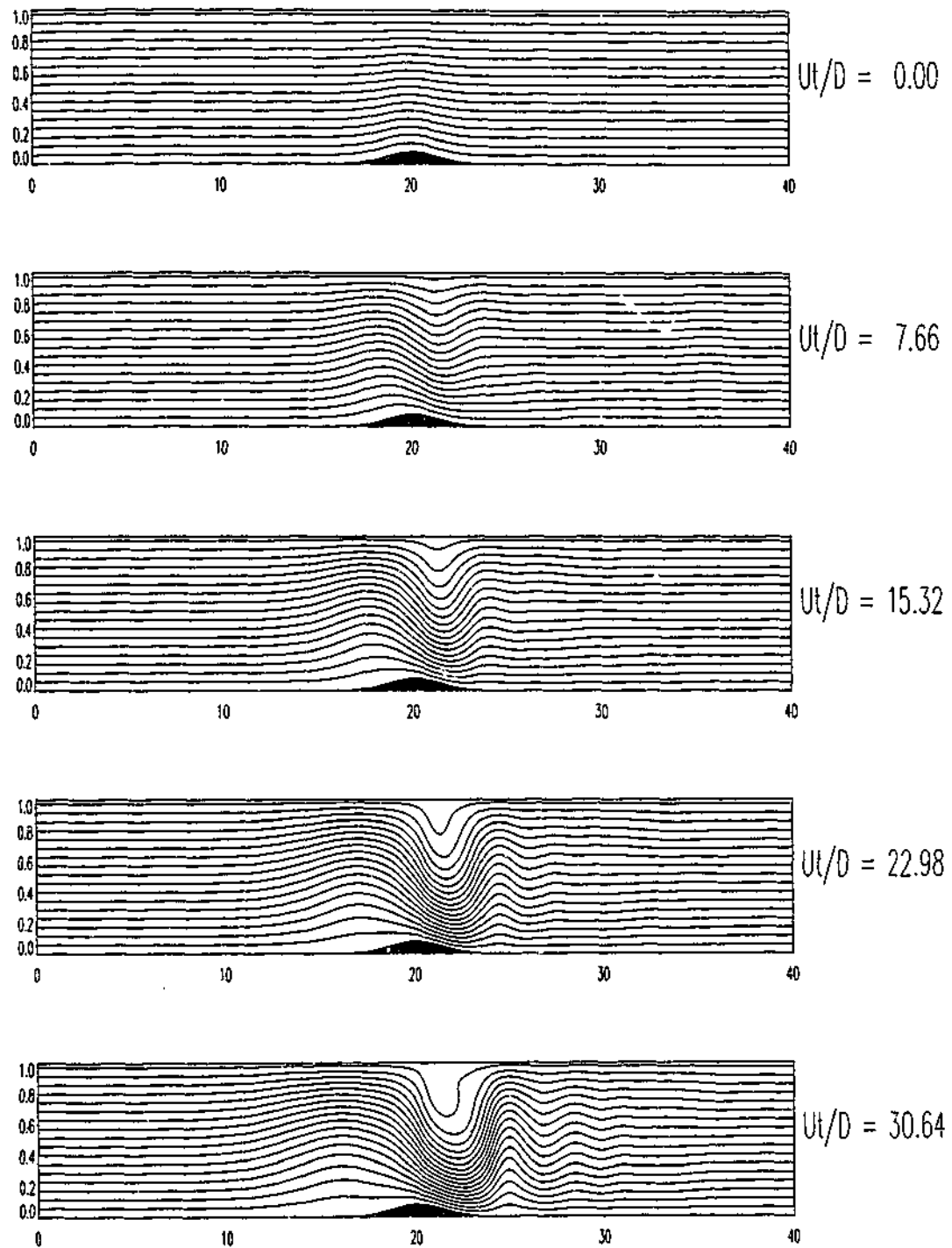
Figure 5.21: Contour plot of the streamfunction for $K = 1.2$ and $H^* = 0.1$ at the times $Ut/D = 0.0, 7.66, 15.32, 22.98, 30.64$. Breaking occurs at $t_{br} = Ut/D = 23.74$. The width of the domain is denoted along the horizontal and the depth along the vertical.

(a)



(b)



(c)
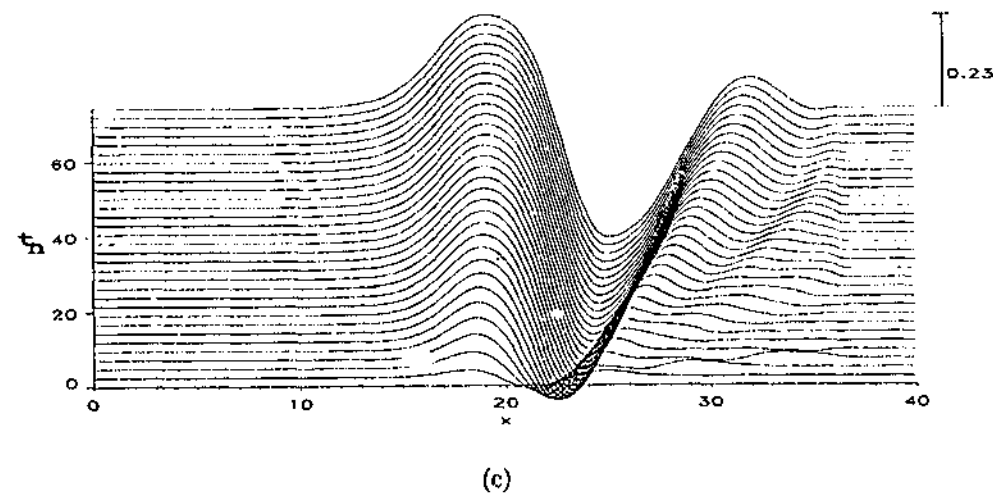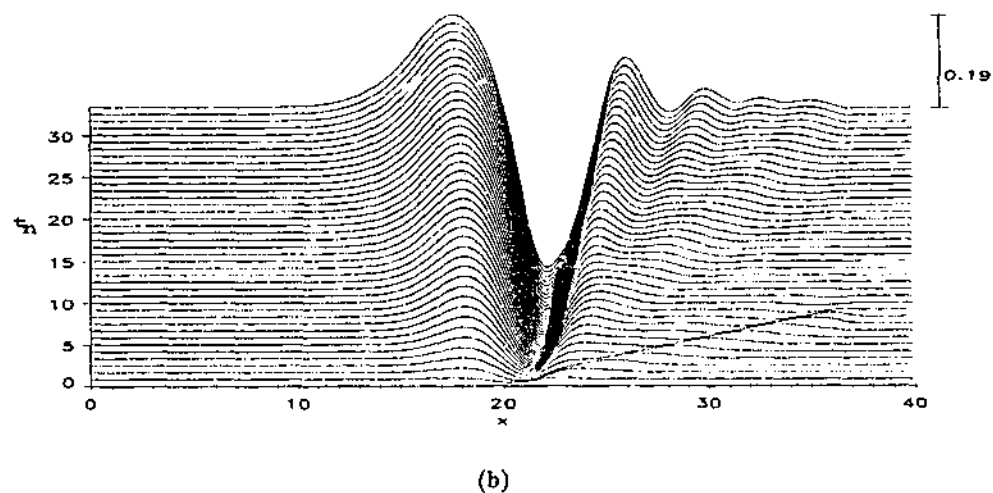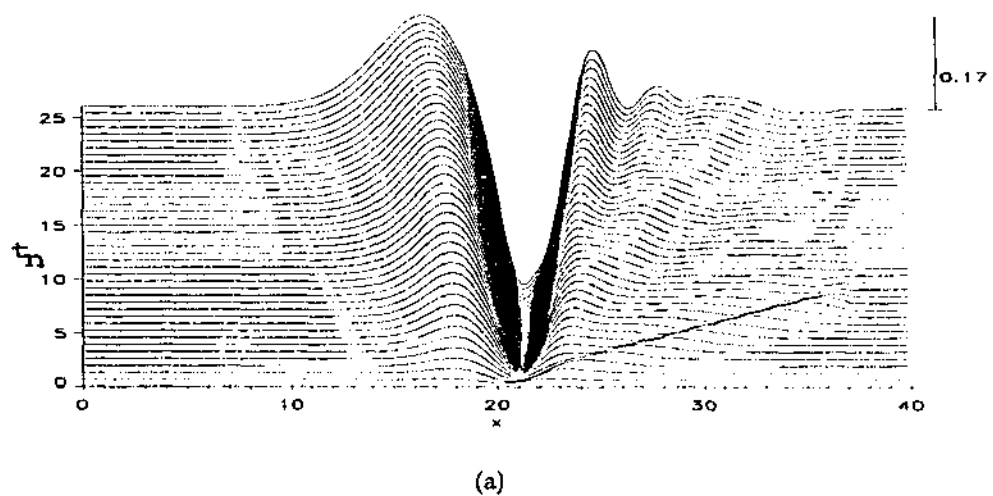
Figure 5.22: Plot of the amplitude function $A(x,t)$ for the resonant mode of vertical displacement as computed by the spectral model for the case with $H^* = 0.1$, $L/D = 2.0$ and (a) $K = 1.2$, corresponding to the case shown in figure 5.21, (b) $K = 1.1$ and (c) $K = 1.0$. The obstacle is centered at $x/D = 20$. The corresponding breaking times are $t_{br} = 23.7, 28.8, 88.2$.
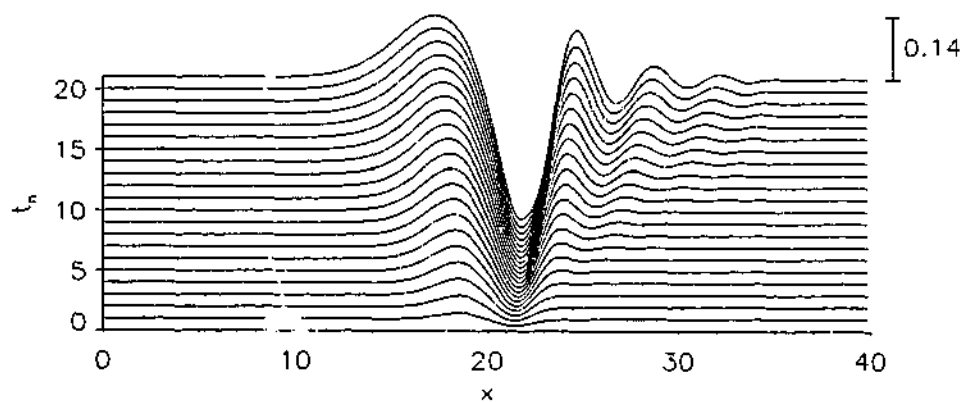
(a)
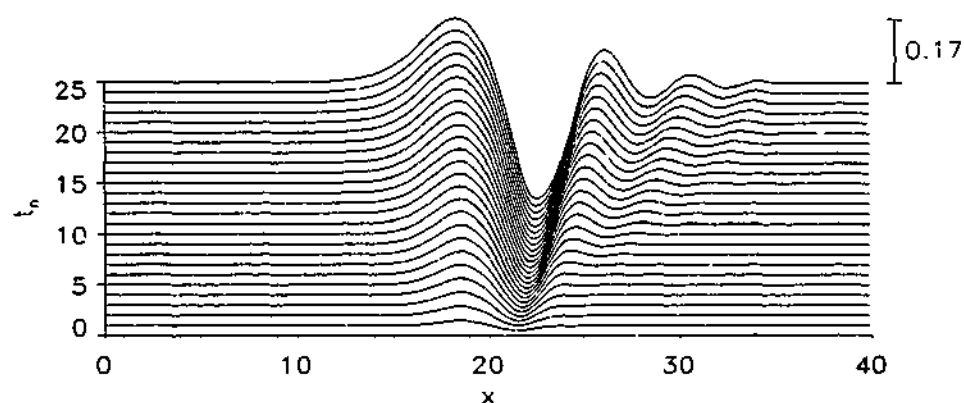


(b)
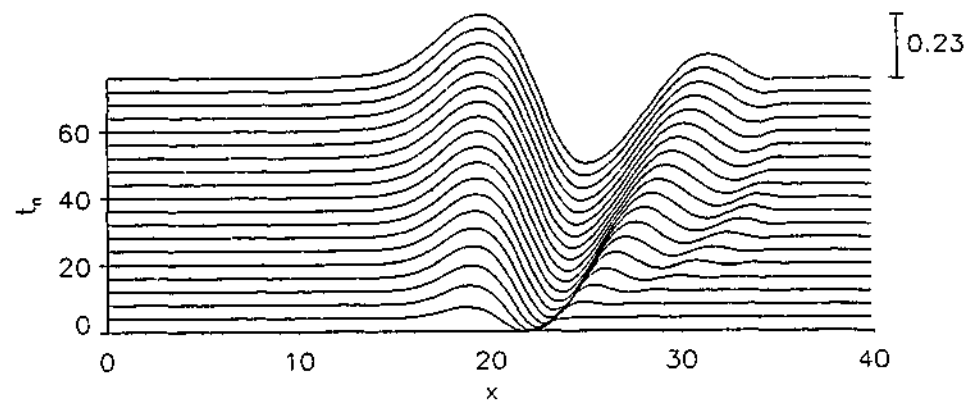


(c)

Figure 5.23: Plot of the amplitude function $A(x,t)$ for the resonant mode of vertical displacement as computed by the FALW model for the case with, $H^* = 0.1$, $L/D = 2.0$ and (a) $K = 1.2$, (b) $K = 1.1$ and (c) $K = 1.0$. The obstacle is centered at $x/D = 20$. The corresponding breaking times are $t_{br} = 21.1, 25.9, 77.9$.

(a)

(b)
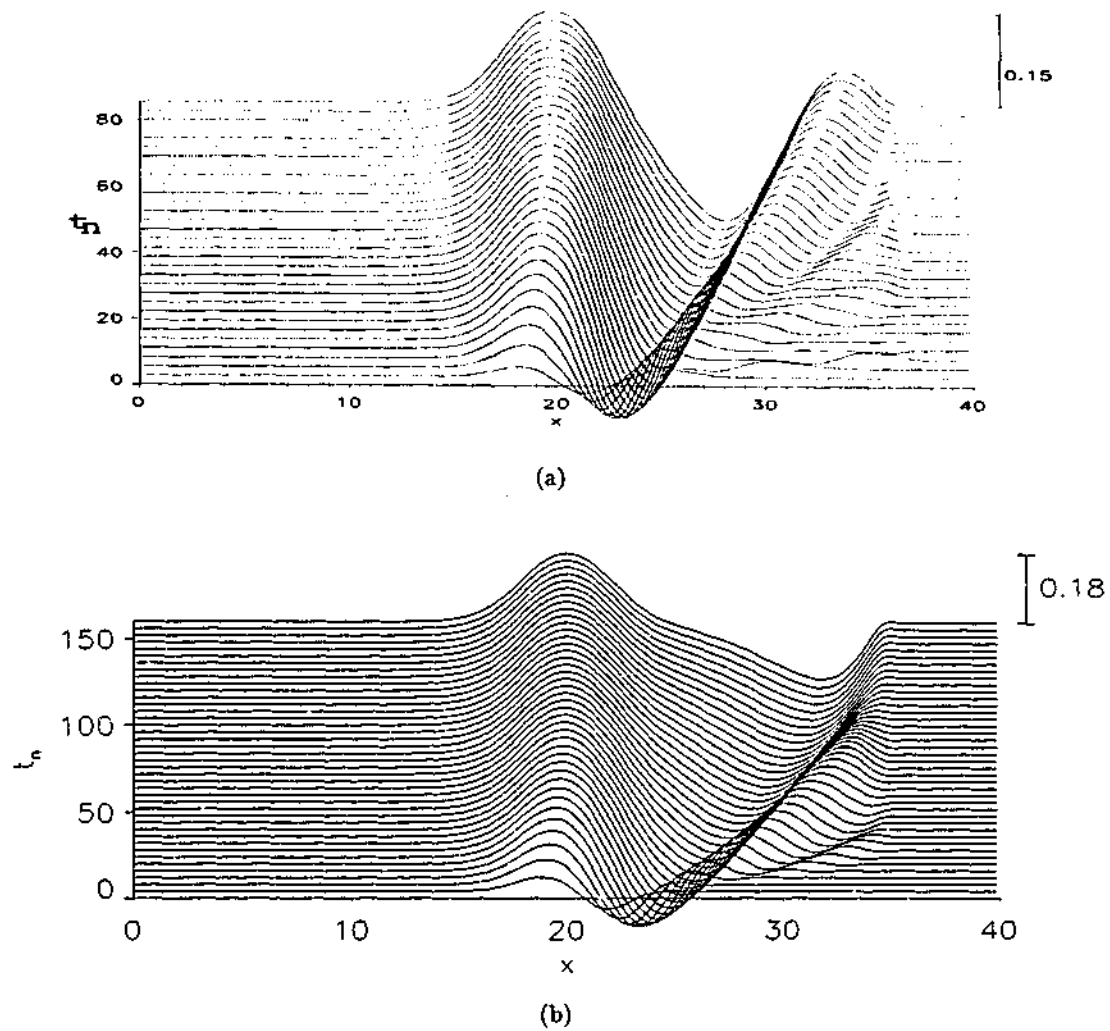
Figure 5.24: Plot of the amplitude function $A(x,t)$ for the resonant mode of vertical displacement as computed by a) the spectral model and b) the FALW model for the case with, $H^* = 0.1$, $L/D = 2.0$ and $K = 0.95$ up to the time $Ut/D = 115$ and 160 respectively. The obstacle is centered at $x/D = 20$.
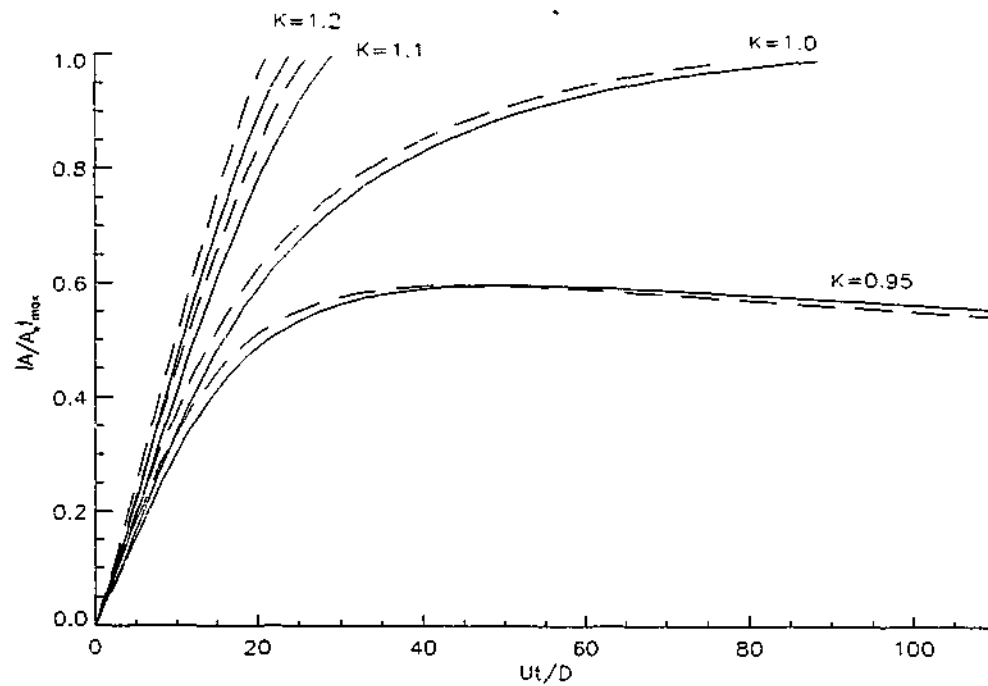
Figure 5.25: Plot of the maximum absolute amplitude normalized by the maximum possible amplitude $|A/A_*|_{max}$ as a function of time, corresponding to the calculations for $K = 0.95$, 1.0, 1.1 and 1.2: The solid lines indicate the spectral model and the dashed lines the FALW model.
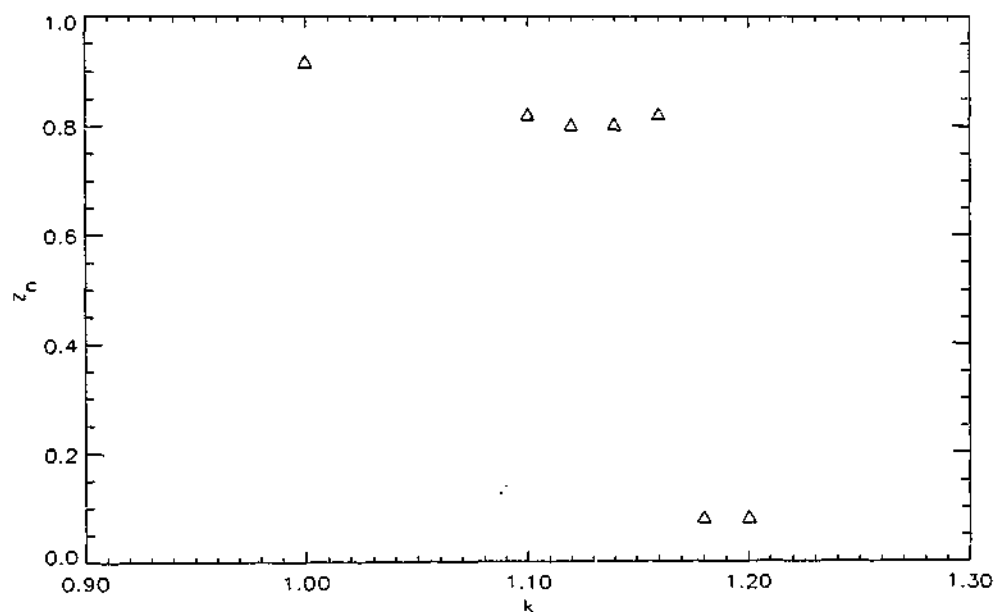


Figure 5.26: Normalized vertical position $z_n = z/D$ of wave breaking for several cases, $1.0 \leq K \leq 1.2$, note that the breaking location is either at the top or at the bottom and sets in downstream or upstream of the hill.
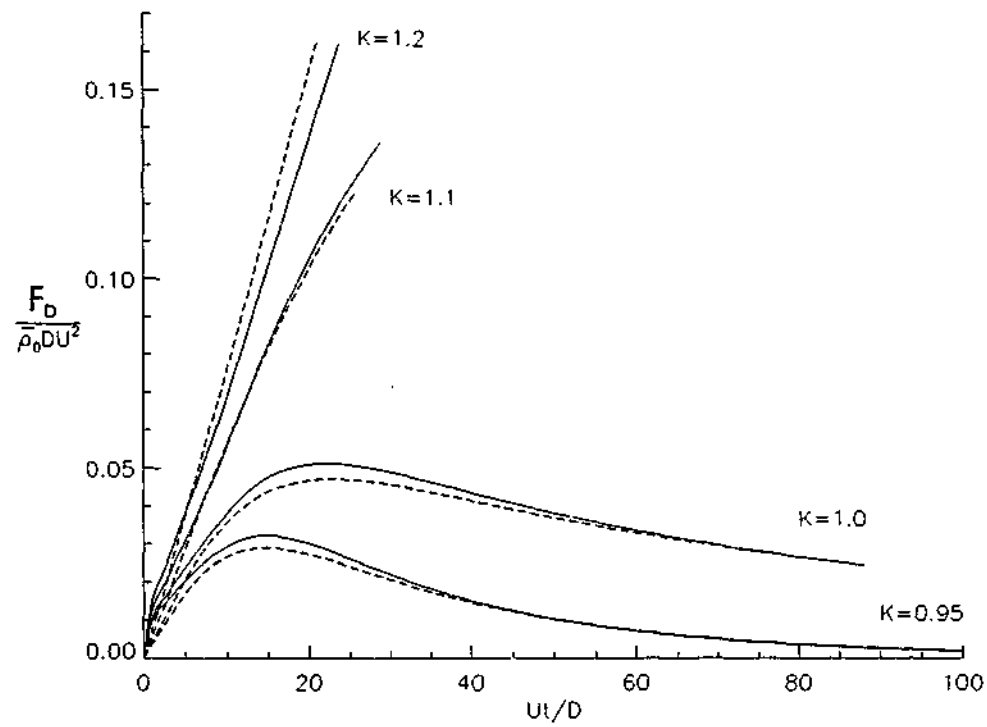
Figure 5.27: Plot of the drag as a function of time on the hill of height $H^* = 0.1$ corresponding to the calculations for $K = 0.95$, 1.0,1.1 and 1.2: The solid lines indicates the spectral model and the dashed lines the FALW model.

## 5.3    Multi-scale internal solitary waves

Two multi-scaled internal solitary waves are considered for large and medium wave-
lengths.    Time is normalized with the typical length scale of the wave $W$ and the
uniform flow speed $U$. Figure 5.28 shows the streamfunction at a depth $\frac{2}{3}h$ and Figure
5.29 the corresponding streamfunction field at four respective non-dimensional times
for $\alpha_3 = 1.001$ and $A_0 = 0.3$. The final time is about six hours, which is long enough
to consider the wave to be of permanent shape. Figure 5.30 and 5.31 show the stream-
function for $\alpha_3 = 1.1$ and $A_0 = 0.3$. The solutions show little change of shape and agree
with the solutions derived by Derzho and Velarde (1995) [17] to within the accuracy of
the numerical model.

In order to illustrate that the solutions are not valid for amplitudes greater than
the maximum amplitude $A = A_*$ a solution with maximum amplitude $A_0 = 0.6$ is used
in Figures 5.32 and 5.33. It shows a very rapid change in the maximum amplitude
and a downstream propagation of perturbations to a steady state solution of smaller
amplitude.
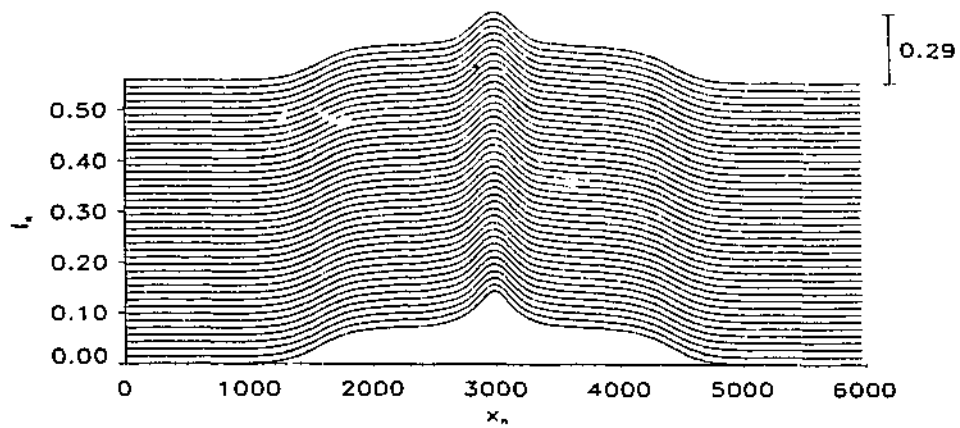
Figure 5.28: Plot of the streamfunction at $\frac{2}{3}h$ versus normalized time $t_n = t\frac{U}{W}$ for the parameters $\alpha_3 = 1.001$ and $A_0 = 0.3$.
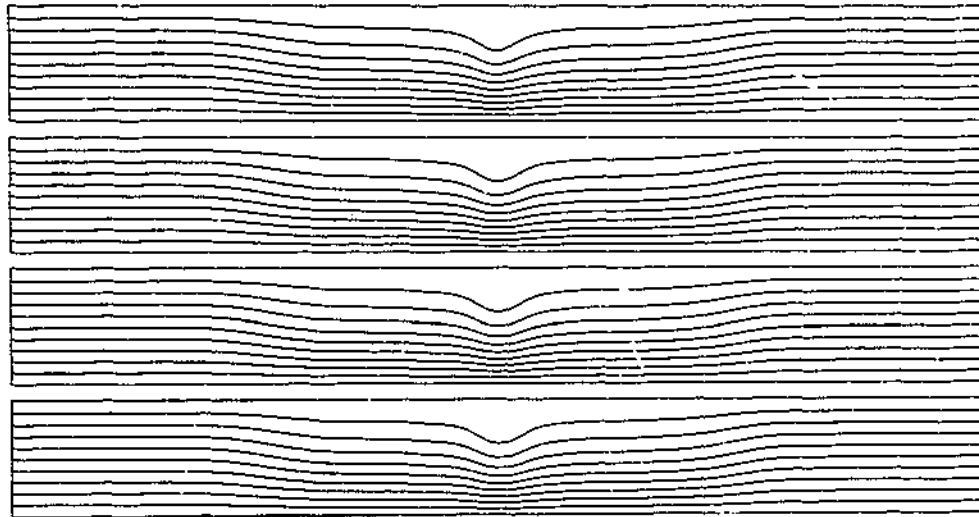


Figure 5.29: Plot of the streamfunction field for the parameters given in Figure 5.28 and normalized times $t_n = 0.0, 0.12, 0.37$ and $0.56$. Along the horizontal is the width of the domain and across the vertical the depth of the fluid.
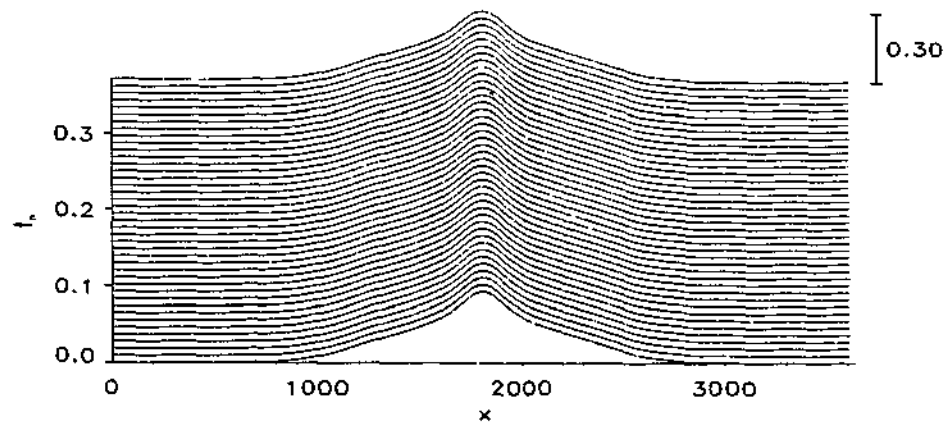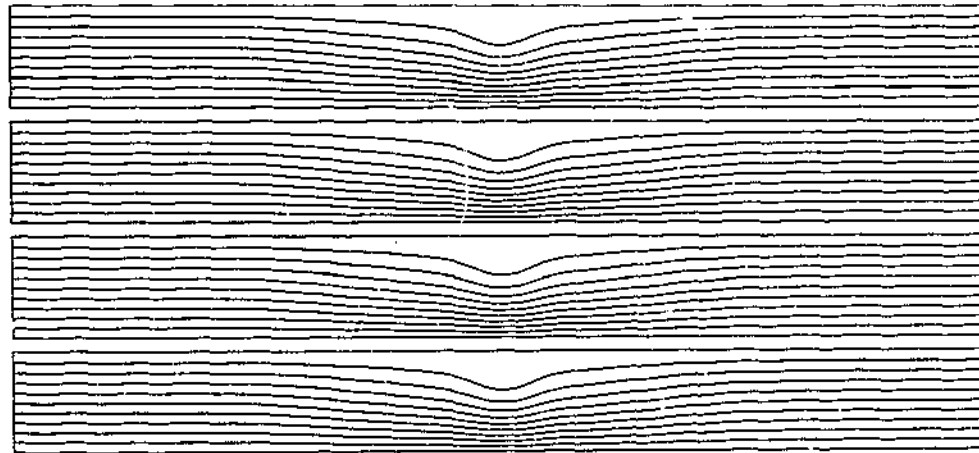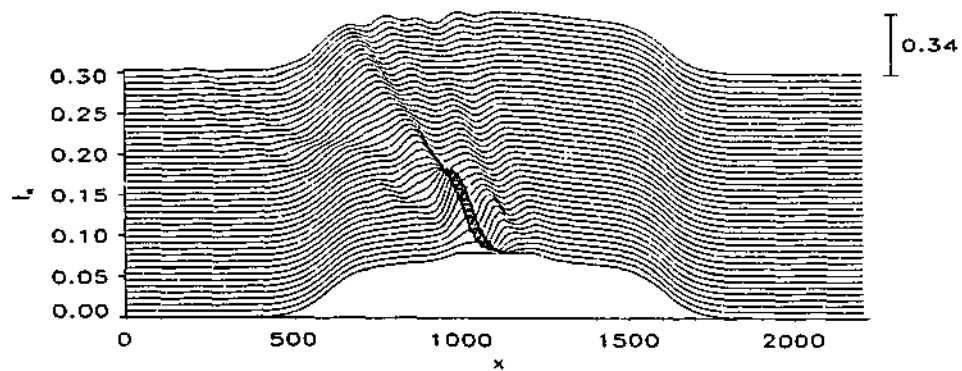
Figure 5.30: Plot of the streamfunction at $\frac{2}{3}h$ verus normalized time $t_n = t\frac{U}{W}$ for the parameters $\alpha_3 = 1.1$ and $A_0 = 0.3$.



Figure 5.31: Plot of the streamfunction field for the parameters given in Figure 5.30 and normalized times $t_n = 0.0, 0.12, 0.25$ and $0.37$. Along the horizontal is the width of the domain and across the vertical the depth of the fluid.

Figure 5.32: Plot of the streamfunction at $\frac{2}{3}h$ verus normalized time $t_n = t\frac{U}{W}$ for the parameters $\alpha_3 = 1.001$ and $A_0 = 0.6$. Notice that the solution is unstable for parameters outside the validity.
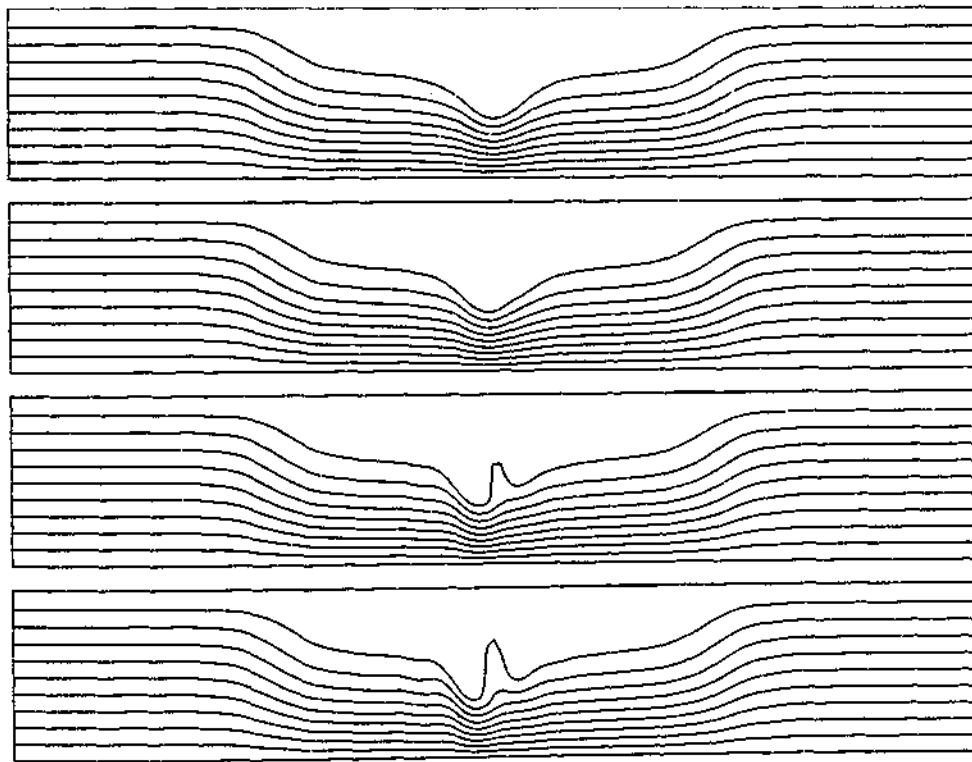


Figure 5.33: Plot of the streamfunction field for the parameters given in Figure 5.32 and normalized times $t_n = 0.0, 0.1, 0.2$ and $0.3$. Along the horizontal is the width of the domain and across the vertical the depth of the fluid.

|   | $a_1$ | $a_2$ | $b_1$ | $b_2$ | Type | $\Omega_0$ | $\kappa$ | $\sigma$ | $\epsilon$ | $\mu$ |
|---|---|---|---|---|---|---|---|---|---|---|
| 1 | 0.1 | 0.1 | 5.0 | -0.6 | KdV | 0.1 | 2.0 | 2.0 | 0.1 | $0.75 \cdots 0.9$ |
| 2 | 0.1 | 0.1 | 0.0 | 0.0 | mKdV | 0.01 | 1.0 | 1.0 | 0.1 | $0.75 \cdots 0.9$ |
| 3 | -0.196 | 0.5 | 0 | 0 | mKdV | 0.05 | 1.0 | 1.0 | 0.1 | $0.75 \cdots 0.9$ |

*Table 5.4* Table of parameters for the three cases considered. Case 1 and 2 are the cases of near uniform horizontal velocity with uniform and non-uniform radial velocity respectively. Case 3 is the jet-like profile with uniform radial velocity.

## 5.4 Large-amplitude inertial solitary waves with vortex cores in a cylindrical channel

In the following, the results for the propagation of large-amplitude inertial solitary waves with vortex cores in a rotating flow are presented. Three specific inflow conditions are of interest, the corresponding parameters are given in Table 5.4.

The horizontal and rotational velocities $u$ and $w$ in the first two cases feature a typical shear in horizontal velocity and strong rotational shear velocity and uniform rotational shear velocity respectively. The third case features a jet-like profile for the horizontal velocity and a uniform rotational velocity. The corresponding solutions are a KdV outer solution in the first case and mKdV outer solutions in the two other cases. The three specific inflow conditions are shown in Figures 5.34, 5.43 and 5.52.

Figures 5.35, 5.44 and 5.53 show plots of the streamfunction at 2/3 of the depth for the three respective cases. Time is normalized with the flow speed and the typical length scale of the wave. Figures 5.36, 5.45, 5.54 and 5.38, 5.47, 5.56 show contour plots of the streamfunction field and an enlarged view of the recirculation region for the three cases respectively for normalized times given in the Figures. Figures 5.37, 5.46, 5.55 and 5.39, 5.48, 5.57 show the corresponding contour plot of the circulation.

All contour plots depict little change of the solutions and the recirculation regions in particular. The recirculation regions remain stagnant to first order.

The solutions given by DG for the three inflow conditions are studied for several amplitudes up to the maximum amplitude, $0.75 \leq \frac{A_{max}-A_*}{\mu_{max}} \leq 0.9$. In addition, the maximum adverse velocity at the axis as well as the maximum amplitude of the solutions versus normalized time are measured.

The results for the maximum adverse velocity are shown in Figures 5.40, 5.49 and 5.58 and for the maximum amplitude in Figures 5.41, 5.50 and 5.59.

It is pertinent to note here that the recirculation region was not set to constant, as in the stratified flow case, since the discontinuity in $\psi_r$ across the vortex boundary caused numerical instability, but it is noted here that since $\psi = 0$ at the axis it is apparent from the close-ups of the recirculation regions that the recirculation regions are yet stagnant to first order.

All results show a nearly linear decrease of adverse velocity inside the recirculation region of order of magnitude less than $O(10^{-5})$, a relative change of less than 1%. In Figures 5.42, 5.51 and 5.60 the phase speeds for the three inflow conditions are depicted together with the final amplitude of the solutions. The final amplitudes in all three cases are very close to the initial amplitudes. Remarkable is the increase in maximum amplitude for the second and third inflow conditions and a decrease for the first case. The relative change in maximum amplitude is less than 0.1% for the two latter cases and 3% for the first case. For the latter two cases the change in amplitude is bounded indicating that an equilibrium solution is to be expected. For the first case, the numerical evidence is not entirely convincing, but considering that the rotation $\Omega_0$ is much larger than in the subsequent cases and noting that the changes are to within the error of the numerical scheme, all results confirm the permanence of the solutions and the stagnancy of the recirculation region in particular.
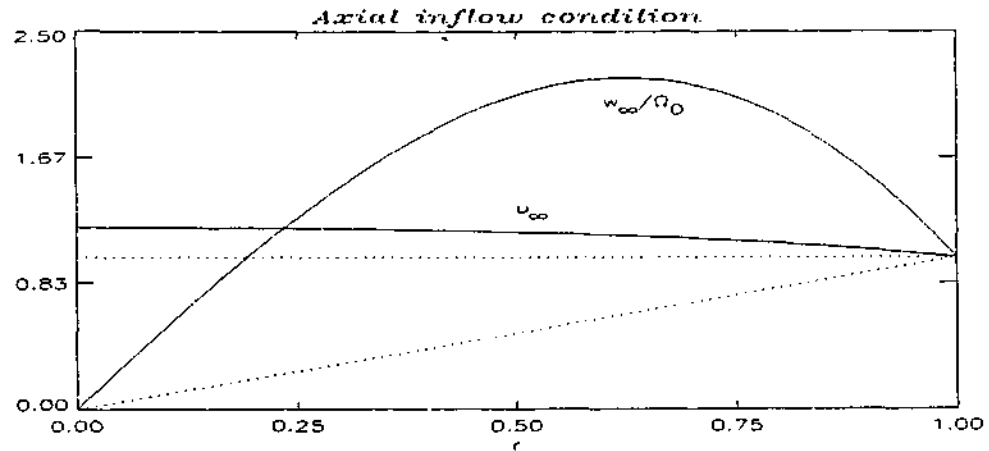
Figure 5.34: Plot of the inflow conditions (solid) for the KdV outer solution ($\alpha_3 = 0$) and the parameters $a_1 = 0.1$, $a_2 = 0.1$, $b_1 = 5.0$, $b_2 = -0.64$, $\epsilon = 0.1$, $\kappa = 2.0$, $\sigma = 2.0$, $R(A_*) = 0.662$, $\mu_{max} = 0.00382$, $\Omega_0 = 0.1$ and $c = 1.058$.
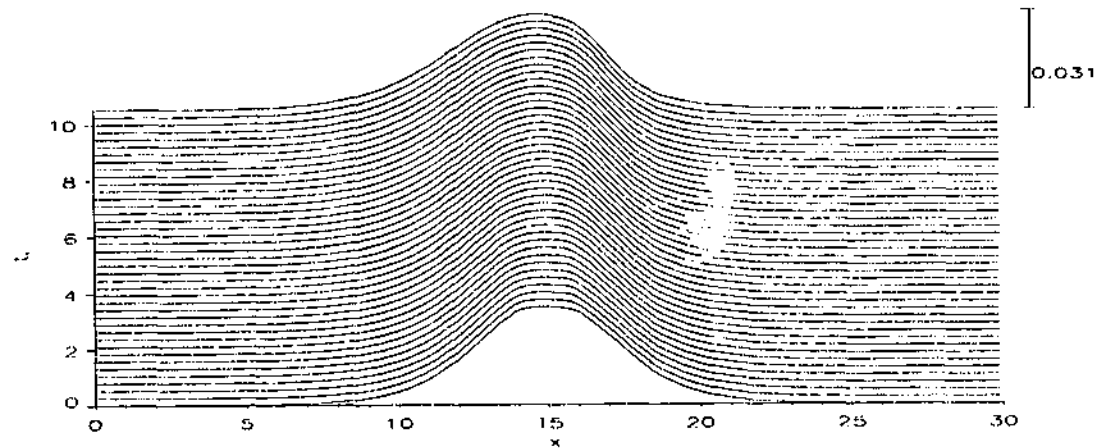


Figure 5.35: Plot of the streamfunction for the KdV outer solution at the depth $\frac{2}{3}a$ for the parameters given in Figure 5.34 and $\mu = 0.75\mu_{max}$.
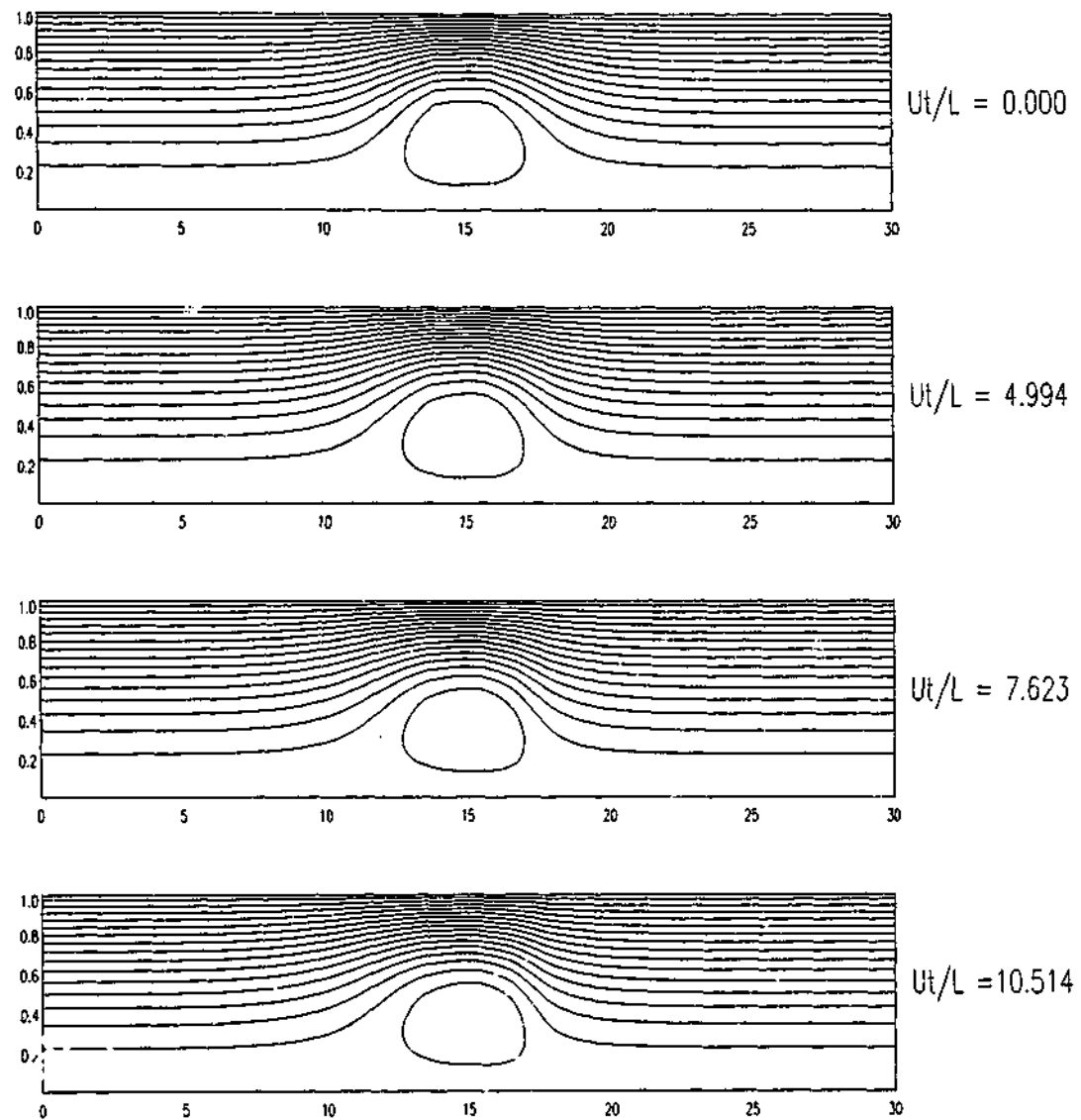
Figure 5.36: Contour of the streamfunction for the KdV outer solution of Figure 5.35 for the normalized times $t_n = 0,5,7.6$ and 10.5. The width of the domain is denoted along the horizontal and the radius along the vertical.
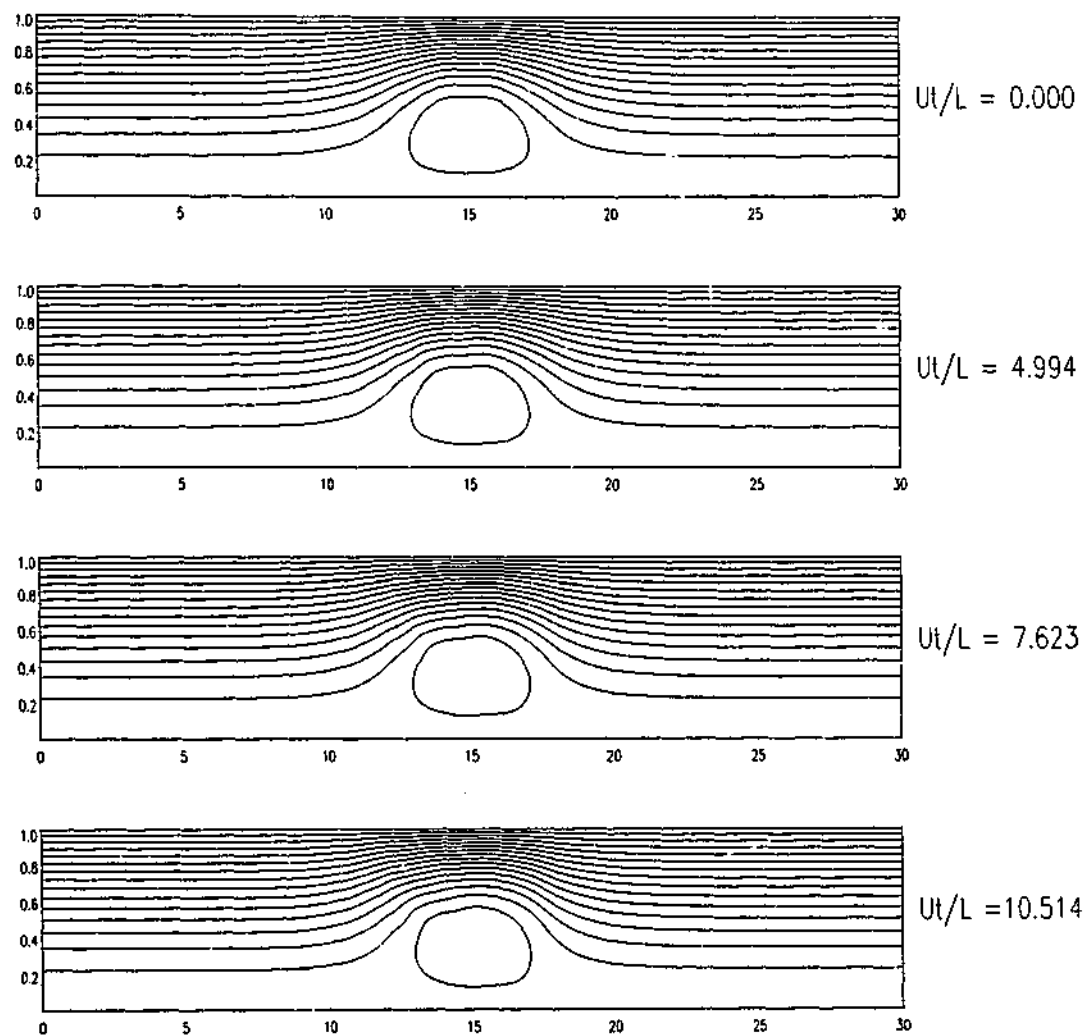
Figure 5.37: Contour of the circulation $C(\psi)$ for the KdV outer solution of Figure 5.35 for the normalized times $t_n = 0,5,7.6$ and 10.5. The width of the domain is denoted along the horizontal and the radius along the vertical.
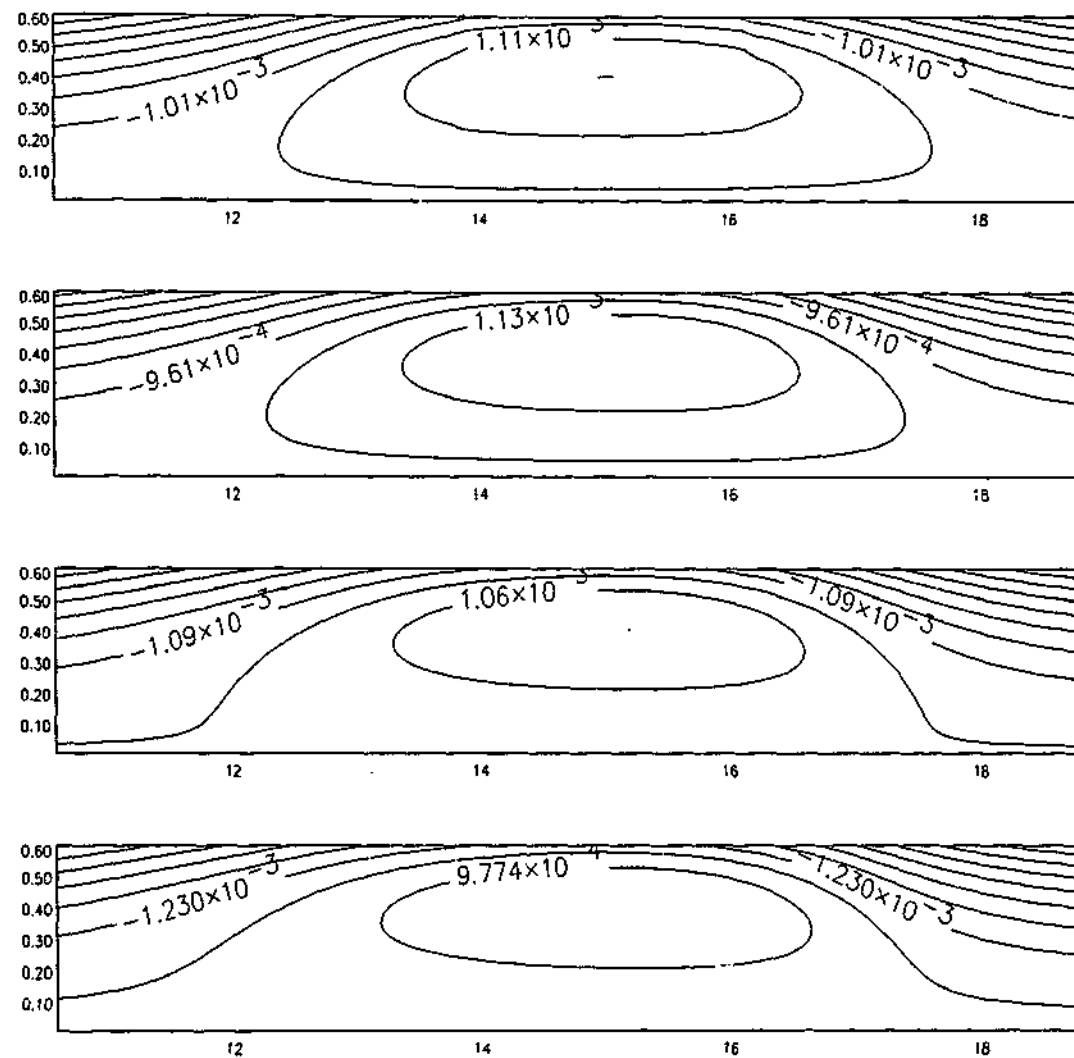
Figure 5.38: Enlargement of the recirculation regions of the streamfunction contour-plot for the KdV outer solution of Figure 5.36. The range is 70x36 points. The width of the domain is denoted along the horizontal and the radial position along the vertical.
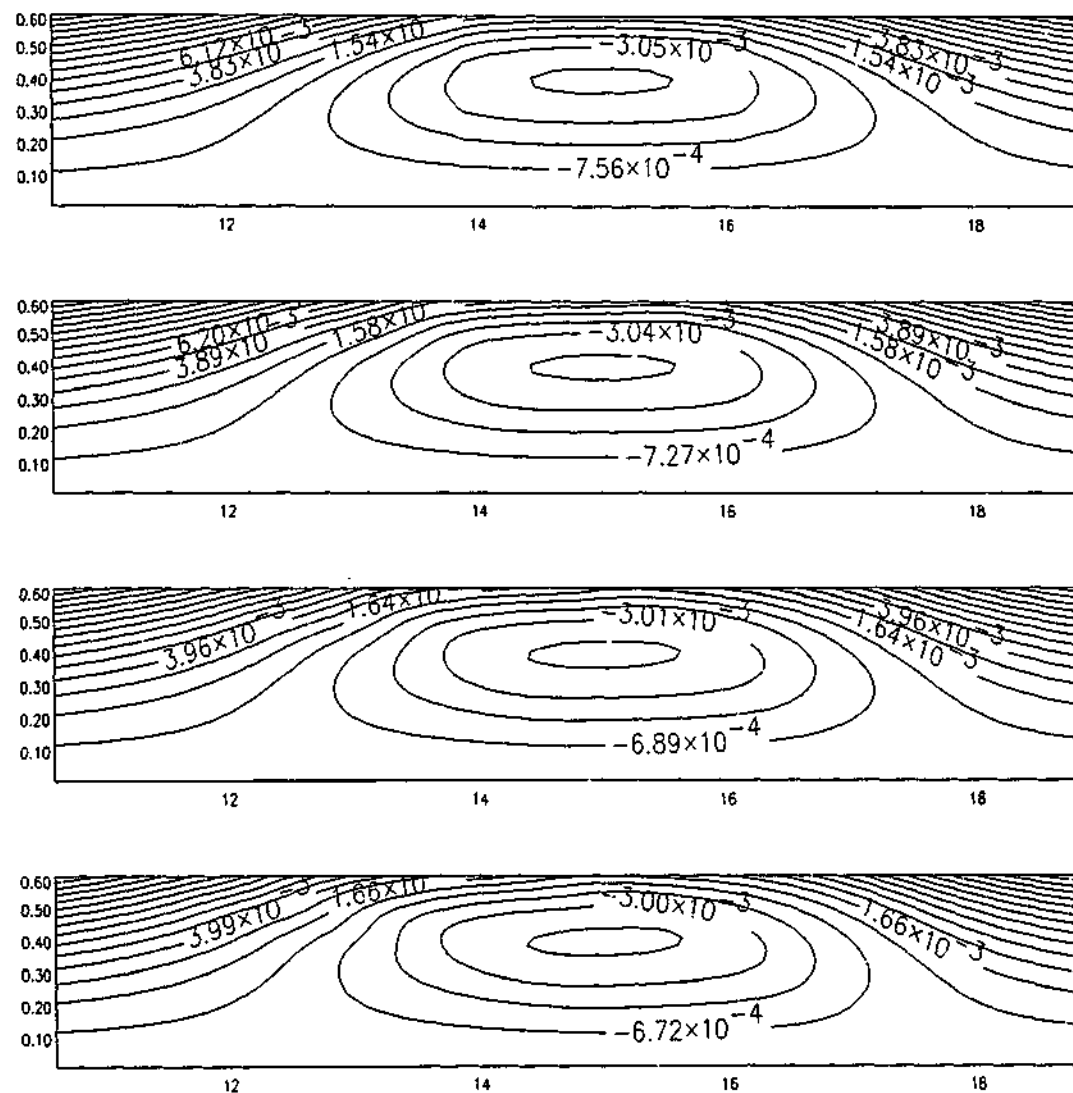
Figure 5.39: Enlargement of the recirculation regions of the circulation contour-plot for the KdV outer solution of Figure 5.37. The range is 70x36 points. The width of the domain is denoted along the horizontal and the radial position along the vertical.
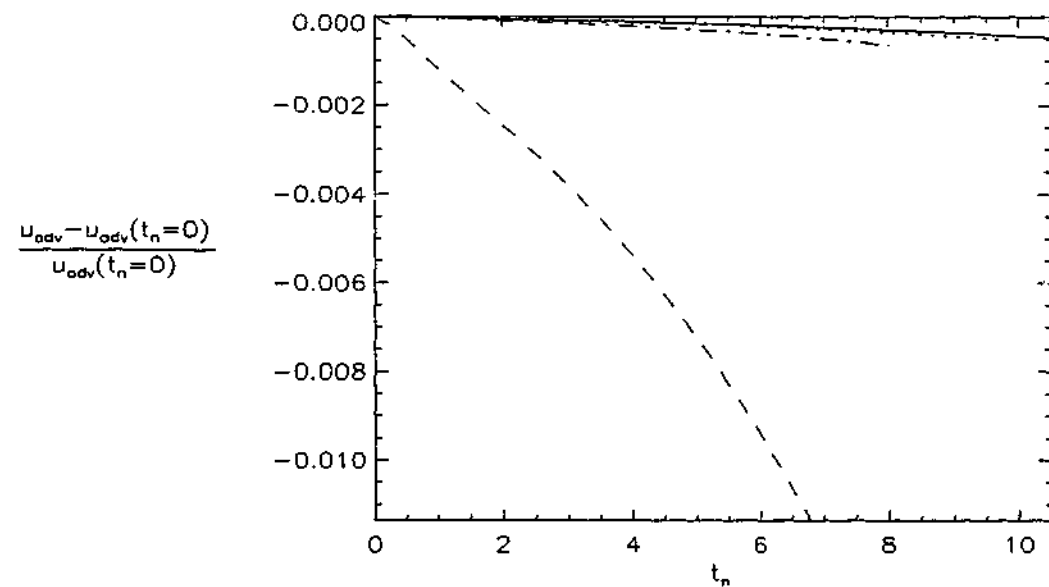
$$\frac{u_{adv} - u_{adv}(t_n = 0)}{u_{adv}(t_n = 0)}$$

Figure 5.40: Plot of the maximum adverse velocity $u_{adv}$ relative to the initial value $u_{adv}(t_n = 0)$ at the axis versus normalized time $t_n$ for the KdV outer solution and the parameters given in Figure 5.34 and $\mu = 0.75\mu_{max}$ (solid), $0.80\mu_{max}$ (dotted), $0.85\mu_{max}$ (dashed) and $0.9\mu_{max}$ (dash-dot).



$$\frac{A_{max} - A_{max}(t_n = 0)}{A_{max}(t_n = 0)}$$

Figure 5.41: Plot of the maximum amplitude $A_{max}$ relative to the initial value $A_{max}(t_n = 0)$ versus normalized time $t_n$ for the KdV outer solution and the parameters given in Figure 5.34 and $\mu = 0.75\mu_{max}$ (solid), $0.80\mu_{max}$ (dotted), $0.85\mu_{max}$ (dashed) and $0.9\mu_{max}$ (dash-dot).
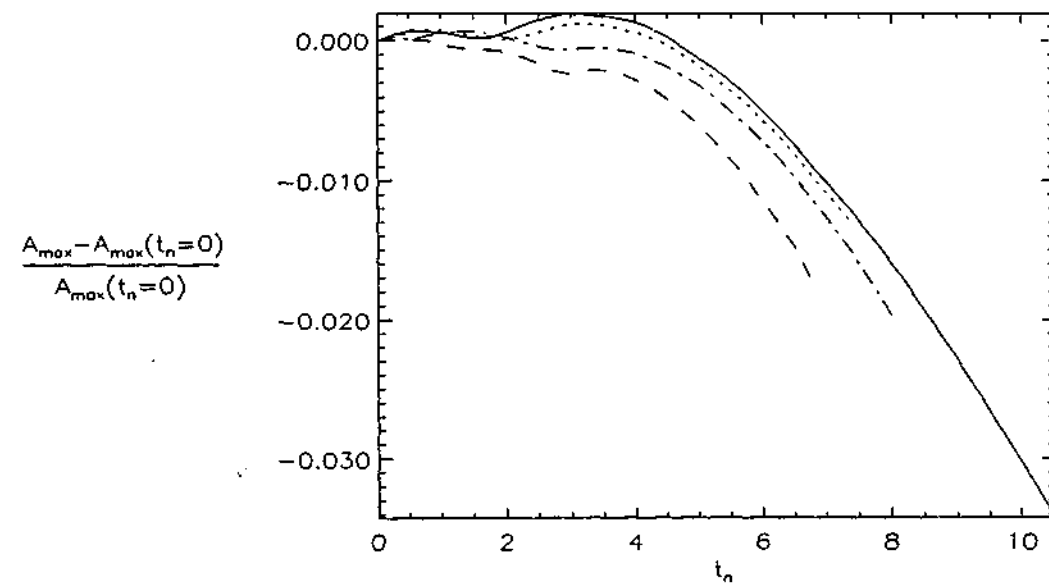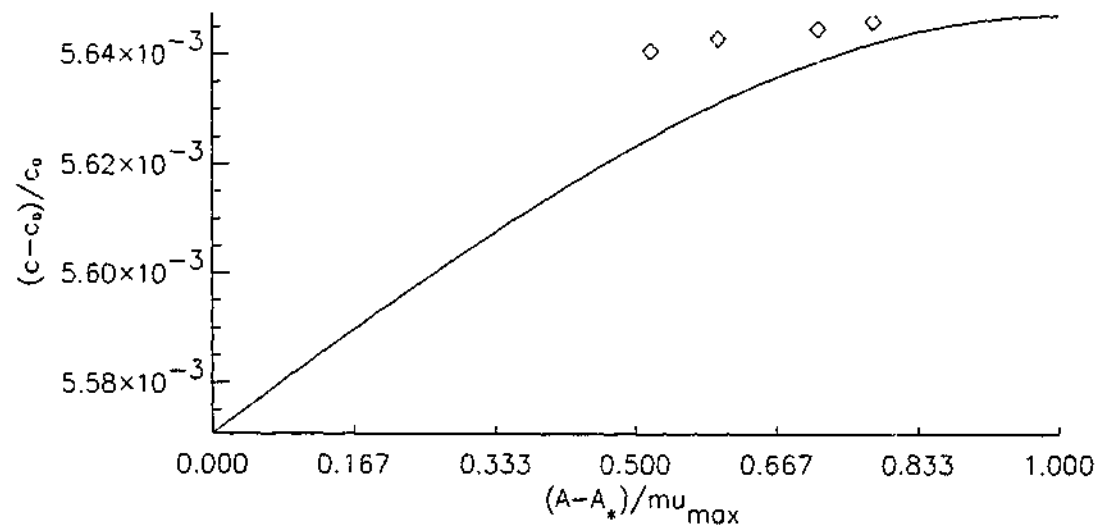
Figure 5.42: Plot of the theoretical phase speed versus Amplitude for the KdV outer solution and the parameters given in Figure 5.34. Diamonds denote the results for several normalized amplitudes $0.75 \leq (A - A_*)/\mu_{max} \leq 0.9$, ie. $(.75, .8, .85, .9)$.
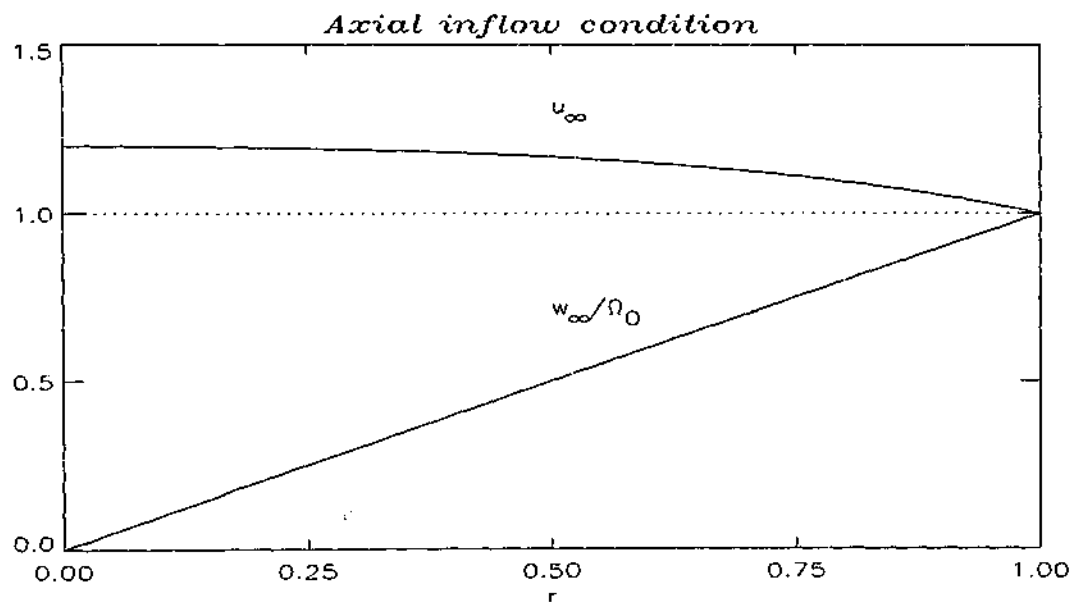


Figure 5.43: Plot of the inflow conditions (solid) for the mKdV outer solution $(\alpha_3 \neq 0)$ and the parameters $a_1 = 0.1$, $a_2 = 0.1$, $b_1 = 0.0$, $b_2 = 0.0$, $\epsilon = 0.1$, $\kappa = 1.0$, $\sigma = 1.0$, $R(A_*) = 0.15853$, $\mu_{max} = 0.000419$, $\Omega_0 = 0.01$ and $c = 1.007$.
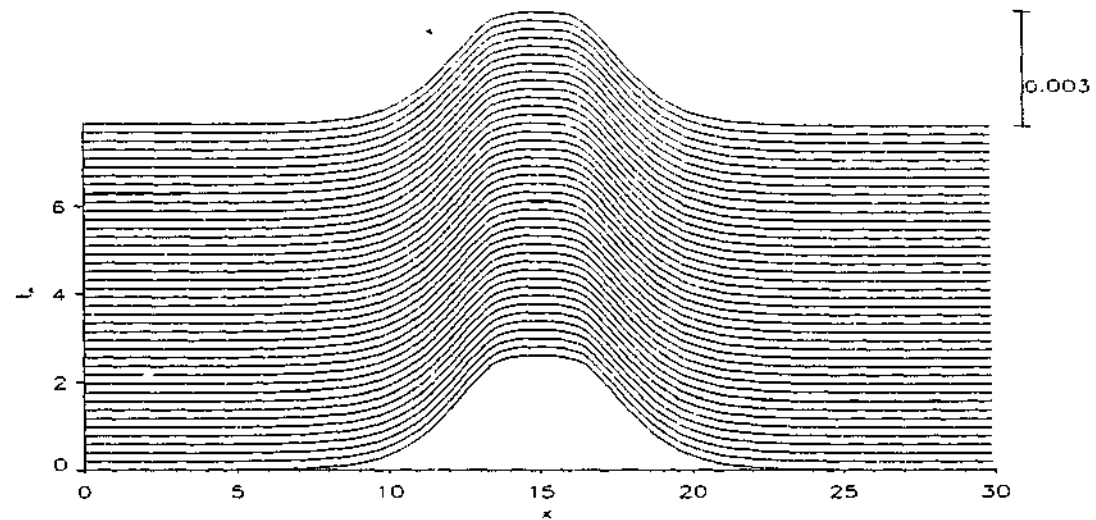
Figure 5.44: Plot of the streamfunction for the mKdV outer solution at the depth $\frac{2}{3}a$ for the parameters given in Figure 5.43 and $mu = 0.9\mu_{max}$.



Figure 5.45: Contour of the streamfunction for the mKdV outer solution of Figure 5.44 for the normalized times $t_n = 0, 3.7, 5.7$ and $7.9$. The width of the domain is denoted along the horizontal and the radius along the vertical.
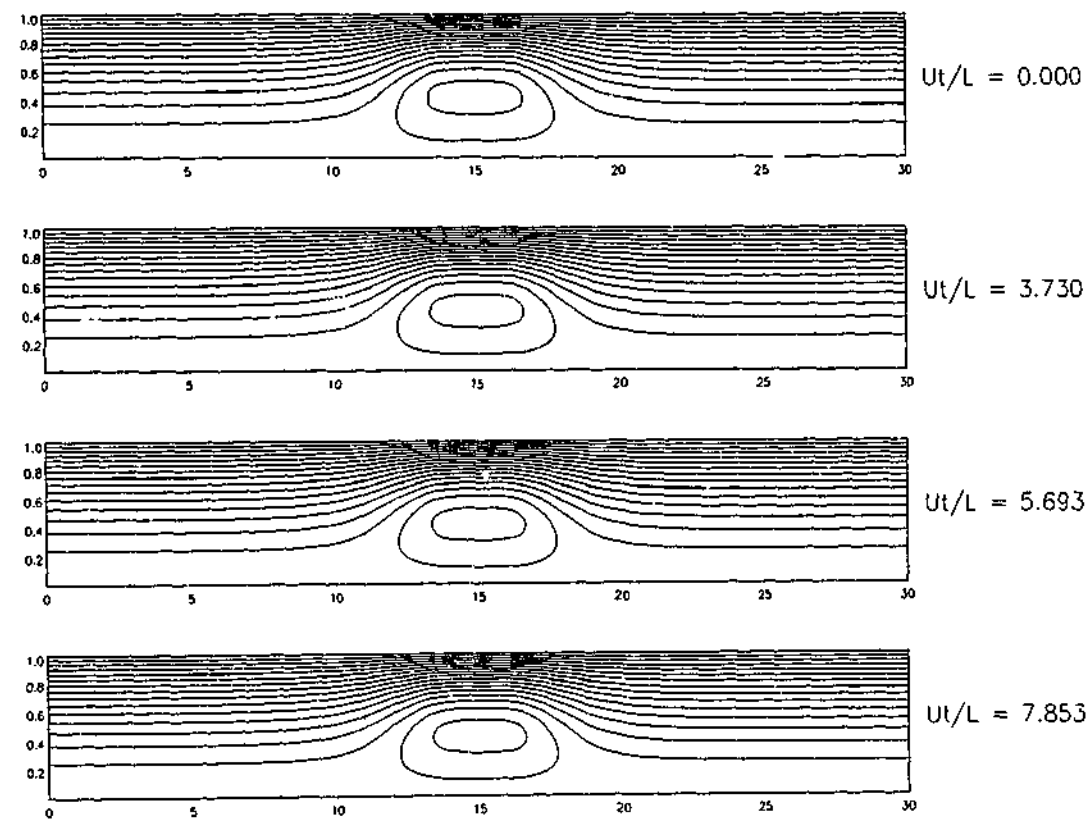
Figure 5.46: Contour of the circulation $C(\psi)$ for the mKdV outer solution of Figure 5.44 for the normalized times $t_n = 0,3.7,5.7$ and $7.9$. The width of the domain is denoted along the horizontal and the radius along the vertical.

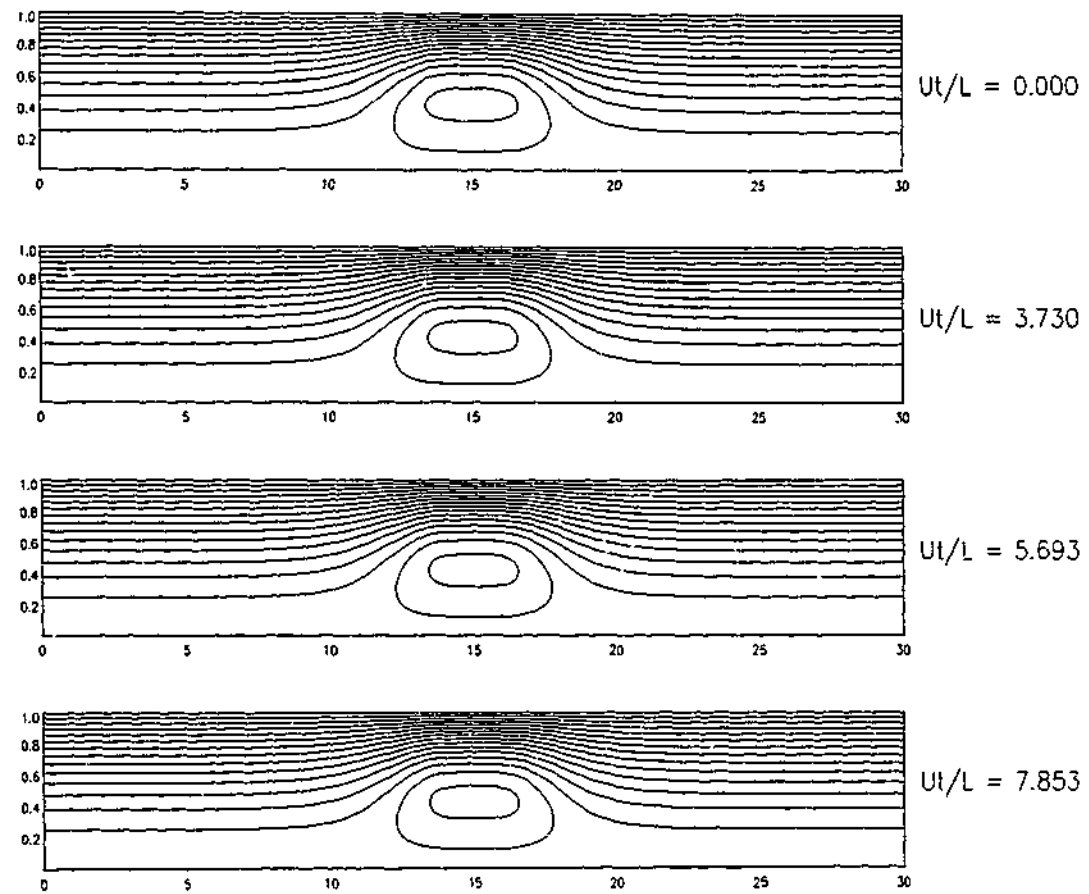Figure 5.47: Enlargement of the recirculation regions of the streamfunction contour-plot for the mKdV outer solution of Figure 5.45. The range is 70x36 points. The width of the domain is denoted along the horizontal and the radial position along the vertical.
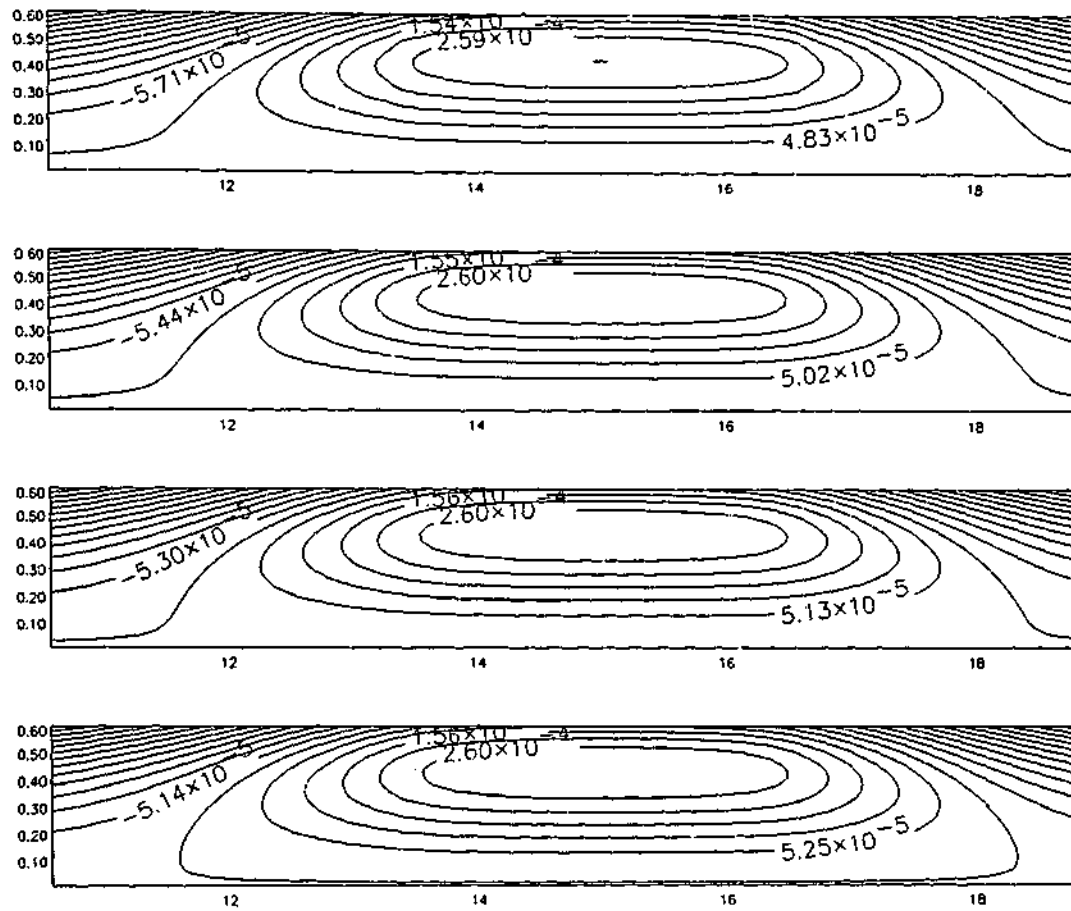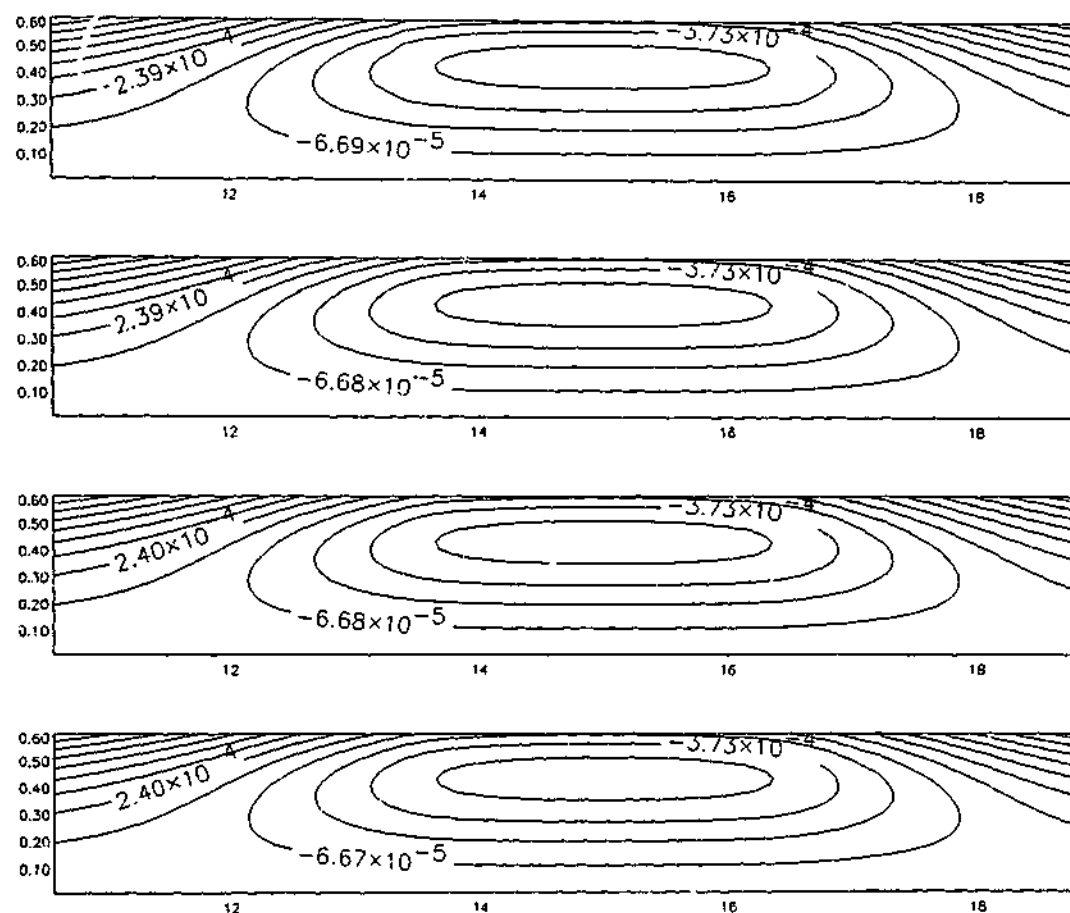
Figure 5.48: Enlargement of the recirculation regions of the circulation contour-plot for the mKdV outer solution of Figure 5.46. The range is 70x36 points. The width of the domain is denoted along the horizontal and the radial position along the vertical.
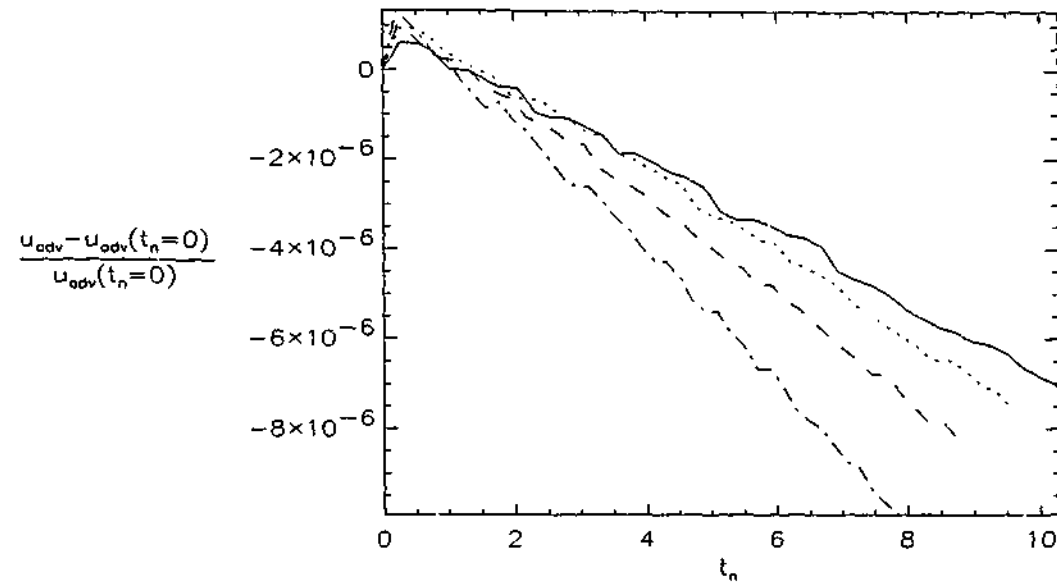
Figure 5.49: Plot of the maximum adverse velocity $u_{adv}$ relative to the initial value $u_{adv}(t_n = 0)$ at the axis versus normalized time $t_n$ for the mKdV outer solution and the parameters given in Figure 5.44 and $\mu = 0.75\mu_{max}$ (solid), $0.80\mu_{max}$ (dotted), $0.85\mu_{max}$ (dashed) and $0.9\mu_{max}$ (dash-dot).
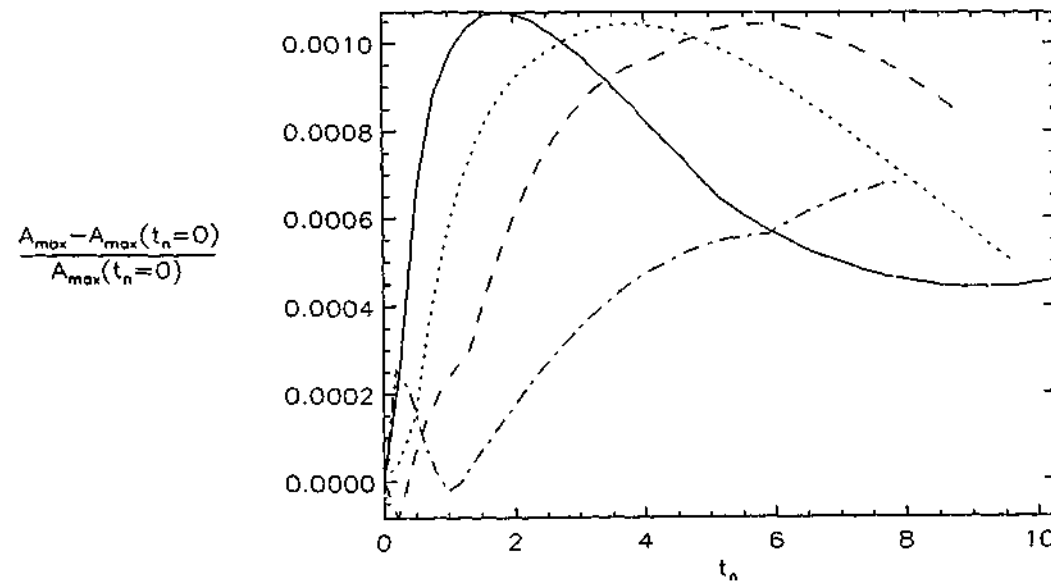


Figure 5.50: Plot of the maximum amplitude $A_{max}$ relative to the initial value $A_{max}(t_n = 0)$ versus normalized time $t_n$ for the mKdV outer solution and the parameters given in Figure 5.44 and $\mu = 0.75\mu_{max}$ (solid), $0.80\mu_{max}$ (dotted), $0.85\mu_{max}$ (dashed) and $0.9\mu_{max}$ (dash-dot).
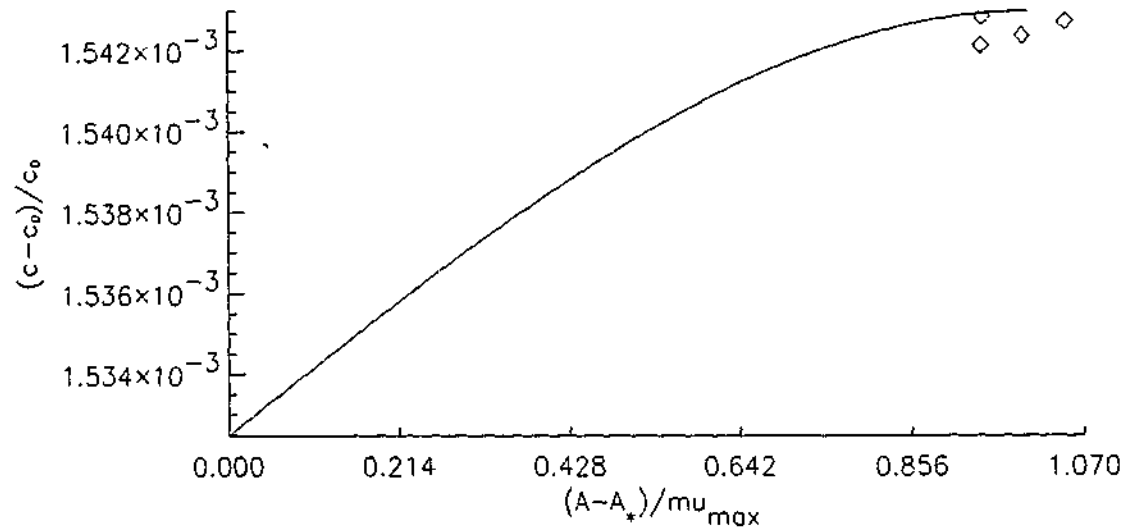
Figure 5.51: Plot of the theoretical phase speed versus Amplitude for the mKdV outer solution and the parameters given in Figure 5.43. Diamonds denote the results for several normalized amplitudes $0.75 \leq (A - A_*)/\mu_{max} \leq 0.9$, ie. $(.75, .8, .85, .9)$.
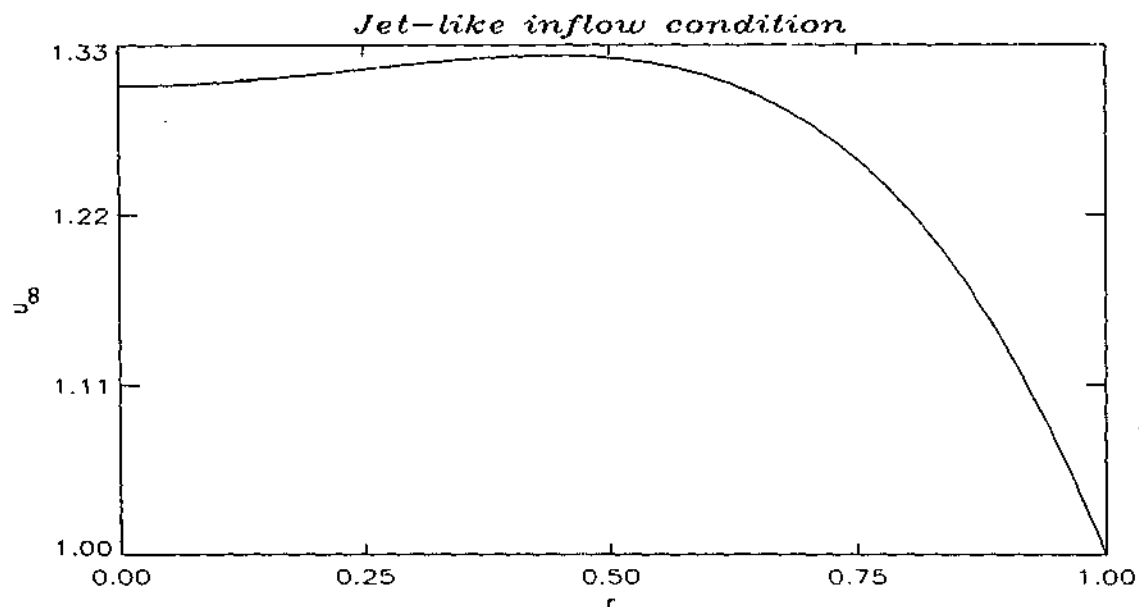


Figure 5.52: Plot of the inflow horizontal velocity condition (solid) for the mKdV outer solution with uniform axial velocity, $(\alpha_3 \neq 0)$ and the parameters $a_1 = -0.196$, $a_2 = 0.5$, $b_1 = 0.0$, $b_2 = 0.0$, $\epsilon = 0.1$, $\kappa = 1.0$, $\sigma = 1.0$, $R(A_*) = 0.0612$, $\mu_{max} = .000184$, $\Omega_0 = 0.005$ and $c = 1.0052$.
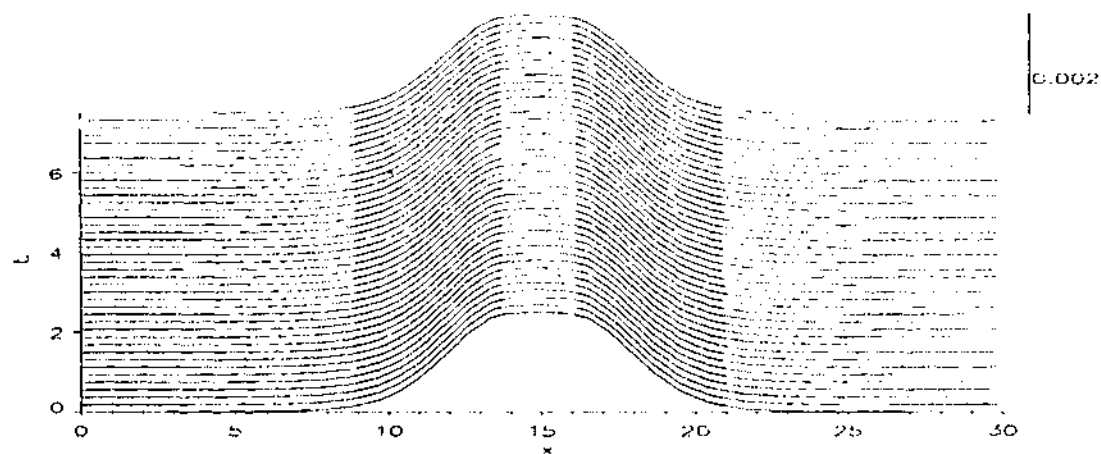
Figure 5.53: Plot of the streamfunction for the mKdV outer solution at the depth $\frac{2}{3}a$ for the parameters given in Figure 5.52 and $mu = 0.9\mu_{max}$.
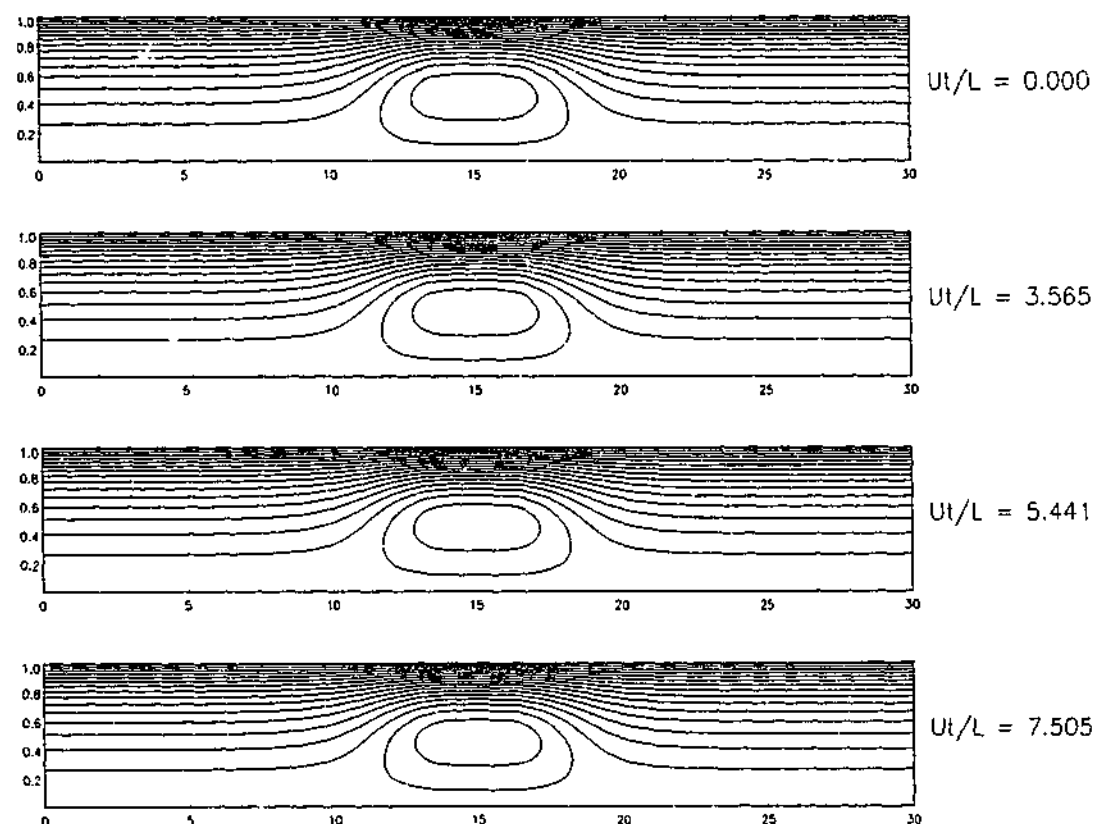


Figure 5.54: Contour of the streamfunction for the mKdV outer solution of Figure 5.53 for the normalized times $t_n = 0, 3.6, 5.4$ and $7.5$. The width of the domain is denoted along the horizontal and the radius along the vertical.
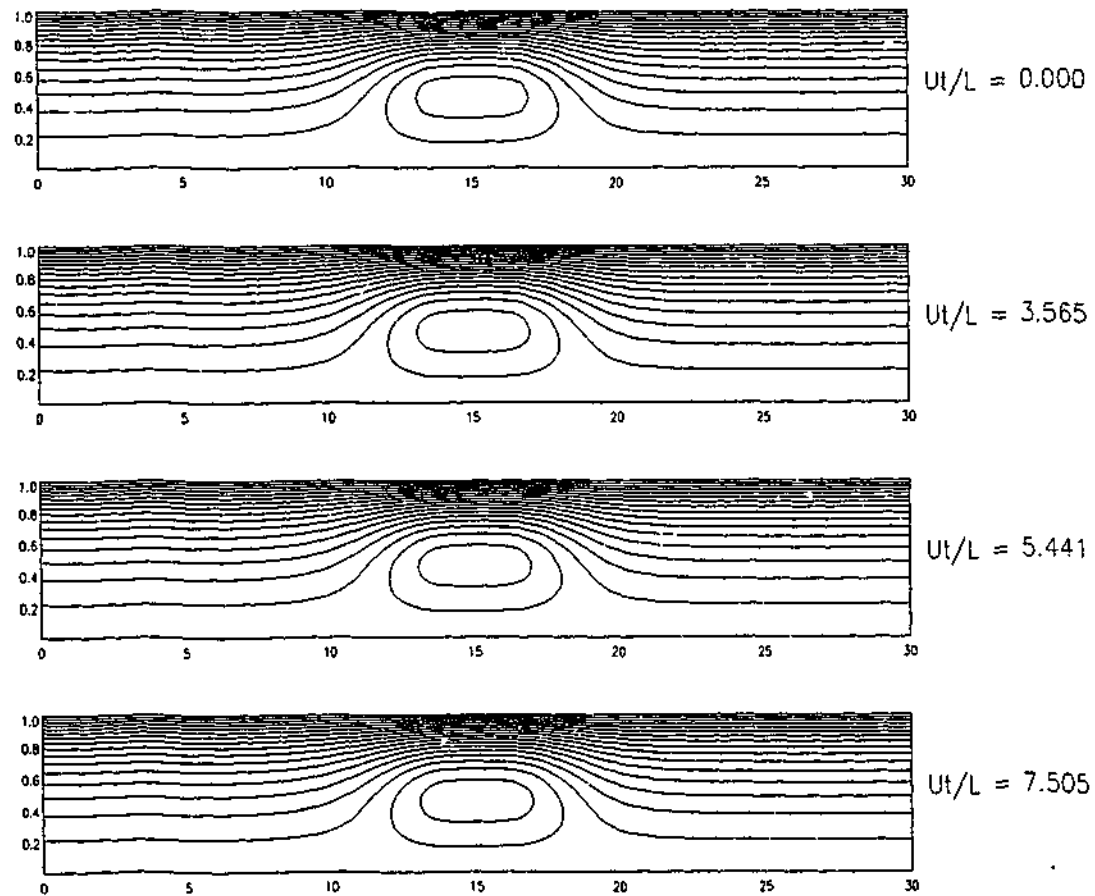
Figure 5.55: Contour of the circulation $C(\psi)$ for the mKdV outer solution of Figure 5.53 for the normalized times $t_n = 0,3.6,5.4$ and $7.5$. The width of the domain is denoted along the horizontal and the radius along the vertical.
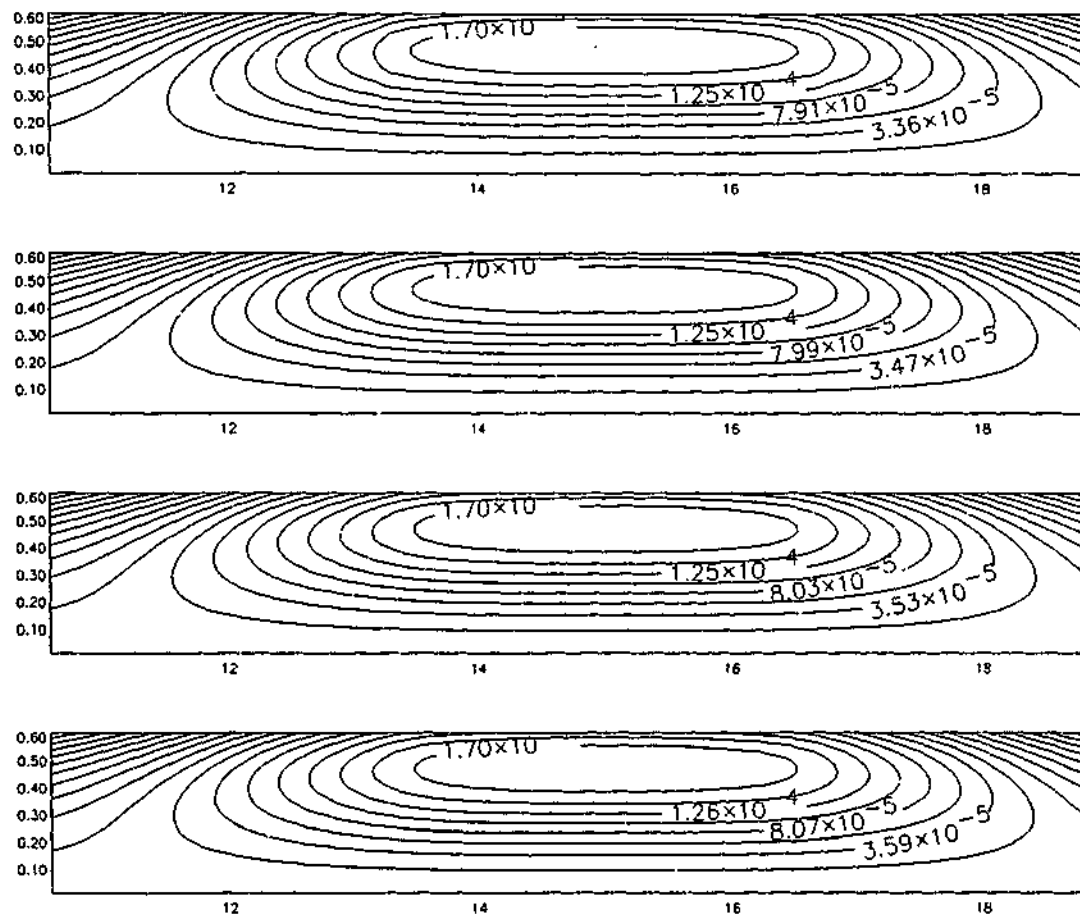
Figure 5.56: Enlargement of the recirculation regions of the streamfunction contour-plot for the mKdV outer solution of Figure 5.54. The range is 70x36 points. The width of the domain is denoted along the horizontal and the radial position along the vertical.
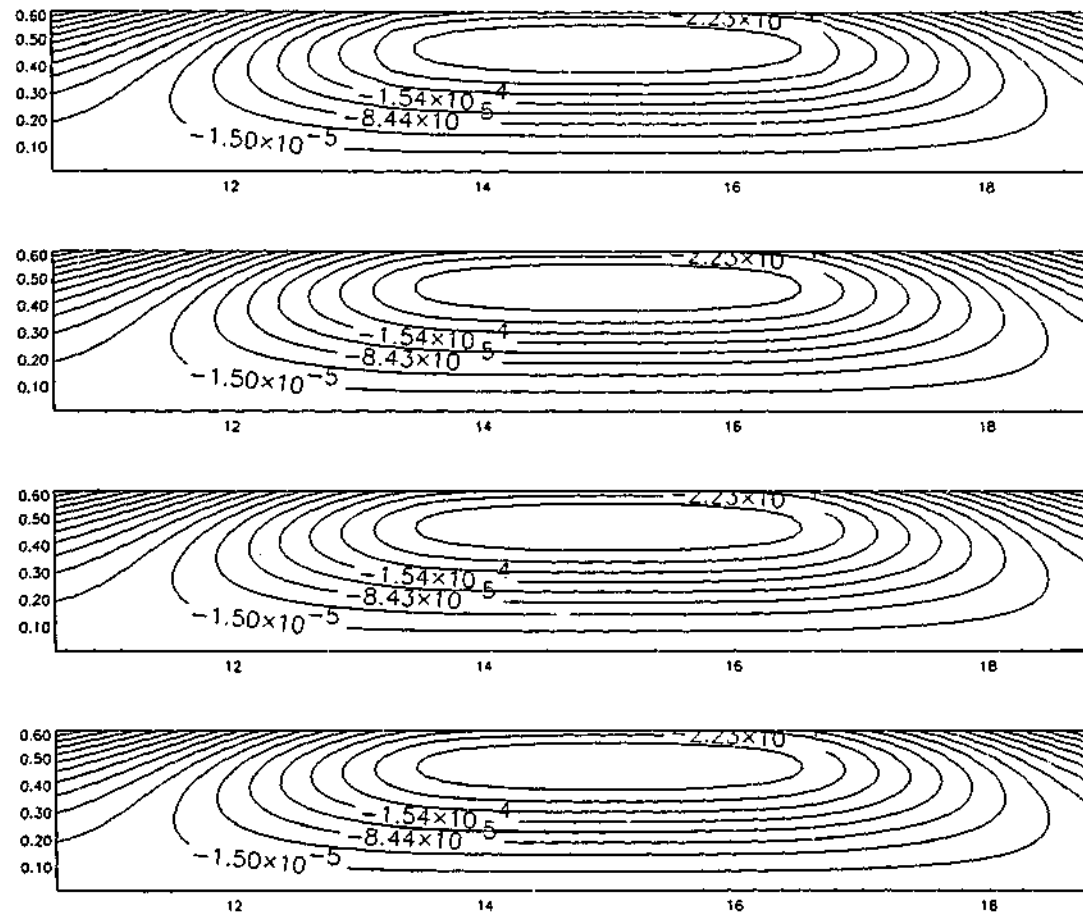
Figure 5.57: Enlargement of the recirculation regions of the circulation contour-plot for the mKdV outer solution of Figure 5.55. The range is 70x36 points. The width of the domain is denoted along the horizontal and the radial position along the vertical.
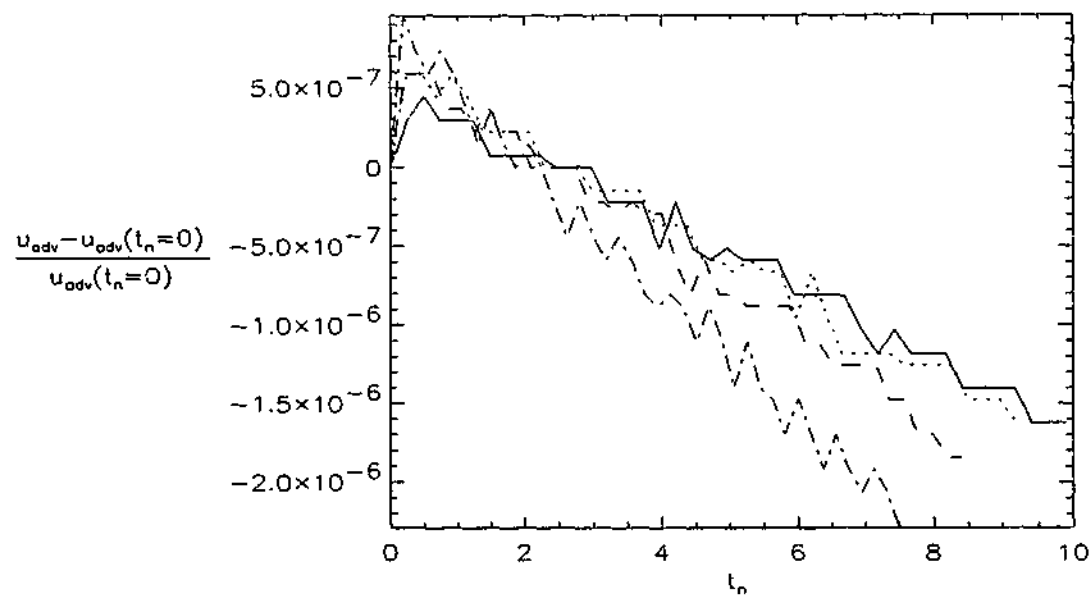
Figure 5.58: Plot of the maximum adverse velocity $u_{adv}$ relative to the initial value $u_{adv}(t_n = 0)$ at the axis versus normalized time $t_n$ for the mKdV outer solution and the parameters given in Figure 5.53 and $\mu = 0.75\mu_{max}$ (solid), $0.80\mu_{max}$ (dotted), $0.85\mu_{max}$ (dashed) and $0.9\mu_{max}$ (dash-dot).
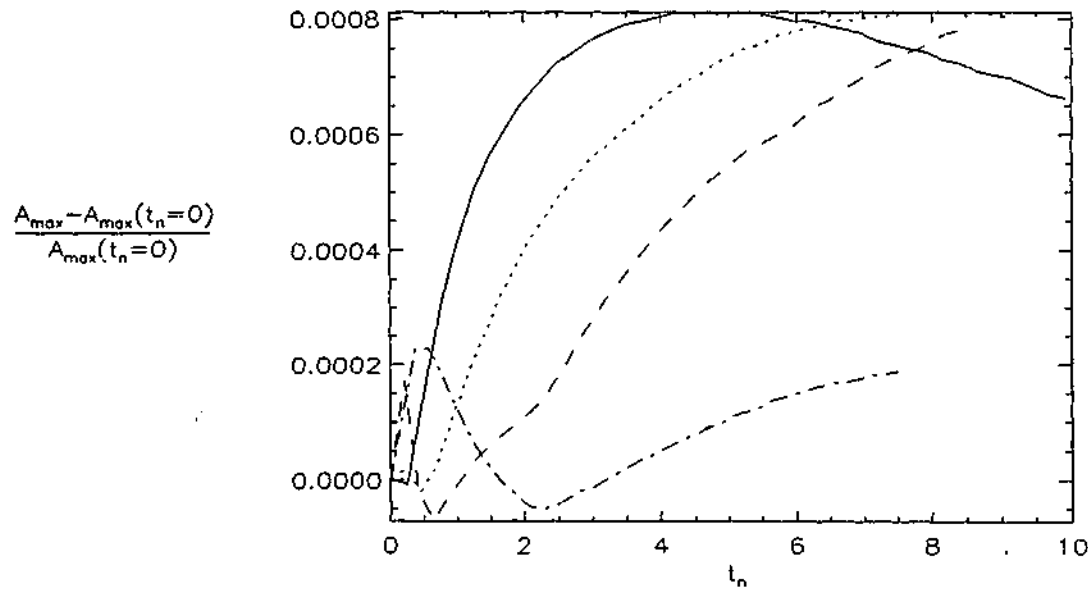


Figure 5.59: Plot of the maximum amplitude $A_{max}$ relative to the initial value $A_{max}(t_n = 0)$ versus normalized time $t_n$ for the mKdV outer solution and the parameters given in Figure 5.53 and $\mu = 0.75\mu_{max}$ (solid), $0.80\mu_{max}$ (dotted), $0.85\mu_{max}$ (dashed) and $0.9\mu_{max}$ (dash-dot).
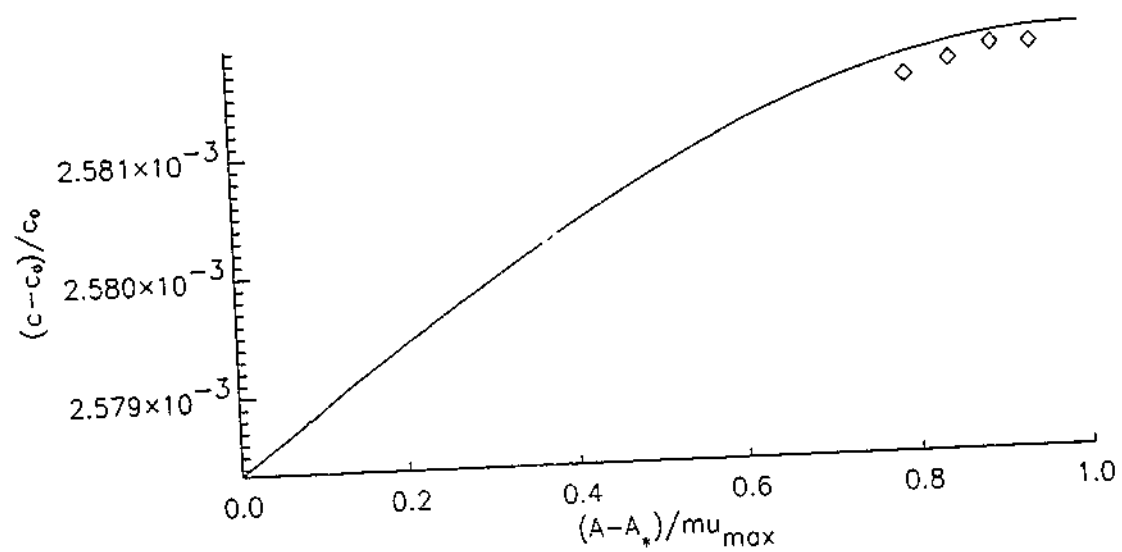
Figure 5.60: Plot of the theoretical phase speed versus Amplitude for the mKdV outer solution and the parameters given in Figure 5.52. Diamonds denote the results for several normalized amplitudes $0.75 \leq (A - A_*)/\mu_{max} \leq 0.9$, ie. $(.75, .8, .85, .9)$.

# Chapter 6

# Conclusion

The main purpose of this study was to show the permanence and validity of the asymptotic theory developed by Derzho and Grimshaw for large-amplitude solitary waves with vortex cores in a stratified fluid [16] and a rotating flow through a cylindrical channel [15]. For this purpose two novel numerical methods have been proposed for the fully nonlinear governing equations of stratified flow and the governing equations of rotating flow. The numerical methods are described in chapter 4. In addition, the numerical model for stratified flow was utilized to verify the finite-amplitude long-wave equation derived by Grimshaw and Yi (1991) [32] for the generation of internal solitary-like waves by flow over topography, as well as the study of multi-scaled internal solitary waves derived by Derzho and Velarde (1995) [17]. In particular, the fully-nonlinear numerical model for stratified flow has been compared to the results of the numerical model of the finite-amplitude long-wave equation by Rottman et al (1996) [58].

Both numerical models developed used extremely accurate pseudospectral methods to model the two-dimensional time-dependent governing equations. Fourier modes in the horizontal and Chebyshev modes in the vertical have been employed for the spatial integration and third order low-storage Runge-Kutta methods, combined with a Liouville-Neumann integration in time for stratified flow for the temporal integration. To solve the two-dimensional elliptic partial differential equation for the rotating flow, a novel direct method was derived and combined with a minimum residual method.

Section 5.1 presented the results for large-amplitude internal solitary waves with vortex cores in the Boussinesq approximation and including the non-Boussinesq terms.

The large-amplitude internal solitary waves in the weakly stratified shallow fluid proved to be stable and of permanent shape. The solutions possessed the characteristics of large amplitude solitary waves. The width increases with amplitude and the phase speed depends nonlinearly on the amplitude (since $\mu = A - A_*$). The width of the solutions tends to infinity for the maximum possible amplitude ($\mu \to \mu_{max}$), indicating the termination of this asymptotic theory. The results show that solitary waves with an essentially homogeneous vortex core exist in a Boussinesq as well as fully-nonlinear fluid. In addition, the results indicate that there is a non-vanishing adverse velocity at the top boundary. The amplitude equation is in both cases governed by a slightly more nonlinear equation, which can be approximated by the nonlinear equation given by Derzho and Grimshaw (1997) [16] .

The recent laboratory experiments by Stamp and Jacka (1995) [60] of solitary waves with vortex cores, which were generated by displacing a large mass of fluid along a very thin thermocline, generally support the theoretical and numerical results presented here, but seem to show that the recirculation region is not stagnant to first order. The numerical simulation by Terez and Knio (1998) [65] of the gravitational collapse of a mixed region along a thermocline produced similar solitary waves with vortex cores of diminishing mass, which is in better agreement with the results presented here.

In section 5.2 results for the generation of solitary-like waves by uniformly stratified flow over isolated bottom topography have been presented for a range of parameters. The results indicate that the theory developed by Grimshaw and Yi (1991) [32] agrees very well with the fully nonlinear spectral model proposed here. The amplitude growth and the drag on the obstacle are in very good agreement with the numerical model of the finite-amplitude long-wave equation by Rottman *et al* (1996) [58] . The agreement between the spectral model proposed here and the FALW model allows the conclusion that, to within the error of the computation, the proposed numerical scheme models the fully nonlinear, inviscid, two-dimensional time-dependent governing equations very well.

In section 5.3 multi-scaled internal solitary waves were presented that exist due

to a balance between nonlinearity and dispersion different to the common KdV type balance. Multi-scaled internal solitary waves resemble bores with smaller-scale solitary waves situated on top. The results presented here show that such waves are of permanent shape and thus validate the theory derived by Derzho and Velarde (1995) [17].

In section 5.4 results for large-amplitude inertial solitary waves with vortex cores derived by Derzho and Grimshaw [15] in an axially-symmetric rotating, incompressible, inviscid fluid of constant density in a cylindrical channel have been presented. As was the case for the stratified flow the purpose was to show the permanence of such solitary waves for a range of outer solutions and inflow conditions, by studying their longtime behaviour as well as maximum adverse velocity at the axis and maximum amplitude. The results indicate that the solutions are of permanent shape and that the recirculation region remains stagnant to first order to within the accuracy of the scheme.

The results presented here reveal the relevance of large-amplitude solitary waves with vortex cores in stratified and rotating flows for a whole class of flows and possible analogues in various other naturally occurring and engineering flows. The verification of the asymptotic theory by Derzho and Grimshaw (1997) [16, 15] has proven the permanence of such waves and in particular the stagnancy of the recirculation region. It is important to note here that the solutions represent steady-state solutions to be expected in corresponding tank experiments for very large times. But since corresponding laboratory experiments for extremely large times are usually not feasible, such results can only give an impression for the near steady-state of the flow. This explains why in most laboratory experiments large-amplitude solitary waves seem to possess a significantly strong recirculation region. In addition to the advantage of steady-state results the quantitative results provided here are otherwise not obtainable and are thus valuable for future applications. Furthermore results presented for the generation of solitary-like waves by uniformly stratified flow over bottom topography validates the asymptotic theory developed by Grimshaw and Yi (1991) [32] and complements the numerical results for the equations in the Boussinesq approximation by Rottman *et al*(1996) [58]. The results for multi-scaled internal solitary waves derived by Derzho and Velarde (1995) [17]

show the validity of their asymptotic theory and permanence of the bore-like solutions.

Finally it remains to be emphasized that the wide variety of applications studied here reveal the excellent numerical accuracy, consistency and adaptability of spectral methods for modelling stratified flow in a channel and constant density rotating flow through a cylindrical channel.

# Appendix

The parameters $\alpha_n$ ($n = 1, 2, 3$) of equation (3.109) are given by the following equations

$$\alpha_1 = \frac{2\hat{\kappa}}{(1 - c^{(0)})}(a_1(-g_3 + g_6) + a_2(-g_1 + g_6 - \frac{g_7}{\lambda^{(0)2}})) + \cdots$$
$$+ \hat{\sigma}(b_1(3g_3 - 2g_6) + b_2(-2g_6 + 4g_1)),$$

$$\alpha_2 = \frac{3\hat{\kappa}}{(1 - c^{(0)})^2}(-a_2g_2 - \frac{1}{2}a_1g_5) + \frac{\hat{\sigma}}{(1 - c^{(0)})}(3b_1g_5 + 8b_2g_2),$$

$$\alpha_3 = \frac{4g_4}{(1 - c^{(0)})^2}(\hat{\sigma}b_2 - \frac{1}{3}\frac{\hat{\kappa}a_2}{(1 - c^{(0)})}).$$

The factor in equation (3.109) equates to

$$\frac{I}{\lambda^{(0)2}} = \frac{1}{2}\frac{J_0(\lambda^{(0)})^2}{\lambda^{(0)2}} = 181.02.$$

The $g_n$'s ($n = 1, \cdots, 7$) in the equations for $\alpha_n$ are given by the Integrals

$$g_1 = \int_0^1 \frac{W(\xi)}{2\xi}\xi^{5/2}J_1(\lambda^{(0)}\sqrt{\xi})d\xi = 0.011802,$$

$$g_2 = \int_0^1 \frac{W(\xi)}{2\xi}\xi^2 J_1(\lambda^{(0)}\sqrt{\xi})^2 d\xi = 0.007496,$$

$$g_3 = \int_0^1 \frac{W(\xi)}{2\xi}\xi^{3/2}J_1(\lambda^{(0)}\sqrt{\xi})d\xi = 0.027035,$$

$$g_4 = \int_0^1 \frac{W(\xi)}{2\xi}\xi^{3/2}J_1(\lambda^{(0)}\sqrt{\xi})^3 d\xi = 0.005976,$$

$$g_5 = \int_0^1 \frac{W(\xi)}{2\xi}\xi J_1(\lambda^{(0)}\sqrt{(\xi)})^2 d\xi = 0.021309,$$

$$g_6 = \int_0^1 \frac{W(\xi)}{2\xi}\sqrt{\xi}J_1(\lambda^{(0)}\sqrt{\xi})d\xi = 0.081107,$$

$$g_7 = \int_0^1 2W(\xi)\sqrt{\xi}J_1(\lambda^{(0)}\sqrt{\xi})d\xi = 0.108143.$$

where

$$W(\xi) = \sqrt{\xi}J_1(\lambda^{(0)}\sqrt{\xi}).$$

106

# Bibliography

[1] A. Aigner, D. Broutman, and R. Grimshaw, *Numerical simulations of internal solitary waves with vortex cores*, Fluid Dyn. Res. **25** (1999), 315–333.

[2] T. B. Benjamin, *The stability of solitary waves*, Proc. R. Soc. Lond., Ser. A **328** (1972), 153–183.

[3] _____, *Theory of the vortex breakdown phenomenon*, J. Fluid Mechanics **14** (1978), 593–629.

[4] _____, *A new kind of solitary wave*, J. Fluid Mechanics **245** (1992), 401–403.

[5] D. J. Benney and D. R. S. Ko, *The propaga'ion of long large amplitude internal waves*, Stud. in Appl. Math. **59** (1978), 187–199.

[6] J. Bona, *On the stability theory of solitary waves*, Proc. R. Soc. Lond., Ser. A **344** (1975), 363–374.

[7] J. L. Bona, P. E. Souganidis, and W. A. Strauss, *Stability and instability of solitary waves of KdV type*, Proc. R. Soc. London Ser. A **411** (1987), 395–412.

[8] J. P. Boyd, *Chebyshev and Fourier Spectral Methods*, Springer-Verlag, Berlin, 1989.

[9] S. L. Bragg and W. R. Hawthorne, *Some exact solutions of the flow through annular cascade actuator discs*, J. Aeron. Sci. **17** (1950), 243–249.

[10] A. Brandt and S. R. Fulton, *Improved spectral multigrid methods for periodic elliptic problems*, J. Comp. Phys. **58** (1985), 96–112.

[11] D. J. Brown and D. R. Christie, *Fully nonlinear solitary waves in continuously stratified incompressible Boussinesq fluids*, Phys. Fluids **10** (1998), no. 10, 2569–2586.

[12] C. Canuto, M. Y. Hussaini, A. Quarteroni, and T. A. Zang, *Spectral methods in fluid dynamics*, Springer Series in Computational Physics, Springer, 1988.

[13] L. Collatz, *The numerical treatment of differential equations*, 3rd ed. ed., Springer Verlag, 1960, p.36 ff.

[14] A. Defant, *Über interne Wellen, besonders solche mit Gezeitencharakter*, Deutsche Hydro. Zeit. **5** (1952), no. 5/6, 231–245.

[15] O. Derzho and R. Grimshaw, *Solitary waves with recirculation zones in axisymmetric rotating flows*, J. Fluid Mechanics, sub judice.

[16] O. G. Derzho and R. Grimshaw, *Solitary waves with a vortex core in a shallow layer of stratified fluid*, Phys. Fluids **9** (1997), no. 11, 3378–3385.

[17] O. G. Derzho and M. G. Velarde, *Multiscaled solitary waves*, private communication, 1995.

[18] P. G. Drazin, *Solitons*, Lond. Math. Soc. Lecture Note Ser., vol. 85, Cambridge University Press, 1983, p. 33.

[19] M. L. Dubreil-Jacotin, *Sur la determination rigoureuse des ondes permanentes periodiques d'amplitude finie*, J. Math. Pure Appl. **13** (1937), 217.

[20] J. E. Fjeldstad, *Interne Wellen*, Geofys. Publika. **X** (1933), no. 6, 3–35.

[21] B. Fornberg, *A practical guide to pseudospectral methods*, Cambridge University Press, 1996.

[22] D. G. Fox and S. A. Orszag, *Pseudospectral approximation to two-dimensional turbulence*, J. Comp. Phys. **11** (1973), 612.

[23] C. S. Gardner, J. M. Greene, M. D. Kruskal, and R. M. Miura, *Korteweg-de Vries equation and generalizations. VI. Methods of Exact Solution*, Comm. Pure Appl. Math. **27** (1974), 97–133.

[24] J. A. Gear and R. Grimshaw, *A second-order theory for solitary waves in shallow fluids*, Phys. Fluids **26(1)** (1983), 14–29.

[25] D. Gottlieb, M. Hussaini, and S. Orszag, *Introduction: Theory and applications of spectral methods*, Spectral Methods for Partial Differential Equations (R. Voigt, D. Gottlieb, and M. Hussaini, eds.), SIAM, 1984, pp. 1–54.

[26] D. Gottlieb and S. A. Orszag, *Numerical analysis of spectral methods*, 1989.

[27] R. Grimshaw, *On steady recirculating flows*, J. Fluid Mechanics **39** (1969), 695–703.

[28] _____, *Solitary waves in compressible fluid*, J. Pure Appl. Geophysics **119** (1980/81), 780–797.

[29] _____, *Resonant flow of a rotating fluid past an obstacle: the general case*, Stud. Appl. Math. **83** (1990), 249–269.

[30] _____, *Internal solitary waves*, Advances in Coastal and Ocean Engineering (P.L.-F. Liu, ed.), vol. 3, World Scientific Publishing Co., Singapore, 1997, pp. 1–30.

[31] R. Grimshaw and Z. Yi, *Resonant generation of finite-amplitude waves by the uniform flow of a uniformly rotating fluid past an obstacle*, Mathematika **40** (1993), 30–50.

[32] R. Grimshaw and Zengxin Yi, *Resonant generation of finite-amplitude waves by the flow of a uniformly stratified fluid over topography*, J. Fluid Mechanics **229** (1991), 603–628.

[33] A. K. Gupta, *Swirl flows*, 1st ed., Abacus Press, 1984.

[34] J. He, *Numerical spectral methods for nonlinear wave equations*, Ph.D. thesis, Monash University, 1997.

[35] C. Hirsch, *Numerical computation of internal and external flows*, vol. I, Wiley-Interscience, 1988.

[36] M. Y. Hussaini and T. A. Zang, *Iterative spectral methods and spectral solutions to compressible flows*, Spectral Methods for Partial Differential Equations (R. G. Voigt, D. Gottlieb, and M. Y. Hussaini, eds.), SIAM, 1984, pp. 119–140.

[37] D. A. H. Jacobs, *The strongly implicit procedure for the numerical solution of parabolic and elliptic partial differential equations*, Tech. report, Central Electricity Research Laboratory, 1972, Note RD/L/N66/72.

[38] R. S. Johnson, *A modern introduction to the mathematical theory of water waves*, Cambridge Texts in App. Math., Cambridge University Press, 1997, p. 249.

[39] T. F. Chan K.-K. Tung and T. Kubota, *Large amplitude internal waves of permanent form*, Stud. in Appl. Math. **66** (1982), 1–44.

[40] L. Kantorovich, *The method of successive approximations for functional equations*, Acta Math. **71** (1939), 63–97.

[41] D. J. Korteweg and G. de Vries, *On the change of form of long waves advancing in a rectangular canal, and on a new type of long stationary waves*, Phil. Mag. **39** (1895), no. 5, 422-443.

[42] W. Krauss, *Interne Wellen großer Amplitude, Teil 1*, Deutsche Hydro. Zeit. **10** (1957), no. 5, 191-201.

[43] _____, *Interne Wellen großer Amplitude, Teil 2*, Deutsche Hydro. Zeit. **11** (1958), no. 5, 194-255.

[44] _____, *Interne Wellen*, Bornträger, Berlin, 1973, p.134.

[45] A. I. Leonov and Yu. Z. Miropol'skiy, *Toward a theory of stationary nonlinear internal gravity waves*, Atmospheric and Oceanic Physics **11** (1975), 298-304.

[46] M. J. Lighthill, *Waves in fluids*, Comm. Pure Appl. Math. **XX** (1967), 267-293.

[47] R. R. Long, *Some aspects of the flow of stratified fluids, I. A theoretical investigation*, Tellus **5** (1953), 42.

[48] _____, *Some aspects of the flow of stratified fluids, II. Experiments with a two-fluid system*, Tellus **6** (1954), no. 2, 97-115.

[49] _____, *Some aspects of the flow of stratified fluids, III. Continuous density gradients*, Tellus **7** (1955), no. 3, 341-357.

[50] _____, *The initial-value problem for long waves of finite amplitude*, J. Fluid Mechanics **20** (1964), 161-170.

[51] R. R. Long and J. B. Morton, *Solitary waves in compressible, stratified fluids*, Tellus **XVIII,1** (1966), 79-85.

[52] L. Magaard, *Zur Theorie zweidimensionaler nichtlinearer interner Wellen in stetig geschichteten Medien*, Kieler Meeresforschung **21** (1965), Inst. Meereskunde Universität Kiel.

[53] G. J. McCarthy, *Investigation into the multigrid code MGD1*, Report AERE-R 10889 (1983), Harwell.

[54] M. E. McIntyre, *On Long's hypothesis of no upstream influence in uniformly stratified or rotating flow*, J. Fluid Mechanics **52** (1972), 209-243.

[55] V. E. Nakoryakov, B. S. Pokusaev, and I. R. Schreiber, *Wave propagation in gas-liquid media*, 2nd ed., CRC Press, Boca Raton, 1993.

[56] K. Oswatitsch, *Gas dynamics*, 1st ed., Academic Press, 1956.

[57] D. E. Pelinovsky and R. H. J. Grimshaw, *Instability analysis of internal solitary waves in a nearly uniformly stratified fluid*, Phys. Fluids 9 (1997), no. 11, 3343–3352.

[58] J. W. Rottman, D. Broutman, and R. Grimshaw, *Numerical simulations of uniformly stratified fluid flow over topography*, J. Fluid Mechanics 306 (1996), 1–30.

[59] J. S. Russell, *Report on waves*, Rep. 14th Meet. Brit. Assoc. Adv. Sci. (1844), 311–390.

[60] A. P. Stamp and M. Jacka, *Deep-water internal solitary waves*, J. Fluid Mechanics 305 (1995), 347–371.

[61] H. J. Stetter, *Analysis of discretization methods for ordinary differential equations*, Springer Verlag, 1973.

[62] H. L. Stone, *Iterative solution of implicit approximations of multi-dimensional partial differential equations*, SIAM J. Numer. Anal. 5 (1968), 530–558.

[63] V. L. Streeter and E. B. Wylie, *Fluid mechanics*, 6th ed., McGraw Hill, 1975.

[64] C. L. Streett and T. A. Zang, *Spectral multi·   ·id methods with applications to transonic potential flow*, J. Comp. Phys. 57 (1985), 43–76.

[65] D. E. Terez and O. M. Knio, *Numerical simulations of large-amplitude internal solitary waves*, J. Fluid Mechanics 362 (1998), 53–82.

[66] K.-K. Tung, T. F. Chan, and T. Kubota, *Large amplitude internal waves of permanent form*, SIAM 66 (1982), 1–44.

[67] J. K. Vennard, *Elementary fluid mechanics*, 4th ed., J. Wiley & Sons, 1961.

[68] M. I. Weinstein, *Lyapunov stability of ground states of nonlinear dispersive evolution equations*, Comm. Pure and Appl. Math. 39 (1986), 51–68.

[69] J. Weissinger, *Zur Theorie und Anwendung des Iterationsverfahrens*, Math. Nachr. 8 (1952), 193–212.

[70] P. Wesseling, *A robust and efficient multigrid method*, Multigrid Methods. Springer Lecture Notes in Mathematics **960** (1982), 614–630.

[71] ———, *Theoretical aspects of a multigrid method*, SIAM J. Sci. Statist. Comput. **3** (1982), 387–407.

[72] J. H. Williamson, *Low-storaye Runge-Kutta schemes*, J. Computat. Phys. **35** (1980), 48–56.

[73] N. J. Zabusky and M. D. Kruskal, *Interactions of solitons in a collisionless plasma and the recurrence of initial states*, Phys. Rev. Lett. **15** (1965), 240–243.

[74] T. A. Zang, *Spectral methods for simulations of transition and turbulence*, Comp. Meth. Appl. Mech. Eng. **80** (1990), 209–221.

# List of amendments

1. On page (vi) in the second reference replace "to appear" with:
   "28:323-247"

2. On page 2 in the second paragraph insert at the end of the first sentence:
   "..., see Apel (1980,1995) and Ostrovsky and Stepanyants (1989)."
   On page 2 in the second paragraph insert at the end of the second sentence:
   "... (see, the reviews by Smith (1988) and Christie (1989))."
   On page 2 in the second paragraph insert at the end of the third sentence:
   "..., see overview by Grimshaw (1997)."
   On page 2 in the second paragraph insert at the end of the last sentence:
   "..., see Gupta (1984)."

   Add to the list of references in the Bibliography:

   J. R. Apel (1980) "Satellite sensing of ocean surface dynamics", Ann. Rev. Earth Planet. Sci. 8:303-342

   J. R. Apel (1995) "Linear and nonlinear internal waves in coastal and marginal seas", Oceanographic Applications of Remote Sensing, eds. M. Ikeda and F. Dobson, CRC Press, Boca Raton, Florida

   L. A. Ostrovsky and Yu A Stepanyants (1989) "Do internal solitons exist in the ocean?", Rev. Geophysics 27: 293-310

   R. K. Smith (1988) "Travelling waves and bores in the lower atmosphere: the 'morning glory' and related phenomenum", Earth Sci. Rev. 25: 267-290

   D. R. Christie (1989) "Long nonlinear waves in the lower atmosphere", J. Atm. Sci. 46: 1462-1491

   R. Grimshaw (1997) "Internal solitary waves", Adv. Coastal and Ocean Eng., ed. P.L-F. Liu, World Scientific Publ. Co., Singapore, Vol. 3, 1-30.

3. On page 6 in Table 1.1 replace:
   "deviation from uniform (linear) stratification $N^2$ ... and topography"
   by
   "deviation from uniform (linear) stratification and topography.

4. Replace last sentence of first paragraph on page 11 with
   "The governing equations for the stratified flow through a channel are followed by the governing equations for the rotating flow of a constant density fluid through a cylindrical channel."

5. On page 11 after equation (2.4) insert:
   "Equation (2.1) and (2.2) are the momentum equations for the horizontal and vertical velocities $u$ and $w$. Equation (2.3) represents the conservation of total density $\rho$ and equation (2.4) is the incompressibility condition. The pressure is denoted by $p$.

6. On page 12 in the third line from the bottom replace
   "To identify the Boussinesq approximation ... in the Boussinesq approximation by $\kappa = 0$."
   by

"To identify the Boussinesq approximation, it is appropriate to introduce an artificial parameter $\kappa$, which is set to $\kappa = 0$ for the equations in the Boussinesq approximation and set to $\kappa = 1$ for the equations in the non-Boussinesq case."

7. On page 17 in the fourth line from the bottom add to the end of the sentence: "... having a value typical for water, and $\sigma = 0.01$ typical for an oceanographic setting."

8. Put Figures 5.1, 5.2 and 5.12 on page 23 (chapter 3) rather than in chapter 5.

9. Insert the following at the bottom of page 24 after Rottman [58]:
"The complete derivation of the finite-amplitude long-wave equation can be found in [32] and is not repeated here. It will only be stated here for reasons of completeness."

10. On page 25 replace the paragraph starting from line 4 after section 3.3 "The amplitude equation ..." and ending at the bottom of the page "... polynomial terms of degree $q < 5$." with the following:

The amplitude equation for such multi-scale internal solitary waves that arises from an asymptotic expansion of the governing equations has nonlinearities that are of greater power than in the common Korteweg-de Vries equation. Due to the similarities of this amplitude equation to the generalized KdV equation its stability properties are comparable to the characteristics of the generalized KdV equation. The generalized KdV equation can be written as

$$\cdot \text{ equation } (3.50)$$

where $p <= 4$. Note that the generalized KdV includes the KdV and mKdV equation and a term of higher order nonlinearity. Benjamin (1972) [2] has proven the stability of KdV type waves which was extended by Bona (1976) [6]. The KdV wave is given by $p = 1$ and the mKdV wave by $p = 2$. Weinstein (1986) [68] has shown the stability and integrability for $p < 4$. For $p >= 4$ no stability proof is available. Bona et al (1987) [7] assume that an amplitude equation of the gKdV type (3.50) is marginally stable for $p = 4$ and unstable for $p > 4$. The multi-scale internal solitary waves derived by Derzho and Velarde (1995) [17] contain a polynomial term R(A) on the right hand side of equation (3.50) of quintic power $q = 5$ and additional polynomial terms of degree $q < 5$.

11. On page 28 replace the sentence after equation (3.66) starting with "Equation (2.19)" with:
"The steady form of equation (2.21) shows that the circulation C is constant along streamlines, thus $C = C(\psi)$ where the functional form of $C = C(\psi)$ is to be determined from the upstream inflow condition for those streamlines which originate upstream."

12. On page 31 insert after the second sentence of section "Derivation of the steady-solutions":
"... and let $X = \epsilon x$ as well as $\hat{\kappa} = \kappa/\epsilon^2$, $\hat{\sigma} = \sigma/\epsilon^2$."

13. On page 36 line 7 from bottom replace differential with derivative.
On page 37 line 6 from top replace differential with derivative.

14. On page 37 after the first paragraph add:
"In this study a time step of $dt = 0.46$ was used for the non-Boussinesq case and a time step of $dt = 0.001$ for the rotating flow. The time step was usually limited by what the numerical scheme required to account for the changes in the solution. Due to the small step size for the rotating flow the maximum time that could be achieved computationally was much smaller."

15. On page 37 after the end of the first paragraph insert the following:
"The low-storage Runge-Kutta scheme is given explicitly by

```
y = yₙ
for  k = 3, 1, −1
        y = yₙ + Δt/k F(y)
end for
yₙ₊₁ = y.
```

16. On page 37 second paragraph in the last sentence replace
"Finite difference methods approximate spatial ... trading off accuracy."
with
"Finite difference methods in effect approximate spatial derivatives by a Taylor series of finite order. They are frequently applied to complicated problems, due to their straightforward implementation."

17. On page 38 and line 3 from the top replace albeit with despite.

18. On page 38 after the second paragraph insert:
"The equations can be transformed to topography-following coordinates by making the transformation $(X, Z)$

$$X = x, Z = D\left[\frac{z - h(x)}{D - h(x)}\right].$$

The top and bottom horizontal boundaries are then parallel regardless of the bottom topography $h(x)$.

19. On page 38 in the second paragraph from bottom add to the sentence "In the vertical Chebyshev ... the vertical." the following
"Typically 256 Fourier modes in the horizontal and 65 Chebyshev modes in the vertical are sufficient to resolve the waves studied here."

20. Replace the second last sentence on page 38 "A 2/3 filter on the highest modes is used ... domain." by
"A 2/3 filter on the highest modes is used to remove aliasing errors, see Boyd [8] and Canuto [12]. It consists of keeping only those coefficients of the Fourier transform for which the wavenumber $|k| \leq \frac{N}{2}$ and set all other coefficients to zero. Without a filter the numerical growth of high wavenumbers is aliased into low wavenumbers, which can lead to an unphysical cascade of energy from high to low wavenumbers and eventual numerical instability.

A sponge is situated across the boundary condition in the horizontal to prevent energy propagated downstream from re-entering the domain. The sponge layer covers about $\frac{1}{16}$th on each end of the computational domain and continuously smoothes any perturbation to the basic streamfunction and density field using a tanh profile."

21. On page 42 insert the following after the paragraph ending on line 5 from the top:

"The equations of motion for the time-dependent non-Boussinesq stratified flow solved numerically are given by equations (2.11) and (2.12) and explicitly

$$\omega_t = -U\omega_x - J(\psi, \omega) - \frac{\rho_x}{\rho}\left(g + \frac{D\psi_x}{Dt}\right) - \frac{\rho_z}{\rho}\frac{D\psi_z}{Dt}$$

for the vorticity $\omega$ and

$$\rho'_t = -U\rho'_x - J(\psi, \rho') - \psi_x\bar{\rho}_z$$

for the density perturbation $\rho'$."

22. On page 42 and line 12 from the bottom replace reference to equation (4.9) with (4.8)
On page 42 and line 9 from the bottom replace reference to equation (4.9) with (4.8)
On page 44 and line 4 from the top replace reference to equation (4.9) with (4.8)

23. On page 46 and line 15 from the bottom add to sentence ending "... with all the eigenvalues in Chebyshev space." the following:

"... with all the eigenvalues in Chebyshev space, see Canuto et. al. [12]"

24. On page 47 after the paragraph ending line 3 from the top insert:

"The equations of motion for the rotating flow through a cylindrical channel solved numerically are explicitly are given by equations (2.20) and (2.21)."

25. On page 48 in the subsection on 'A solution to the linearized equations' replace the last sentence
"The numerical model... within the error of the computation."
with

"The non-Boussinesq model has been initialized with the solution given by equation (4.24). The error in the growth rate, equation (4.25), is of order $O(10^{-2})$ on a time scale of $O(10^{-1}s)$. Due to the no-flow boundary condition enforced at the top and bottom boundary and the multiplication by a Gaussian function, see equation (4.24), the theoretical growth rate (4.25) is only representative initially."

26. On page 49 in the subsection on 'Conservation laws' insert at the end of the paragraph:
"The error in the conservation laws is of order $O(10^{-9})$ for a KdV solitary wave and the solitary wave remains stationary in the reference frame for times of order $O(10^3 s)$.

27. On page 49 in the subsection on 'Kinetic and potential energy' replace the last sentence.
"Gaussian quadrature is used ... error of the numerical model"
with

"Gaussian quadrature is used to compute the two-dimensional integrals. The change in energy is computed for the non-Boussinesq model for large times using a large-amplitude solitary wave with a vortex core as an initial condition. The relative change in energy $\frac{E - E_{initial}}{E_{initial}}$ is of order $O(10^{-9})$ for times of order $O(10^4 s)$ , which confirms that the numerical scheme conserves energy and is non-dissipative.

28. On page 50 replace the first 3 sentences of the first paragraph by:
"This section presents the results for the four applications considered. Firstly the results for the large-amplitude internal solitary waves with vortex cores in the Boussinesq approximation followed by the non-Boussinesq case are presented. These results are followed by the results for the stratified flow over topography and multi-scaled internal solitary waves."

29. On page 50 insert at the beginning of section 5.1:
"This section presents the results for the time-dependent simulation of large-amplitude internal solitary waves with vortex cores in a stratified fluid. The results for the equations in the Boussinesq approximation will be discussed first and followed by the discussion of the results for the non-Boussinesq case of the governing equations. The numerical results aim to show that the solitary waves derived by DG are permanent of shape and that the recirculation region remains stagnant to first order, as predicted by the theoretical results."

30. On page 51 in the second paragraph add the following after the sentence ending with "... as predicted by DG.":
"Note that the contours of the streamfunction inside the vortex core are an artefact of the visualization routine and do not represent an inhomogeneity of the core."

31. On page 51 in the last paragraph replace:
"The amplitude of the steady state solution is measured for a number of different phase speeds from ..."
with
"Throughout the whole study a range of steady state solutions are investigated using 5 to 7 amplitudes

within the minimum amplitude $A_*$ and maximum possible amplitude $A_* + \mu_{max}$ for which solitary waves with vortex cores exist. The parameter $\mu$ was chosen to be greater than 65% and less than 95% of the maximum possible value $\mu_{max}$ $(0.65\mu_{max} < \mu < 0.95\mu_{max})$.

32. On page 51 replace the sentence on the fifth line from the bottom
    "The results agree computation."
    with
    "The numerical results displayed in Figures 5.1 and 5.2 represent the relative phase speed $\frac{c-c_0}{c_0}$ versus amplitude. The results exhibit a deviation of the numerical results from the theoretical of order much less than $10^{-3}$ $(\Delta c = O(10^{-4}))$. The deviation of the numerical results from the theoretical values is much smaller than the error terms of the theoretical solution, which are of order $\epsilon^2 = 0.01$. In the numerical simulations a range of values in the interval $A_{min}$ to $A_{max}$ were chosen but the numerical results do not exactly follow the theoretical curve. This is attributed to the limit of the accuracy of the numerical scheme as well as the theoretical solution. The fact that the phase speed-amplitude results of Figure 5.1 and 5.2 are close to the theoretical values and the time-evolution of the solutions in Figures 5.4 and 5.8 confirm the validity and stability of the theoretical solution."

33. On page 52 and in the first line replace the part "..., which corresponds ... hours." with
    "..., which corresponds to the flow having traversed the width of the waves for approximately 11 times and a dimensional time of more than $8.3\bar{3}$ hours."

34. On page 52 in the first line replace "It is argued..." with
    "The author of this thesis argues ..."

35. On page 52 on second last paragraph and third sentence replace $O(10^{-4})$ with $O(10^{-2})$, $O(\sigma^2)$ with $O(\epsilon^2)$ and $\sigma = 0.01$ with $\epsilon^2 = 0.01$.

36. On page 66 at the beginning of section 5.2 replace the first sentence with:
    "This section presents the results for the two-dimensional time-dependent stratified flow over topography using the non-Boussinesq numerical model. The purpose of this investigation is to compare the results of the non-Boussinesq model with the results of the numerical model based on the finite-amplitude long-wave [FALW] equation derived by Grimshaw and Yi [32]. The numerical model used for the FALW equation is not identical to the model used by Grimshaw and Yi. It it is based on the improved scheme implemented by Rottman et.al. and applied to the FALW equation including the non-Boussinesq term neglected in the Boussinesq approximation."

37. On page 66 after equation 5.2 insert
    "... such that the buoyancy frequency $N$ is constant, ..."

38. On page 77 insert at the beginning of section 5.3:
    "This section presents the results for the simulation of multi-scaled solitary waves in a stratified fluid using the non-Boussinesq numerical model. The purpose of this investigation is to show that the multi-scaled internal solitary waves derived by Derzho and Velarde [17] are permanent of shape.

39. In the fifth line from the top on page 77 replace the sentence "The final time is about six hours ... shape." with
    "The final time corresponds to approximately seven hundred buoyancy periods $\left(T = \frac{2\pi}{N}\right)$ and 6 hours in dimensional time, which is long enough to consider the wave to be of permanent shape."

40. Replace the last sentence in the first paragraph on page 77:
"The solutions show little change of shape ... within the accuracy of the numerical model."
with
"The two cases considered here are for two respective cases: when the wavelength of the solution is quite large ($\alpha_3 = 1.001$) and comparably small ($\alpha_3 = 1.1$). In both cases the numerical results show only little change of shape, wavelength and amplitude of the solutions derived by Derzho and Velarde."
and add at the end of the second paragraph
"The numerical results obtained here show that the multi-scale internal solitary wave solutions obtained by Derzho and Velarde are stable solutions and retain a balance between nonlinearity and dispersion necessary for solitary wave propagation. Furthermore the stability of these solutions agrees with the stability analysis by Weinstein [68] and Bona et al [7] for amplitude equations of the generalized KdV type."

41. On page 81 in Table 5.4 replace $\kappa$ and $\sigma$ with $\hat{\kappa}$ and $\hat{\sigma}$.

42. On page 81 at the beginning of section (5.4) replace the first sentence with:
"This section presents the results for the time-dependent simulation of large-amplitude inertial solitary waves with vortex cores in a rotating flow through a cylindrical channel. The purpose of this study is to verify the existence and permanence of the large-amplitude solitary waves with vortex cores derived by Derzho and Grimshaw [15] and in particular that the recirculation region remains stagnant to first order."

43. On page 81 insert the following after the sentence on line 6 from the bottom:
"The solutions are computed up to a maximum time $t_n \approx 8$ corresponding to approximately 20 revolutions of the fluid on the rotation timescale, $T = \frac{1}{\Omega_0}$. This length of time is sufficient to verify whether or not the theoretical solution by DG is permanent of shape."

44. On page 81 after the second paragraph from the bottom replace sentence
"The recirculation regions remain stagnant to first order."
with
"For the first case of a strong rotational shear and a KdV outer solution, see Figure 5.36, an upstream steepening of the wave is noticeable. Transients moving downstream are observable in the contour plot of the circulation, see Figure 5.37. The close up contour plot of the recirculation region shows a change in the strength of the recirculation region of order $O(10^{-4})$, but the recirculation region is only known to first order of the asymptotic expansion, equation (3.84), where the corrections to the recirculation region are of order $\epsilon^2 = 0.01$. Thus the recirculation region remains stagnant to first order. For the second case of uniform rotation and for the third case of a jet-like inflow condition the change in the strength of the recirculation region are of order $O(10^{-6})$."

45. After the first sentence on page 82 insert:
"For the first case of a strong rotational shear the change in amplitude is of the order $O(10^{-2})$ indicating that the steady state solution has not been reached. For the second and third case the change in amplitude is of order $O(10^{-4})$ and is approaching a constant. In all three cases considered the adverse velocity is linearly decreasing with time on the order of $O(10^{-6})$ ($O(10^{-3})$ in one run of the first case), but as mentioned above this is to within the accuracy of the known theoretical solution.

46. On page 82 remove the first sentence of the last paragraph: "All results show a nearly linear ... less than 1%."

47. On pages 83, 89, 95 in the captions of Figures 5.34, 5.43 and 5.52 replace $\kappa$ and $\sigma$ with $\hat{\kappa}$ and $\hat{\sigma}$.

48. On pages 89, 95, 101 in the captions of figures 5.42, 5.51 and 5.60 replace Amplitude with amplitude.